



LPJ-GUESS/LSMv1.0: A next generation Land Surface Model with high ecological realism

David Martín Belda¹, Peter Anthoni¹, David Wårlind², Stefan Olin², Guy Schurgers^{3,5}, Jing Tang^{2,3,4}, Benjamin Smith^{2,6}, and Almut Arneth¹

¹Karlsruhe Institute of Technology KIT, Institute of Meteorology and Climate Research - Atmospheric Environmental Research (IMK-IFU), 82467 Garmisch-Partenkirchen, Germany

²University of Lund, Department of Physical Geography and Ecosystem Science, 223 62, Lund, Sweden

³Terrestrial Ecology Section, Department of Biology, Universitetsparken 15, DK-2100, Copenhagen Ø, Denmark

⁴Center for Permafrost (CENPERM), University of Copenhagen, Øster Voldgade 10, DK-1350, Copenhagen K, Denmark

⁵Department of Geosciences and Natural Resource Management, University of Copenhagen, Copenhagen, Denmark

⁶Hawkesbury Institute for the Environment, Western Sydney University, Richmond, NSW, Australia.

Correspondence: David Martín Belda (david.belda@kit.edu)

Abstract. Land biosphere processes are of central importance to the climate system. Specifically, biological processes interact with the atmosphere through a variety of feedback loops that modulate energy, water and CO₂ fluxes between the land surface and the atmosphere across a wide range of temporal and spatial scales. Human land use and land cover modification add a further level of complexity to land-atmosphere interactions. Dynamic Global Vegetation Models (DGVMs) attempt to capture these land surface processes, and are increasingly incorporated into Earth System Models (ESMs), which makes it possible to study the coupled dynamics of the land-biosphere and the climate. In this work we describe a number of modifications to the LPJ-GUESS DGVM, aimed at enabling direct integration into an ESM. These include energy balance closure, the introduction of a sub-daily time step, a new radiative transfer scheme, and improved soil physics. The implemented modifications allow the model (LPJ-GUESS/LSM) to simulate the diurnal exchange of energy, water and CO₂ between the land-ecosystem and the atmosphere. A site-based evaluation against FLUXNET2015 data shows reasonable agreement between observed and modeled sensible and latent heat fluxes. Differences in predicted ecosystem function between standard LPJ-GUESS and LPJ-GUESS/LSM vary across land cover types, but the emergent ecosystem composition and structure are consistent between the two versions. We find that the choice of stomatal conductance model has a major impact on the model's predictions. The new LSM implementation described in this work lays the foundation for using the well established LPJ-GUESS DGVM as an alternative LSM in coupled land-biosphere-climate studies, where an accurate representation of ecosystem processes is essential.

1 Introduction

The land surface is of central importance in the climate system, as feedbacks between the land-biosphere and the atmosphere impact climate across a wide range of temporal and spatial scales (Pitman, 2003). Biological processes affected by climate variations can feed back into the climate by modulating the fluxes of energy and water between vegetation and the atmosphere



(Guo et al., 2006; Green et al., 2017). For example, the early, strong greening caused by the warming climate can enhance evapotranspiration, which may result in a seasonal cooling effect or in an amplification of heat waves, depending on regional characteristics and water availability (Peñuelas et al., 2009; Lorenz et al., 2013). On decadal time scales, decreased vegetation cover caused by reduced rainfall can further decrease local precipitation (Zeng et al., 1999). Large scale shifts in vegetation cover in response to climate change can affect global and regional climate by altering the radiation and water budgets (O'ishi and Abe-Ouchi, 2009; Levis et al., 2000; Wramneby et al., 2010; Wu et al., 2021).

The climate and the biosphere are also coupled biogeochemically through the carbon cycle (Luo, 2007). Increased atmospheric carbon dioxide (CO₂) concentration promotes vegetation growth through CO₂ fertilization, which increases plant CO₂ absorption from the atmosphere. However, higher temperatures caused by a higher atmospheric CO₂ concentration enhance the release of CO₂ from respiration (Cramer et al., 2001; Piao et al., 2013). Other important effects relate to extreme events (Zscheischler et al., 2014), disturbances (Kurz et al., 2008; Metsaranta et al., 2010) or interaction with the nitrogen cycle (Arnoeth et al., 2010; Lamarque et al., 2013; Ciais et al., 2014).

Of particular importance is the added complexity arising from land use and land-cover change. Conversion of forests into cropland or grassland increases surface albedo, which may promote surface cooling in temperate latitudes (e.g. Noblet-Ducoudré et al., 2012), but is also a significant contributor to anthropogenic CO₂ emissions (Arnoeth et al., 2017; Le Quéré et al., 2018). Observations and model studies suggest that historical land cover changes over the industrial era have had a minor net impact on the climate system at the global scale, but regional effects are large (Brovkin et al., 2004; Pongratz et al., 2010; Christidis et al., 2013). Further complexity arises from the interaction between land use change and the water cycle (e.g. Narisma and Pitman, 2003; Kumar et al., 2013; Lawrence and Vandecar, 2015), atmospheric circulation (Swann et al., 2012; Wu et al., 2017) and from atmospheric teleconnections (Werth and Avissar, 2002; Medvigy et al., 2013).

Incorporating DGVMs into ESMs allows the interactions between the biosphere and the rest of the climate system to be studied on the long time scales of vegetation dynamics and biogeochemical and biogeographical responses (Quillet et al., 2010; Fisher et al., 2018). There is considerable uncertainty regarding the carbon cycle response to future climate warming scenarios (Friedlingstein et al., 2006, 2014; Jones et al., 2013), much of which has been attributed to uncertainty in the representation of land surface processes (Huntingford et al., 2009; Booth et al., 2012; Friend et al., 2014) and differences between the global circulation models (GCMs) used to make such projections (Ahlström et al., 2013, 2017; Schurgers et al., 2018). Improved representations of land-biosphere processes and land use change in ESMs are therefore essential to constrain climate change projections (Friend et al., 2014) and thus to support the assessment of mitigation and adaptation strategies.

DGVMs are frequently coupled to ESMs through an intermediary Land Surface Model (LSM), which facilitates the sub-daily energy, water and gas exchange calculations (e.g. Bonan et al., 2003; Krinner et al., 2005; Smith et al., 2011; Döscher et al., 2021). This approach can, however, entail inconsistencies between the DGVM and the LSM, such as the use of different time steps and temperatures in photosynthetic calculations, duplicated or inconsistent soil water tracking, or different characterization of vegetation types. In this work we modify the LPJ-GUESS DGVM (Smith et al., 2001, 2014) to enable coupling with an atmospheric model without the need for a mediating LSM. LPJ-GUESS simulates a wide range of land-biosphere processes, including vegetation growth, establishment and mortality, plant functional type (PFT) competition, disturbances, wildfires, and



land use change. This model has been used in a broad range of applications, including coupled biosphere-atmosphere regional (Wramneby et al., 2010; Smith et al., 2011; Zhang et al., 2014, 2018; Wu et al., 2016, 2021) and global (Weiss et al., 2014; Alessandri et al., 2017; Forrest et al., 2020; Döscher et al., 2021) studies, and undergoes active development and evaluation, which makes it a suitable choice to study climate-biosphere interactions.

60 Coupling LPJ-GUESS with an atmospheric model requires it to be able to calculate diurnal energy and water exchange rates between plant canopies and the atmosphere. To achieve this, we introduced several major modifications to LPJ-GUESS v4.0, namely: (a) a new radiative transfer scheme, capable of representing direct and diffuse light, as well as treating sunlit and shaded leaves separately; (b) representation of the energy balance on a sub-daily time step; and (c) an improved representation of heat and water transport in the soil. Section 2 describes these modifications in detail. A site-based evaluation of the modeled
65 fluxes against eddy covariance data is presented in Section 3. Finally, the work is discussed and summarized in Section 4.

2 Model description

2.1 LPJ-GUESS

LPJ-GUESS (Smith et al., 2001, 2014) is a process-based model of vegetation dynamics and ecosystem biogeochemistry and water cycling that incorporates tree demographic processes and competition for light, space and soil resources among co-
70 occurring PFTs. Capturing establishment, growth and death of individuals allows to better represent the mechanisms underlying competition, population and community structural dynamics, carbon assimilation and ecosystem carbon turnover (Smith et al., 2001; Wolf et al., 2011a). In LPJ-GUESS, natural vegetation is represented as a co-occurring mixture of different PFTs, divided into age classes or *cohorts*, in a modeled area or *patch*. New cohorts can establish in the patch when climatic conditions are within PFT-prescribed bioclimatic limits, and compete with other cohorts for light, water and soil nitrogen. Each cohort
75 assimilates atmospheric CO₂ at a rate, updated daily in the standard model, that depends on the amount of photosynthetically active radiation (PAR) it absorbs, water availability, temperature, and the maximum rate of carboxylation, V_{\max} . The maximum rate of carboxylation is estimated under the assumption that plants redistribute leaf nitrogen content across the canopy so as to maximize net assimilation at the canopy level (Haxeltine and Prentice, 1996), and is limited by nitrogen availability (Smith et al., 2014). The yearly assimilated carbon is distributed between roots, leaves and, in the case of woody PFTs, sapwood,
80 according to a set of PFT-specific allometric constraints. The phenological status of the cohorts (for summergreen and raingreen PFTs) is updated daily. Population dynamics (establishment and mortality) and non-fire related disturbances are modeled as stochastic processes, influenced by environmental factors, vegetation structure, growth and competition. Disturbances occur recurrently and destroy all vegetation in a patch, restarting the successional cycle. Wildfires are modeled explicitly (Thonicke et al., 2001). At any given geographical location (*gridcell*), a number of replicate patches with independent successional
85 histories are simulated.

LPJ-GUESS can represent managed land (croplands, pastures/rangelands and managed forest) and land use change (Lindeskog et al., 2013, 2021; Olin et al., 2015). Each gridcell contains different land cover types or *stands*, which are updated every simulation year (for example, to simulate conversion of forest to cropland). Croplands are represented as single PFT



stands, distinguishing various rainfed and irrigated crop functional types. In pasture stands only grassy PFTs are allowed to establish. Simulated land management practices include crop sowing, irrigation, fertilization, harvest, rotation and abandonment, and pasture grazing.

2.2 Model modifications

Figure 1 shows a comparison of the daily loop in standard LPJ-GUESS and in the new LSM implementation. In both versions, phenology and soil organic matter dynamics are calculated daily, and carbon allocation (growth) and vegetation dynamics (establishment, mortality and disturbance) are computed at the end of every simulation year.

Radiative transfer in standard LPJ-GUESS is based on Beer's law (Monsi and Saeki, 1953, 2005). The canopy is divided in vertical layers, each absorbing a fraction of the PAR let through by the layer above. The PAR absorbed by each layer is then split among cohorts according to their share of leaf area index (LAI) in that layer. In this way, taller cohorts have access to more PAR and shade the lower layers of the canopy. Daily unstressed values of V_{\max} and canopy conductance g_{pot} are first computed for each cohort assuming well watered conditions. The actual evapotranspiration rate in the patch is then calculated as the minimum of a potential rate, determined by atmospheric conditions and g_{pot} , and a supply rate, which depends on the amount of soil water available for uptake and the vegetation rooting profiles. For each cohort, the model calculates a daily assimilation rate that is consistent with its contribution to the total patch evapotranspiration. The soil column consists of a top layer of 0.5 m and a bottom layer of 1 m thickness. The fraction of root matter in each soil layer is PFT-specific. Soil water content is updated taking into account daily precipitation, interception, percolation between the two layers, evapotranspiration and runoff. Daily soil temperature is calculated as a dampened, lagged oscillation around the annual mean of the forcing air temperature, as described in Sitch et al. (2003). More detailed descriptions of the radiative transfer, evapotranspiration, assimilation and soil organic matter calculations can be found in the supplement to Smith et al. (2001), Smith et al. (2014), and references therein. The hydrology scheme is described in Gerten et al. (2004).

In the LSM implementation, radiative transfer, energy balance, assimilation and soil heat and water transport are all solved on a subdaily basis. Based on Dai et al. (2004), each cohort is conceptualized as two big leaves, representing its sunlit and shaded parts. Sunlit leaves receive direct solar radiation and diffuse radiation, while shaded leaves receive only diffuse radiation. The total LAI for each cohort is calculated dynamically by LPJ-GUESS. A stem area index (SAI) was added to account for the impact of stems and branches in the energy balance and radiative transfer calculations. Whole canopy leaf area and plant area (PAI) indices are obtained by aggregating over cohorts i :

$$\text{LAI}_c = \sum_i \text{LAI}^{(i)}; \quad (1)$$

$$\text{PAI}_c = \sum_i \left[\text{LAI}^{(i)} + \text{SAI}^{(i)} \right]. \quad (2)$$

Based on Kucharik et al. (1998), we set the stem area index of woody PFTs to 10% of their leaf area index at full leaf coverage. Grasses do not have stem area index. The sunlit and shaded fractions of leaf and plant area indices are updated in the radiative transfer routine on a subdaily basis (Sec. 2.2.2).



We replaced the original two-layer soil column with a new profile consisting of 9 layers. The top 4 layers have thicknesses of 7, 10, 13 and 20 cm, in order of increasing depth, and correspond to the top soil layer in the original soil column. The next three layers have thicknesses of 30, 30 and 40 cm, and correspond to the original bottom layer. These 7 layers constitute the rooting zone. The new water transport scheme assumes, for simplicity, free gravitational drainage at the bottom of the soil column, which can lead to excessive soil dryness during dry periods. Additionally, no heat flux is allowed through the bottom boundary, an approximation better met at higher soil depths. In order to mitigate spurious effects derived from this choice of boundary conditions, we extended the soil column with two additional layers of 50 and 100 cm, reaching a total depth of 3 m.

The sunlit and shaded leaves of each cohort have different assimilation rates and stomatal conductances. The temperatures of sunlit and shaded leaves are different, but common to all the cohorts in the patch. The vertical layering of the canopy is kept in the radiation calculations, but the new scheme distinguishes direct and diffuse radiation and two separate wavebands (visible and near infrared). Infrared radiation does not contribute to photosynthetic assimilation, but needs to be accounted for in the energy balance calculations. A separate treatment of diffuse and direct radiation allows to resolve sunlit and shaded leaves. This approach has been shown to lead to predictions of fluxes of energy, water and CO₂ that are comparable in accuracy to those made by more complex, and considerably more computationally expensive, multi-layered canopy models (Wang and Leuning, 1998).

Each cohort exchanges sensible and latent heat with a common canopy air space, which in turn exchanges sensible and latent heat with the atmosphere (Fig. 2). Assimilation and evapotranspiration are calculated consistently in the energy balance routine. Daily averages of absorbed PAR are used to update V_{\max} for each cohort. The new energy balance, radiative transfer and soil physics calculations are detailed in sections 2.2.1 through 2.2.5.

2.2.1 Energy balance

The energy balance of the patch canopy is described by the following equations (e.g., Bonan, 2008):

$$S_{\text{sun}} = L_{\text{sun}} + H_{\text{sun}} + \lambda E_{\text{sun}}; \quad (3)$$

$$S_{\text{sha}} = L_{\text{sha}} + H_{\text{sha}} + \lambda E_{\text{sha}}, \quad (4)$$

where the S terms are absorbed shortwave radiation, L is net emitted longwave radiation, H is sensible heat flux towards the canopy air space, E is water vapor flux towards the canopy air space, and λ is latent heat of vaporization (here taken constant; $\lambda = 2.44 \cdot 10^6 \text{ J kg}^{-1} \text{ }^\circ\text{C}^{-1}$). The subindices ‘sun’ and ‘sha’ refer to the sunlit and shaded parts of the canopy. The calculation of the shortwave and longwave radiation terms is detailed in Secs. 2.2.2 and 2.2.3.

The sensible heat flux from the sunlit part of the canopy to the canopy airspace is formulated as:

$$H_{\text{sun}} = -2\text{PAI}_{c,\text{sun}}\rho c_P g_b (T_{ca} - T_{\text{sun}}), \quad (5)$$

where $\text{PAI}_{c,\text{sun}}$ is the plant area index of the sunlit canopy, ρ is air density, c_P is the specific heat of air at constant pressure, g_b is average leaf boundary layer conductance (e.g., Bonan, 2008), T_{ca} is the temperature of the canopy air, and T_{sun} is the temperature of the sunlit canopy. The factor 2 expresses heat loss from both sides of the leaf and stem elements.



The latent heat flux from the sunlit part of the canopy to the canopy air is:

$$\lambda E_{\text{sun}} = -\rho \lambda g_{w, \text{sun}} [q_{\text{ca}} - q^*(T_{\text{sun}})], \quad (6)$$

155 where q_{ca} is the specific humidity of the canopy air, $q^*(T_{\text{sun}})$ is the specific humidity inside the stomatal cavity, taken to be the saturated humidity at the leaf temperature, and $g_{w, \text{sun}}$ is the conductance for water vapor flux from the sunlit part of the canopy to the canopy air space. The latter is calculated as a weighted average of the contributions from evaporation of intercepted water and transpiration through the stomata (Appendix A):

$$160 \quad g_{w, \text{sun}} = f_{\text{wet}} \eta_{\text{sun}} \text{PAI}_{c, \text{sun}} g_{\text{b}} + (1 - f_{\text{wet}} \eta_{\text{sun}}) \sum_i \text{LAI}_{\text{sun}}^{(i)} \frac{g_{s, \text{sun}}^{(i)} g_{\text{b}}}{g_{s, \text{sun}}^{(i)} + g_{\text{b}}}. \quad (7)$$

In this equation f_{wet} is the wet fraction of the canopy, the factor η_{sun} limits evaporation to the amount of intercepted water present in the canopy, and $\text{LAI}_{\text{sun}}^{(i)}$ is the leaf area index of the sunlit part of cohort i . The stomatal conductance of cohort i , $g_{s, \text{sun}}^{(i)}$, is related to its net photosynthetic rate through a semiempirical model. We implemented two selectable stomatal conductance models: the Ball-Berry model (Ball et al., 1987) and the Medlyn model (Medlyn et al., 2011).

165 Equations analogous to Eqs. (5) through (7) apply to the shaded part of the canopy.

The energy balance equation for the ground surface is:

$$S_{\text{g}} = L_{\text{g}} + H_{\text{g}} + \lambda E_{\text{g}} + G, \quad (8)$$

where G is heat conducted into the ground. The sensible heat from the ground surface to the canopy air space is:

$$H_{\text{g}} = -\rho c_P g_{\text{ab}} (T_{\text{ca}} - T_{\text{g}}), \quad (9)$$

170 where g_{ab} is the aerodynamic conductance from the ground surface to the canopy air space, which is calculated following Sakaguchi and Zeng (2009). The latent heat from the ground surface to the canopy air is given by:

$$\lambda E_{\text{g}} = -\rho \lambda \frac{g_{\text{surf}} g_{\text{ab}}}{g_{\text{surf}} + g_{\text{ab}}} [q_{\text{ca}} - \alpha q^*(T_{\text{g}})], \quad (10)$$

where we used the model of Sakaguchi and Zeng (2009) for the surface conductance g_{surf} , and $\alpha q^*(T_{\text{g}})$ is the air specific humidity at the ground surface (Philip, 1957).

175 The heat conducted into the ground is calculated as:

$$G = -\kappa_{\text{s}}^{(1)} \frac{T_{\text{s}}^{(1)} - T_{\text{g}}}{\Delta z^{(1)}/2}, \quad (11)$$

where $\kappa_{\text{s}}^{(1)}$, $T_{\text{s}}^{(1)}$, and $\Delta z^{(1)}$ are, respectively, the thermal conductivity, the temperature, and the thickness of the top soil layer.

The following two equations express conservation of latent and sensible heat:

$$H^{\uparrow} = H_{\text{sun}} + H_{\text{sha}} + H_{\text{g}}; \quad (12)$$

$$180 \quad \lambda E^{\uparrow} = \lambda E_{\text{sun}} + \lambda E_{\text{sha}} + \lambda E_{\text{g}}, \quad (13)$$



where H^\uparrow and λE^\uparrow are respectively the sensible and latent heat fluxes into the atmosphere, given by

$$H^\uparrow = -\rho c_P g_{aa}(T_{atm} - T_{ca}); \quad (14)$$

$$\lambda E^\uparrow = -\rho \lambda g_{aa}(q_{atm} - q_{ca}). \quad (15)$$

Here, T_{atm} and q_{atm} are the temperature and specific humidity of the air at the atmospheric reference level, and g_{aa} is the
 185 aerodynamic conductance above the canopy. The latter is calculated by applying Monin-Obukov similarity theory, which
 requires knowledge of the surface roughness length, z_0 , and the zero plane displacement, z_d . These are calculated as a function
 of the canopy plant area index, PAI_c , and the canopy height, h_c , according to the model of Raupach (1994, 1995):

$$\frac{z_d}{h_c} = 1 - \frac{1 - \exp(-\sqrt{7.5PAI_c})}{\sqrt{7.5PAI_c}}; \quad (16)$$

$$\frac{z_0}{h_c} = \left(1 - \frac{z_d}{h_c}\right) \exp\left(-\frac{k}{\beta} + 0.193\right), \quad (17)$$

190 where $k = 0.4$ is the von Karman constant, and $\beta = \min(\sqrt{0.003 + 0.15PAI_c}, 0.3)$. Canopy height is calculated, following
 Forrest et al. (2020), as an average of cohort heights weighted by their foliar projective cover (FPC).

Equations (3), (4) and (8), subject to constraints (12) and (13), are solved simultaneously every time step with a multidimen-
 sional Newton-Rhapson method (e.g. Press, 2003).

2.2.2 Shortwave radiative transfer

195 We adapted the two big leaf model of Dai et al. (2004), based on the two-stream model of Dickinson (1983); Sellers (1985),
 to LPJ-GUESS's multiple cohort, vertically layered canopy. This approach considers direct solar radiation and diffuse at-
 mospheric radiation separately. The intensity of the direct solar radiation beam in the canopy decreases exponentially with
 cumulative plant area index P (measured from the top of the canopy, increasing downwards) (Monsi and Saeki, 1953, 2005):

$$I_D^\downarrow(P) = I_{D0}^\downarrow e^{-kP}, \quad (18)$$

200 where I_{D0}^\downarrow is incoming direct solar radiation and k is the direct beam extinction coefficient. The profile of diffuse radiation
 in the canopy results from the multiple scattering and backscattering of incoming radiation by leaves and stems. Corrected
 profiles (normalized by incoming radiation) of scattered direct beam (\hat{I}_b^\uparrow and \hat{I}_b^\downarrow) and scattered atmospheric diffuse radiation
 (\hat{I}_a^\uparrow and \hat{I}_a^\downarrow) are given in analytic form in Dai et al. (2004) (the arrows indicate the direction of propagation).

The direct beam radiation absorbed in a canopy layer l between P and $P + \Delta_l P$ is calculated as the fraction of the decrease
 205 in direct beam intensity in that layer that is not scattered:

$$S_D^{(l)} = -(1 - \omega) \Delta_l I_D^\downarrow, \quad (19)$$

where ω is the direct beam scattering coefficient, and Δ_l denotes change across layer l . The diffuse radiation absorbed in the
 layer is the sum of the radiation from the direct beam that is scattered and reabsorbed in the layer and the contribution from the



diffuse beams:

$$210 \quad S_d^{(l)} = -\omega \Delta_l I_D^\downarrow + I_{D0}^\downarrow (\Delta_l \hat{I}_b^\uparrow - \Delta_l \hat{I}_b^\downarrow) + I_{d0}^\downarrow (\Delta_l \hat{I}_a^\uparrow - \Delta_l \hat{I}_a^\downarrow), \quad (20)$$

where I_{d0}^\downarrow is incoming atmospheric diffuse radiation. The radiation absorbed by the sunlit and shaded parts of this layer is

$$S_{\text{sun}}^{(l)} = S_D^{(l)} + f_{\text{sun}}^{(l)} S_d^{(l)}; \quad (21)$$

$$S_{\text{sha}}^{(l)} = f_{\text{sha}}^{(l)} S_d^{(l)}, \quad (22)$$

215 where the sunlit and shaded fractions of the layer are given by

$$f_{\text{sun}}^{(l)} = -\frac{e^{-k(P+\Delta_l P)} - e^{-kP}}{k\Delta_l P}; \quad (23)$$

$$f_{\text{sha}}^{(l)} = 1 - f_{\text{sun}}^{(l)}. \quad (24)$$

The total amount of shortwave radiation absorbed by the sunlit and shaded parts of the canopy is obtained by summing over layers:

$$220 \quad S_{\text{sun}} = \sum_l S_{\text{sun}}^{(l)}; \quad (25)$$

$$S_{\text{sha}} = \sum_l S_{\text{sha}}^{(l)}. \quad (26)$$

The shortwave radiation absorbed by the ground surface is calculated as the difference between the downward and upward beams at $P = \text{PAI}_c$,

$$225 \quad S_g = I_D^\downarrow(\text{PAI}_c) + I_{D0}^\downarrow [\hat{I}_b^\downarrow(\text{PAI}_c) - \hat{I}_b^\uparrow(\text{PAI}_c)] + I_{d0}^\downarrow [\hat{I}_a^\downarrow(\text{PAI}_c) - \hat{I}_a^\uparrow(\text{PAI}_c)]. \quad (27)$$

The shortwave radiation reflected back at the atmosphere is obtained by evaluating the upward beams at $P = 0$:

$$I^\uparrow = I_b^\uparrow(0) + I_a^\uparrow(0). \quad (28)$$

The optical elements in the canopy have different properties in the visible and near-infrared wave bands, so the equations above are applied separately to these two parts of the spectrum, and the contributions are summed to calculate total absorption.

230 In this study, we set the optical properties of the canopy to the following values, regardless of PFT:

$$\alpha_{\text{leaf,vis}} = 0.1; \quad \alpha_{\text{stem,vis}} = 0.16; \quad (29)$$

$$\tau_{\text{leaf,vis}} = 0.05; \quad \tau_{\text{stem,vis}} = 0.001; \quad (30)$$

$$\alpha_{\text{leaf,nir}} = 0.45; \quad \alpha_{\text{stem,nir}} = 0.39; \quad (31)$$

$$\tau_{\text{leaf,nir}} = 0.25; \quad \tau_{\text{stem,nir}} = 0.001, \quad (32)$$



235 where α is absorptivity, τ is transmissivity, 'vis' refers to visible radiation and 'nir' refers to near-infrared. These values were taken from the ones assigned to tropical trees by Oleson et al. (2004). Soil optical properties are from the dataset prepared by Lawrence and Chase (2007).

The PAR absorbed by the sunlit leaves of a cohort i is obtained as the sum over layers of the absorbed visible radiation weighted by the cohort's fractional leaf area index:

$$240 \quad \text{PAR}_{\text{sun}}^{(i)} = \sum_l S_{\text{sun,vis}}^{(l)} \frac{\text{LAI}^{(i,l)}}{\text{PAI}^{(l)}}. \quad (33)$$

The sunlit leaf and plant area indices of cohort i are obtained by aggregating over layers:

$$\text{LAI}_{\text{sun}}^{(i)} = \sum_l f_{\text{sun}}^{(l)} \text{LAI}^{(i,l)}; \quad (34)$$

$$\text{PAI}_{\text{sun}}^{(i)} = \sum_l f_{\text{sun}}^{(l)} [\text{LAI}^{(i,l)} + \text{SAI}^{(i,l)}]. \quad (35)$$

The sunlit plant area index for the whole canopy is calculated by summing over cohorts:

$$245 \quad \text{PAI}_{\text{sun,c}} = \sum_i \text{PAI}_{\text{sun}}^{(i)}. \quad (36)$$

Equations analogous to Eqs. (33) through (36) apply to the shaded parts of the canopy.

2.2.3 Longwave radiative transfer

The longwave radiation emitted by the sunlit part of the canopy is (Dai et al., 2004):

$$L_{\text{sun}} = \gamma_{\text{sun}} (2\sigma T_{\text{sun}}^4 - L^\downarrow - \sigma T_{\text{g}}^4); \quad (37)$$

250 where σ is the Stefan-Boltzmann constant, L^\downarrow is the incoming atmospheric longwave radiation, T_{sun} , and T_{g} are expressed in Kelvin, and

$$\gamma_{\text{sun}} = (1 - e^{-\text{PAI}_c}) \frac{\text{PAI}_{\text{sun,c}}}{\text{PAI}_c}. \quad (38)$$

The thermal emissivity of plants and soil is assumed to be 1. The net emission of longwave radiation by the shaded part of the canopy is described by analogous equations.

255 The longwave radiation emitted by the ground surface is

$$L_{\text{g}} = \sigma T_{\text{g}}^4 - \gamma_{\text{sun}} \sigma T_{\text{sun}}^4 - \gamma_{\text{sha}} \sigma T_{\text{sha}}^4 + (1 - \gamma_{\text{sun}} - \gamma_{\text{sha}}) L^\downarrow. \quad (39)$$

The bulk longwave radiation emitted by the land surface toward the atmosphere is:

$$260 \quad L^\uparrow = \gamma_{\text{sun}} \sigma T_{\text{sun}}^4 + \gamma_{\text{sha}} \sigma T_{\text{sha}}^4 + (1 - \gamma_{\text{sun}} - \gamma_{\text{sha}}) \sigma T_{\text{g}}^4. \quad (40)$$



2.2.4 Assimilation and stomatal conductance

Photosynthetic assimilation is now calculated within the subdaily energy balance routine. A net photosynthetic rate is computed for the sunlit and shaded leaves of each cohort separately. These rates are related to stomatal conductance through a semi-empirical model. As noted above, we implemented two selectable models. In the Ball-Berry model (Ball et al., 1987), stomatal conductance depends linearly on net assimilation and the fractional humidity at the leaf surface h_s , and inversely on CO_2 concentration at the leaf surface, c_s . The stomatal conductance for sunlit leaves of cohort i is:

$$g_{s,\text{sun}}^{(i)} = g_{\min} + g_{1,\text{BB}} \frac{A_{n,\text{sun}}^{(i)} h_{s,\text{sun}}}{c_{s,\text{sun}}}, \quad (41)$$

where $A_{n,\text{sun}}^{(i)}$ is the net photosynthetic rate per unit leaf area, g_{\min} is a minimum stomatal conductance, and g_1 is a PFT-specific parameter. The Medlyn model (Medlyn et al., 2011) is derived from the assumption that stomata optimize CO_2 uptake while minimizing water loss. In this model, stomatal conductance depends inversely on the square root of the vapor pressure deficit at the leaf surface, D_s . The stomatal conductance for sunlit leaves of cohort i is:

$$g_{s,\text{sun}}^{(i)} = g_{\min} + 1.6 \left(1 + \frac{g_{1,\text{Med}}}{\sqrt{D_{s,\text{sun}}}} \right) \frac{A_{n,\text{sun}}^{(i)}}{c_{s,\text{sun}}}. \quad (42)$$

Values of the parameters $g_{1,\text{BB}}$ and $g_{1,\text{Med}}$ for specific PFTs were obtained following Sellers et al. (1996) for the Ball-Berry model and De Kauwe et al. (2015) for the Medlyn model. Figure 3 shows the different behaviour of the stomatal conductance models as a function of D_s .

For a given cohort i , the total photosynthetic rate is limited by the maximum rate of carboxylation, $V_{\max}^{(i)}$, which depends linearly on the total amount of daily absorbed photosynthetic active radiation, $\text{PAR}_{\text{day}}^{(i)}$ (Haxeltine and Prentice, 1996):

$$V_{\max,\text{day}}^{(i)} = f_v(T_{\text{leaf,dt}}^{(i)}, \dots) \times \text{PAR}_{\text{day}}^{(i)}. \quad (43)$$

In this equation, $V_{\max,\text{day}}^{(i)}$ is expressed per unit patch area. This potential rate is calculated by LPJ-GUESS for every cohort daily (Fig 1). The slope of the relationship, f_v , depends on environmental factors, including temperature and leaf nitrogen content. The daytime-averaged leaf temperature, $T_{\text{leaf,dt}}^{(i)}$, is weighted by the daily averaged fractions of sunlit and shaded leaves for cohort i :

$$T_{\text{leaf,dt}}^{(i)} = \frac{1}{n_{\text{dt}}} \sum_{\text{dt}} \frac{\text{PAI}_{\text{sun}}^{(i)} T_{\text{sun}} + \text{PAI}_{\text{sha}}^{(i)} T_{\text{sha}}}{\text{PAI}^{(i)}}, \quad (44)$$

where n_{dt} is the number of daytime subdaily periods.

Separating the contributions to daily absorbed PAR from sunlit and shaded leaves, maximum carboxylation rates for the sunlit and shaded parts of the cohort are estimated as:

$$\begin{aligned} V_{\max,\text{sun,day}}^{(i)} &= f_v(T_{\text{leaf,dt}}^{(i)}, \dots) \times \text{PAR}_{\text{sun,day}}^{(i)} \\ V_{\max,\text{sha,day}}^{(i)} &= f_v(T_{\text{leaf,dt}}^{(i)}, \dots) \times \text{PAR}_{\text{sha,day}}^{(i)} \end{aligned} \quad (45)$$



where $\text{PAR}_{\text{sun,day}}^{(i)}$ and $\text{PAR}_{\text{sha,day}}^{(i)}$ are the total daily PAR absorbed by the sunlit and shaded leaves of cohort i , respectively.
 290 Combining Eqs. (43) and (45) yields, for sunlit leaves:

$$V_{\text{max,sun,day}}^{(i)} = V_{\text{max,day}}^{(i)} \frac{\text{PAR}_{\text{sun,day}}^{(i)}}{\text{PAR}_{\text{day}}^{(i)}}. \quad (46)$$

The maximum carboxylation rate per unit leaf area is then calculated as:

$$V_{\text{max,sun,leaf}}^{(i)} = 86400^{-1} \beta \frac{V_{\text{sun,day}}^{(i)}}{\text{LAI}_{\text{sun,dt}}^{(i)}}, \quad (47)$$

where $\text{LAI}_{\text{sun,dt}}^{(i)}$ is the daily-averaged sunlit LAI of cohort i , and we have introduced a factor β to limit the photosynthetic rate
 295 under conditions of water stress. The prefactor 86400^{-1} converts the rate from day^{-1} to s^{-1} . Analogous equations apply to shaded leaves.

The water stress factor β is formulated as a sum over soil layers of a water uptake function weighed by a PFT-specific vertical rooting profile:

$$\beta = \sum_j r^{(j)} W_{\text{av}}^{(j)}, \quad (48)$$

300 where $r^{(j)}$ is the fraction of roots in soil layer j . In order to study the impact of the β factor on the model predictions, we implemented four different options for the water uptake function $W_{\text{av}}^{(j)}$. In the Noah type (Niu et al., 2011), $W_{\text{av}}^{(j)}$ decreases linearly in each soil layer with volumetric water content $\theta^{(j)}$ down to the wilting point:

$$W_{\text{av}}^{(j)} = \frac{\theta^{(j)} - \theta_{\text{wilt}}}{\theta_{\text{fc}} - \theta_{\text{wilt}}}, \quad (49)$$

where θ_{wilt} and θ_{fc} are volumetric water content at wilting point and field capacity respectively. In LPJ-GUESS, the wilting
 305 point is assumed to be at a matric potential of $\psi_{\text{wilt}} = -45\text{m}$, and the corresponding soil water content is calculated following Prentice et al. (1992).

The CLM type water uptake function is formulated in terms of matric potential (Oleson et al., 2004):

$$W_{\text{av}}^{(j)} = \frac{\psi_{\text{wilt,CLM}} - \psi^{(j)}}{\psi_{\text{wilt,CLM}} - \psi_{\text{sat}}}, \quad (50)$$

where $\psi^{(j)}$ is the matric potential of layer j , ψ_{sat} is the matric potential at saturation, and $\psi_{\text{wilt,CLM}}$ is the matric potential
 310 at wilting point, set to -150m . In this case, the water uptake response is flatter than in the Noah-type case when the soil is wet, and decreases more steeply when the soil gets drier. We also implemented a modified version of the CLM-type uptake function, with the same functional form but using LPJ-GUESS's -45m wilting matric potential instead of CLM's -150m .

The SSiB type water uptake function is:

$$W_{\text{av}}^{(j)} = 1 - e^{-c_2 \ln[\psi_{\text{wilt}}/\psi^{(j)}]}, \quad (51)$$



315 where the parameter c_2 depends on PFT, and takes values between 4.36 and 6.37 (Xue et al., 1991). In this study, we set c_2 to a fixed value of 5.8 for all PFTs, which results in high β values in most of the water availability range, and a steep decrease when approaching the wilting point.

Figure 4 shows the behavior of the different formulations of $W_{av}^{(j)}$ as a function of volumetric water content.

2.2.5 Soil physics

320 In standard LPJ-GUESS, soil temperature is used in calculations related to ecosystem respiration and nitrogen cycling, while soil water content influences plant water uptake and evapotranspiration. Both quantities affect soil organic matter decomposition rates.

Soil temperature T_s is now calculated by solving the heat transport equation:

$$\frac{\partial T_s}{\partial t} = -\frac{1}{c_h} \frac{\partial}{\partial z} \left(\kappa_s \frac{\partial T_s}{\partial z} \right), \quad (52)$$

325 where $c_h(z)$ and $\kappa_s(z)$ are soil heat capacity and thermal conductivity respectively. The top boundary condition is given by the heat flux into the ground, G , calculated in the energy balance routine (Eq. 11). Heat flow through the bottom boundary is neglected. Thermal conductivity is calculated following the method of Johansen (1975, 1977). Soil heat capacity is computed as a weighted sum of the heat capacities of the dry soil, which depends on texture, and water (de Vries, 1963).

330 Vertical water transport in the soil column is described by the Richards equation (Richards, 1931), which can be expressed in the following form:

$$\frac{\partial \theta}{\partial t} = \frac{\partial}{\partial z} \left[\lambda_w \frac{\partial \theta}{\partial z} - \gamma_w \right] + S_\theta(z). \quad (53)$$

Here, θ is volumetric water content, $\lambda_w(\theta)$ is hydraulic diffusivity, $\gamma_w(\theta)$ is hydraulic conductivity, and $S_\theta(z)$ is a volumetric sink term that accounts for plant water uptake ($S_\theta \leq 0$). Hydraulic diffusivity and conductivity are calculated as a function of soil texture and soil water content by using the expressions derived by Clapp and Hornberger (1978) and Cosby et al. (1984).
335 Rain water that is not intercepted by the canopy infiltrates into the soil at a rate limited by the soil's infiltration capacity as given by the Green-Ampt equation (Green and Ampt, 1911). Free gravitational drainage is assumed at the bottom of the soil column.

340 Soil temperature, water content, ecosystem respiration, plant water uptake and evapotranspiration are calculated in the sub-daily loop. Equations (52) and (53) are solved with a Crank-Nicolson scheme (e.g. Press, 2003). Daily averages of water content and temperature over the layers corresponding to the standard LPJ-GUESS top and bottom layers are then used as inputs to the original soil organic matter and nitrogen cycling routines.



3 Model verification and evaluation

3.1 Model verification

The revised model was verified by performing energy and water conservation tests. At any given time step, the energy conser-
345 vation error per unit time and per unit patch area, Δu_{err} , is calculated as:

$$\Delta u_{\text{err}} = S^{\downarrow} + L^{\downarrow} - \langle L^{\uparrow} + H^{\uparrow} + \lambda E^{\uparrow} + \Delta u_{\text{soil}} \rangle, \quad (54)$$

where $\langle \cdot \rangle$ indicates an average over patches, and Δu_{soil} is the rate of change of energy stored in the soil column per unit patch
area ($\text{J m}^{-2} \text{s}^{-1}$). The latter is calculated as:

$$\Delta u_{\text{soil}} = \frac{1}{\Delta t} \sum_j c_h^{(j)} \Delta z^{(j)} T_s^{(j)}, \quad (55)$$

350 where Δt is the time step in seconds, and $c_h^{(j)}$, $\Delta z^{(j)}$ and $T_s^{(j)}$ are, respectively, the heat capacity, thickness and temperature
of soil layer j . Figure 5 (upper panel) shows the frequency of the energy conservation error relative to the energy input to the
system (i.e., the total incoming irradiance, $S^{\downarrow} + L^{\downarrow}$). The vast majority of the time steps ($\sim 98.4\%$) the error is smaller than is
0.25% of the incoming radiation. Errors larger than 1% of the incoming radiation occur $\sim 0.014\%$ of time steps, and the error
is never larger than 1.75% of the energy input.

355 The water conservation error is computed as:

$$\Delta w_{\text{err}} = P - \langle R + E^{\uparrow} + \Delta w_{\text{soil}} + \Delta w_c \rangle, \quad (56)$$

where P is precipitation, R is runoff (including surface runoff and base flow), E^{\uparrow} is evapotranspiration, Δw_{soil} is the change
in soil water content per unit patch area, per unit time, and Δw_c is the change in canopy water content. We found that the bulk
of the water conservation error is due to a generally small overestimation of canopy evaporation when the potential evaporation
360 at a given time step is substantially larger than the available canopy water. To assess the importance of this error in terms of
energy fluxes, we plotted it as a percentage of the energy input to the system (Fig. 5, lower panel). Water conservation errors
larger than 1% of the total energy input occur $\sim 0.35\%$ of the time steps, and errors larger than 5% of the energy input occur
 $\sim 0.006\%$ of the time steps.

We therefore conclude that the magnitude of the errors in energy balance closure and water conservation is negligible the
365 vast majority of time steps. Relatively larger errors in water conservation due to overestimation of canopy evaporation are small
in terms of total energy input.

3.2 Evaluation setup

We evaluated the revised model by comparing hourly and monthly simulated fluxes of sensible and latent heat, and annual CO_2
fluxes, with flux tower measurements from 21 FLUXNET2015 (Pastorello et al., 2020) sites. The current version of the model
370 does not simulate snow or frozen soil water, so we restricted our study to sites where the air temperature remained above 0°C



Table 1. Brief description of selected sites. The land cover classification was taken from the FLUXNET site description web pages. The reference level height is taken as the height of the measuring sensors above the canopy. A dash indicates that we weren't able to find an observed LAI value for the site.

Site	Code	Land Cover	z_{ref} (m)	LAI	Reference
Emerald, Australia	AU-Emr	C ₃ grassland	6.2	0.7	Schroder et al. (2014)
Amoladeras, Spain	ES-Amo	Open shrubland (C ₃ grassland)	3.5	-	López-Ballesteros et al. (2017)
Daly River Cleared, Australia	AU-DaP	C ₄ grassland	5	1.5	Hutley et al. (2011)
Sturt Plains, Australia	AU-Stp	C ₄ grassland	5	0.5	Beringer et al. (2011)
Tchizalamou, Congo	CG-Tch	Savanna (C ₄ grassland)	3.8	2.0	Merbold et al. (2009)
Sardinilla Pasture, Panama	PA-SPs	C ₄ grassland	2.91	5.4	Wolf et al. (2011b)
Daly River Savanna, Australia	AU-DaS	Savanna	5	1.5	Hutley et al. (2011)
Dry River, Australia	AU-Dry	Savanna	5	1.2	Beringer et al. (2011)
Demokeya, Sudan	SD-Dem	Savanna	4	0.9	Ardö et al. (2008)
Adelaide River, Australia	AU-Ade	Woody savanna	5	1.1	Beringer et al. (2011)
Gingin, Australia	AU-Gin	Woody savanna	7.8	0.9	Beringer et al. (2016)
Howard Springs, Australia	AU-How	Woody savanna	5	1.5	Beringer et al. (2011)
Red Dirt Melon Farms, Australia	AU-RDF	Woody savanna	5	1.6	Bristow et al. (2016)
Robson Creek, Australia	AU-Rob	Evergreen broadleaf forest	12	4.3	Beringer et al. (2016)
Santarem-Km67, Brazil	BR-Sa1	Evergreen broadleaf forest	13	6.5	Saleska et al. (2003)
Santarem-Km83, Brazil	BR-Sa3	Evergreen broadleaf forest	19	6.5	Saleska et al. (2003)
Guyaflex, French Guiana	GF-Guy	Evergreen broadleaf forest	23	5.9	Bonal et al. (2008)
Ankasa, Ghana	GH-Ank	Evergreen broadleaf forest	16	-	Stefani et al. (2009)
Pasoh forest, Malaysia	MY-PSO	Evergreen broadleaf forest	18	6.5	Kosugi et al. (2008)
Sardinilla Plantation, Panama	PA-SPn	Deciduous broadleaf forest	5	2.9	Wolf et al. (2011b)
Mongu, Zambia	ZM-Mon	Deciduous broadleaf forest	10	1.6	Merbold et al. (2009)

Table 2. Summary of the LPJ-GUESS/LSM simulations carried out. Simulations with different stomatal conductance schemes are arranged in columns: Ball-Berry (BB) and Medlyn (Med). Simulations with different water uptake function types are arranged in rows: NOAH, CLM, modified CLM and SSiB.

	Ball-Berry	Medlyn
NOAH	NOAH/BB	NOAH/Med
CLM	CLM/BB	CLM/Med
CLM (mod)	CLMm/BB	CLMm/Med
SSiB	SSiB/BB	SSiB/Med



throughout the measuring period. We additionally discarded wetland sites, which require a more detailed representation of soil and ground water hydrology (Wania et al., 2009). A list of the selected sites is presented in Table 1. The location of the sites is represented on the world map in Fig. 6.

For each site, we ran 8 simulations, covering all possible configurations of the water uptake functions and stomatal con-
375 ductance schemes described in Sec. 2.2.4 (Table 2). We used the climate data collected at the tower sites to force the model. Half-hourly forcing data was converted to hourly averages, and we set a lower boundary of 10% of the dataset median on the air humidity to correct for physically invalid negative values. Nitrogen deposition data is from Lamarque et al. (2013). Atmospheric CO₂ concentration data is from McGuire et al. (2001). Additionally, we ran a standard (non-LSM) LPJ-GUESS
380 simulation to compare both model versions' predictions of monthly evapotranspiration and a number of ecosystem structure and function variables. The number of replicate patches was set to 100 in all the simulations to avoid spurious effects of the stochastic ecosystem processes on the modeled fluxes.

All natural PFTs were allowed to establish in forest and savanna sites. Since the focus of the model evaluation was placed on the predicted turbulent fluxes, we restricted the simulated PFTs to grassy types at sites classified as grasslands, which limits modeled surface roughness. This was also done for Spain-Amoladeras and Congo-Tchizalamou. Amoladeras is classified as
385 an open shrubland on the FLUXNET reference, but the vegetation is short and the most abundant species is *Machrocloa Tenacissima*, a type of grass (López-Ballesteros et al., 2017). Tchizalamou, which is classified as savanna, is actually a C₄ grassland (Merbold et al., 2009).

The simulations were spun up for a standard period of 500 years from a bare ground state to bring C and N soil and vegetation pools to near-equilibrium with the climate (see, e.g., Smith et al., 2014). During the spin-up phase, the site climate spanning the
390 whole measurement period was repeated cyclically, with interannual trends in air temperature removed, and the atmospheric CO₂ concentration was kept at the level of the first year of observations at each site.

3.3 Analysis

Half-hourly measured fluxes were converted to hourly averages for direct comparison with model outputs. Subdaily FLUXNET data are classified into four quality categories: 0 (measured), 1 (good quality gap fill), 2 (poor quality gap fill) and 3 (downscale
395 from ERA reanalysis data). In our analysis, we only used subdaily fluxes with a quality flag of 0 or 1. For monthly and annual fluxes, the quality flag varies between 0 and 1, and indicates the fraction of the subdaily values in that month/year whose quality is either 0 or 1. We only used monthly and annual fluxes with a quality flag equal to or greater than 0.75. Following Stöckli et al. (2008), we further discarded fluxes with friction velocity $u^* < 0.2 \text{ms}^{-1}$ in order to avoid possibly biased eddy covariance measurements during periods of weak turbulence (Schroder et al., 2014).

To evaluate the agreement between measured and simulated turbulent heat fluxes at each site for all different model configurations we used standard statistical metrics: correlation coefficient (r), mean bias, and root mean square error (RMSE). We also considered the standard deviation of the modeled fluxes normalized by the standard deviation of the observed fluxes (σ_m/σ_o),
400 which provides a measure of the agreement between observed and simulated variability.



3.4 Results

405 3.4.1 Annual and diurnal cycles of turbulent heat fluxes

Figure 7 shows examples of simulated and observed monthly averages of turbulent and latent heat fluxes over the course of a year at four sites: Gingin (AU-Gin), Daly River Savanna (AU-DaS), Santarem Km67 (BR-Sa1) and Guyaflux (GF-Guy). Examples of the monthly-averaged diurnal cycle for the same sites are shown in Figs. 8 and 9. We chose these sites and years to illustrate situations with varying degrees of agreement between simulations and measurements. The simulated fluxes are
410 from the run using the CLM-type water uptake function and the Medlyn model of stomatal conductance.

At the AU-Gin site, the shape of the annual cycles of latent and sensible heat is similar to the observed (Fig. 7, upper left). Sensible heat is largest at the beginning of the year, decreases steeply to its minimum around June-July, and starts increasing again around August. The simulation agrees very well with measurements most of the year, but overestimates sensible heat by $\sim 40 \text{ Wm}^{-2}$ in the first two months. Observed latent heat dominates the turbulent exchange in the wet season (from May
415 to September). Simulated latent heat is overestimated by up to $\sim 25 \text{ Wm}^{-2}$ during the wet season. The shift from larger sensible heat to larger latent heat in May is well captured in the simulation, but, due to the overestimation of latent heat, the shift back to larger sensible heat flux at the beginning of the dry season is delayed by about a month with respect to the observations. The average simulated diurnal cycle of sensible heat is overestimated in January, peaking at $\sim 700 \text{ Wm}^{-2}$ (observed: $\sim 500 \text{ Wm}^{-2}$), while it agrees very well with observations in May and September, both in terms of magnitude and
420 day-to-day variability.

At the AU-DaS site (Fig. 7, upper right panel), the shapes of measured and simulated annual cycles match relatively well at the beginning and the end of the year, but diverge substantially during the dry season. Simulated monthly averages of latent heat are $\sim 20 \text{ Wm}^{-2}$ above measured values from March to May, and $\sim 30 \text{ Wm}^{-2}$ below the measurements between August and October. The average simulated diurnal cycle peaks at $\sim 300 \text{ Wm}^{-2}$ in May (observed: $\sim 175 \text{ Wm}^{-2}$), and at $\sim 30 \text{ Wm}^{-2}$
425 in September (observed: $\sim 150 \text{ Wm}^{-2}$; Fig. 8, lower half). This marked divergence from measured values happens in very dry periods, when the simulated soil moisture in the rooting zone drops close to the wilting point and there is not enough precipitation to replenish it until the start of the wet season. As a consequence, sensible heat is greatly overestimated. Simulated monthly averages rise sharply and peak at $\sim 120\text{--}140 \text{ Wm}^{-2}$ from September to October, while measured values stay at $\sim 60 \text{ Wm}^{-2}$ throughout the dry season. The average sensible heat diurnal cycle peaks at $\sim 530 \text{ Wm}^{-2}$ in September, while
430 the observed average diurnal peak is slightly under $\sim 300 \text{ Wm}^{-2}$ (Fig. 8).

Monthly averages of sensible and latent heat at the BR-Sa1 tropical rainforest site show little variability throughout the year (Fig. 7, lower left). Measured sensible heat flux stays at $\sim 20 \text{ Wm}^{-2}$ for most of the year, and increases to $\sim 30 \text{ Wm}^{-2}$ around August and September, when measured precipitation reaches its minimum. During this period, the soil retains enough moisture in the rooting zone to maintain average latent heat levels at $\sim 80\text{--}90 \text{ Wm}^{-2}$. Sensible and latent heat fluxes are systematically
435 overestimated by the model by $\sim 10\text{--}20 \text{ Wm}^{-2}$. Average sensible heat flux peaks daily between $\sim 170\text{--}230 \text{ Wm}^{-2}$ (measured: $\sim 100 \text{ Wm}^{-2}$). Latent heat flux peaks daily between $\sim 300\text{--}370 \text{ Wm}^{-2}$ (measured: $\sim 280\text{--}320 \text{ Wm}^{-2}$, Fig. 9).



Table 3. Model performance statistics for simulated hourly (left) and monthly (right) sensible heat fluxes for the CLM/BB and the CLM/Med simulations. Bold fonts indicate the model configuration that performed better. The mean and standard deviation of the observed fluxes (\bar{H}_o and σ_o , respectively), shown for reference, are given in Wm^{-2} . The RMSE and Bias have been normalized by the mean of the observed fluxes for easier cross-site comparison.

Site	$\bar{H}_o (\sigma_o)$	r	Hourly			Monthly				
			σ_m/σ_o	nRMSE	nBias	$\bar{H}_o (\sigma_o)$	r	σ_m/σ_o	nRMSE	nBias
			BB Med	BB Med	BB Med	BB Med	BB Med	BB Med	BB Med	BB Med
AU-Emr	110 (108)	0.93 0.92	1.4 1.3	0.7 0.6	0.3 0.3	57 (20)	0.89 0.85	1.4 1.3	0.4 0.4	0.3 0.3
ES-Amo	103 (133)	0.96 0.94	1.5 1.5	0.8 0.9	0.1 0.0	67 (42)	0.96 0.96	1.7 1.8	0.5 0.6	0.0 0.0
AU-DaP	124 (122)	0.90 0.90	1.2 1.2	0.6 0.5	0.3 0.2	56 (29)	0.78 0.85	0.8 1.0	0.5 0.3	0.3 0.2
AU-Stp	118 (121)	0.96 0.94	1.3 1.3	0.5 0.5	0.3 0.2	66 (19)	0.88 0.88	1.2 1.4	0.3 0.3	0.3 0.2
CG-Tch	98 (74)	0.88 0.86	1.2 1.0	0.4 0.4	0.1 0.0	38 (11)	0.62 0.55	0.5 0.4	0.2 0.3	0.0 -0.1
PA-SPs	104 (96)	0.89 0.85	1.3 1.2	0.7 0.7	0.5 0.3	26 (19)	0.94 0.93	1.2 1.1	0.6 0.5	0.6 0.4
AU-DaS	86 (117)	0.92 0.91	1.5 1.5	1.2 1.0	0.6 0.5	53 (16)	0.73 0.77	1.6 2.1	0.7 0.6	0.6 0.4
AU-Dry	94 (117)	0.94 0.92	1.7 1.5	1.5 1.1	1.0 0.7	56 (21)	0.87 0.80	1.2 1.3	1.1 0.8	1.0 0.8
SD-Dem	78 (107)	0.92 0.89	1.8 1.3	1.5 0.8	0.7 0.2	53 (16)	0.03 0.12	0.7 0.7	0.7 0.4	0.6 0.2
AU-Ade	74 (107)	0.91 0.92	1.6 1.5	1.3 1.0	0.6 0.4	50 (19)	0.82 0.87	1.4 1.8	0.6 0.5	0.5 0.3
AU-Gin	111 (159)	0.96 0.96	1.3 1.3	0.6 0.6	0.2 0.1	73 (44)	0.99 0.98	1.3 1.4	0.3 0.3	0.2 0.1
AU-How	71 (102)	0.88 0.90	1.7 1.6	1.6 1.3	0.9 0.7	41 (22)	0.79 0.84	1.1 1.4	1.0 0.8	0.9 0.7
AU-RDF	109 (114)	0.90 0.89	1.7 1.5	1.1 0.9	0.5 0.3	59 (14)	0.10 0.37	1.4 1.9	0.6 0.5	0.4 0.2
AU-Rob	49 (96)	0.93 0.92	1.7 1.6	2.0 1.8	1.1 0.9	32 (26)	0.97 0.94	1.4 1.6	1.3 1.2	1.2 1.0
BR-Sa1	35 (60)	0.85 0.86	1.9 1.7	2.3 1.8	1.1 0.8	20 (4)	0.58 0.53	3.2 2.6	1.3 0.9	1.2 0.8
BR-Sa3	42 (59)	0.91 0.90	2.2 2.0	2.5 2.2	1.6 1.3	22 (5)	0.87 0.83	2.5 3.1	1.7 1.5	1.6 1.3
GF-Guy	36 (78)	0.92 0.92	1.7 1.5	2.3 2.0	1.4 1.2	22 (17)	0.95 0.93	1.1 1.1	1.6 1.3	1.6 1.3
GH-Ank	37 (65)	0.84 0.84	1.4 1.3	1.5 1.3	0.5 0.3	24 (9)	0.47 0.48	1.1 1.1	0.6 0.5	0.5 0.3
MY-PSO	87 (117)	0.94 0.93	1.2 1.0	0.7 0.5	0.4 0.1	45 (10)	0.88 0.84	0.9 0.7	0.5 0.3	0.5 0.2
PA-SPn	87 (95)	0.91 0.91	1.6 1.5	1.2 1.0	0.7 0.6	29 (15)	0.93 0.93	1.1 1.1	0.9 0.8	0.9 0.7
ZM-Mon	62 (120)	0.93 0.90	1.5 1.4	1.6 1.5	0.9 0.7	48 (15)	0.18 0.28	1.4 1.7	1.0 0.9	0.9 0.8
Average	82 (103)	0.91 0.90	1.5 1.4	1.3 1.1	0.7 0.5	45 (19)	0.73 0.74	1.3 1.5	0.8 0.6	0.7 0.5

At the GF-Guy site, another tropical rainforest, monthly averages of sensible heat are overestimated by $\sim 20 \text{ Wm}^{-2}$ throughout the year, while latent heat flux is underestimated by about the same amount. The simulated sensible heat diurnal cycle peaks, on average, $\sim 100 \text{ Wm}^{-2}$ above the measured values, while the peak of the simulated latent heat diurnal cycle is $\sim 130 \text{ Wm}^{-2}$ below measured values. There is a marked decrease in simulated latent heat in October, and a corresponding sharp increase in sensible heat, due to excessively low soil moisture in the rooting zone in the model. The simulated October average diurnal sensible heat cycle peaks at $\sim 350 \text{ Wm}^{-2}$ (measured: $\sim 200 \text{ Wm}^{-2}$), while the average latent heat diurnal cycle peaks at $\sim 200 \text{ Wm}^{-2}$.

3.4.2 Influence of different stomatal conductance schemes

Table 3 and Fig. 10 show model performance statistics for sensible heat fluxes, for the CLM/BB and the CLM/Med simulations. Correlations between modeled and observed sensible heat fluxes are very high, and similar for both runs. For hourly fluxes, r is between $\sim 0.85-0.92$. Correlations between monthly averaged fluxes are weaker, but still high at most sites ($r > 0.75$), but they are very low for SD-Dem, AU-RDF and ZM-Mon. The correlation is lowest at SD-Dem, but the RMSE and Bias are lower for



Table 4. Model performance statistics for simulated hourly (left) and monthly (right) latent heat fluxes for the CLM/BB and the CLM/Med simulations. Bold fonts indicate the model configuration that performed better. The mean and standard deviation of the observed fluxes ($\lambda\bar{E}_o$ and σ_o , respectively), shown for reference, are given in Wm^{-2} . The RMSE and Bias have been normalized by the mean of the observed fluxes for easier cross-site comparison.

Site	$\lambda\bar{E}_o(\sigma_o)$	r	CLM/BB			CLM/Med			$\lambda\bar{E}_o(\sigma_o)$	r	CLM/BB			CLM/Med		
			σ_m/σ_o	nRMSE	nBias	σ_m/σ_o	nRMSE	nBias			σ_m/σ_o	nRMSE	nBias	σ_m/σ_o	nRMSE	nBias
			BB Med	BB Med	BB Med	BB Med	BB Med			BB Med	BB Med	BB Med	BB Med	BB Med	BB Med	BB Med
AU-Emr	50 (51)	0.61 0.59	1.5 1.7	1.3 1.5	0.3 0.4			29 (13)	0.78 0.76	2.0 2.3	0.7 0.8	0.4 0.4				
ES-Amo	20 (25)	0.72 0.66	2.3 3.1	2.7 3.7	1.5 1.6			14 (7)	0.62 0.66	2.2 3.4	1.6 2.0	1.3 1.4				
AU-DaP	93 (122)	0.84 0.84	0.9 1.2	0.7 0.9	0.0 0.2			53 (45)	0.92 0.93	0.9 1.1	0.3 0.4	0.0 0.2				
AU-Stp	68 (87)	0.82 0.79	1.2 1.5	0.9 1.1	0.0 0.1			43 (35)	0.92 0.92	1.2 1.3	0.4 0.5	0.1 0.1				
CG-Tch	86 (81)	0.85 0.83	1.0 1.2	0.5 0.7	0.1 0.3			40 (22)	0.93 0.90	0.8 0.9	0.2 0.3	0.1 0.2				
PA-SPs	208 (127)	0.85 0.78	0.8 1.1	0.4 0.5	-0.3 - 0.2			75 (18)	0.71 0.70	0.7 0.9	0.3 0.2	-0.2 - 0.1				
AU-DaS	100 (101)	0.80 0.83	0.8 1.2	0.6 0.7	-0.2 - 0.1			67 (24)	0.84 0.87	1.3 1.8	0.3 0.4	-0.2 0.0				
AU-Dry	92 (94)	0.81 0.75	0.8 1.4	0.6 1.0	-0.2 - 0.1			58 (28)	0.85 0.83	1.1 1.7	0.3 0.5	-0.2 - 0.1				
SD-Dem	54 (75)	0.85 0.82	0.6 1.1	0.9 0.9	-0.3 - 0.2			40 (33)	0.94 0.95	0.6 1.0	0.5 0.4	- 0.3 - 0.3				
AU-Ade	120 (133)	0.84 0.90	0.8 1.0	0.6 0.5	-0.2 - 0.1			85 (37)	0.91 0.94	0.9 1.2	0.2 0.2	-0.2 0.0				
AU-Gin	63 (60)	0.72 0.75	1.0 1.3	0.7 0.8	0.0 0.1			43 (16)	0.77 0.76	1.1 1.7	0.3 0.4	0.0 0.1				
AU-How	139 (134)	0.84 0.86	0.6 0.8	0.7 0.6	-0.3 - 0.2			88 (28)	0.87 0.87	0.8 1.2	0.4 0.3	-0.3 - 0.2				
AU-RDF	82 (104)	0.72 0.73	0.8 1.2	0.9 1.1	0.1 0.4			49 (39)	0.81 0.75	0.7 1.1	0.5 0.7	0.2 0.5				
AU-Rob	104 (94)	0.73 0.75	0.9 1.1	0.7 0.7	-0.2 - 0.1			80 (14)	0.20 0.19	0.8 1.1	0.4 0.3	-0.3 - 0.2				
BR-Sa1	132 (134)	0.86 0.89	1.0 1.1	0.5 0.5	0.1 0.2			87 (13)	0.64 0.76	0.6 0.8	0.1 0.2	0.1 0.2				
BR-Sa3	161 (142)	0.82 0.83	0.6 0.7	0.6 0.6	- 0.3 - 0.3			95 (10)	0.40 0.38	1.1 1.6	0.3 0.3	-0.3 - 0.2				
GF-Guy	162 (152)	0.87 0.88	0.6 0.7	0.6 0.6	-0.4 - 0.3			109 (11)	0.55 0.55	0.8 1.1	0.4 0.3	- 0.3 - 0.3				
GH-Ank	72 (114)	0.65 0.66	0.8 0.8	1.2 1.2	0.0 0.1			51 (21)	0.02 0.07	0.6 0.6	0.5 0.5	0.1 0.1				
MY-PSO	169 (151)	0.89 0.93	0.6 0.7	0.6 0.4	-0.4 - 0.2			97 (7)	0.73 0.65	0.7 1.0	0.3 0.2	-0.3 - 0.2				
PA-SPn	195 (127)	0.83 0.85	0.6 0.7	0.5 0.5	-0.4 - 0.3			88 (16)	0.72 0.77	0.6 0.7	0.4 0.3	-0.4 - 0.3				
ZM-Mon	72 (88)	0.69 0.68	0.6 1.0	1.0 1.1	-0.5 - 0.3			59 (22)	0.44 0.59	1.0 1.5	0.6 0.6	-0.5 - 0.4				
Average	107 (105)	0.79 0.79	0.9 1.2	0.8 0.9	-0.1 0.0			64 (22)	0.69 0.70	1.0 1.3	0.4 0.5	-0.1 0.0				

the CLM/Med run. At AU-RDF and ZM-mon, the CLM/Med simulation shows better correlations and smaller errors than the
 450 one using the BB scheme.

The model tends to overestimate average sensible heat. The hourly and monthly mean bias are non-negative at all sites
 (except at CG-Tch for monthly fluxes, where it is slightly negative), but normalized RMSE and mean bias are smaller for the
 CLM/Med run at most sites. The simulations seem to perform comparatively better in grasslands; for the Med simulation,
 RMSE is between 0.4 and 0.8 of the sample average (hourly fluxes), whereas it is in the 0.6–1.3 range at savanna sites, and in
 455 the 0.5–2.2 range for forest sites.

The variability of sensible heat flux is also overestimated by the model. In this case, the CLM/Med run performs better than
 the CLM/BB one for hourly fluxes, but the situation is the reversed for monthly average fluxes. Again, the simulations show
 better performance in grassland sites; for hourly fluxes, the Med simulation predicts $\sigma_m/\sigma_o \sim 1$ –1.5 in grasslands, ~ 1.3 –1.6
 in savanna sites, and ~ 1.0 –2.2 in forest sites.

460 Model performance statistics for latent heat fluxes are presented in Table 4 and Fig. 11. Correlations for hourly fluxes are
 between 0.7 and 0.9 for most sites. For monthly fluxes, correlations are poorer at forest sites, but errors are comparatively



Table 5. Cross-site averaged model performance statistics for simulated hourly and monthly sensible and latent heat fluxes. RMSE and Bias are given in Wm^{-2} . Bold fonts indicate the best performing simulations in each metric.

	<i>H</i>				λE			
<i>Hourly averages</i>	<i>r</i>	σ_m/σ_o	RMSE	Bias	<i>r</i>	σ_m/σ_o	RMSE	Bias
Noah/BB	0.92	1.6	95	49	0.77	0.9	79	-24
CLM/BB	0.91	1.5	88	44	0.79	0.9	74	-19
CLM(mod)/BB	0.92	1.6	90	47	0.79	0.9	74	-22
SSiB/BB	0.91	1.6	88	45	0.79	0.9	74	-20
Noah/Med	0.92	1.5	83	40	0.81	1.0	72	-15
CLM/Med	0.90	1.4	75	31	0.79	1.2	76	-8
CLM(mod)/Med	0.91	1.5	78	35	0.80	1.1	74	-11
SSiB/Med	0.91	1.4	77	32	0.79	1.2	77	-9
<i>Monthly averages</i>	<i>r</i>	σ_m/σ_o	RMSE	Bias	<i>r</i>	σ_m/σ_o	RMSE	Bias
Noah/BB	0.75	1.5	33	28	0.65	1.2	27	-12
CLM/BB	0.73	1.3	30	25	0.69	1.0	24	-10
CLM(mod)/BB	0.74	1.4	31	26	0.71	1.0	24	-12
SSiB/BB	0.74	1.4	30	25	0.69	1.0	24	-11
Noah/Med	0.77	1.6	29	23	0.70	1.2	24	-8
CLM/Med	0.74	1.5	26	18	0.70	1.3	24	-4
CLM(mod)/Med	0.75	1.6	27	20	0.71	1.3	24	-6
SSiB/Med	0.75	1.5	26	18	0.70	1.4	25	-5
LPJ-GUESS	-	-	-	-	0.64	1.6	27	-5

small; normalized RMSE is in the 0.1–0.5 range. Hourly correlations are rather similar for both model configurations at most sites.

Latent heat fluxes tend to be underestimated in forest and savanna sites, and overestimated over grasslands. The CLM/BB configuration seems to perform better at grassland sites, while the CLM/Med configuration performs better at forest sites. Results for savanna sites are mixed in terms of RMSE, but the CLM/Med scheme yields somewhat smaller biases.

The variability of simulated latent heat fluxes is always larger in the CLM/Med run than in the CLM/BB run. Over C_3 grasslands, both LSM runs predict a much larger variability than observed. This may be in part due to the fact that observed variability at these sites is very low in absolute terms. At savanna and woody savanna sites, the CLM/Med run predicts a larger variability than observed, both in the hourly and monthly cases, whilst the CLM/BB simulation tends to produce a lower variability. For forest sites, both runs yield $\sigma_m \lesssim \sigma_o$, with the exception of BR-Sa3 in the CLM/Med run, where the variability of the monthly fluxes is ~ 1.6 times larger than observed. On average, the CLM/BB simulation shows better agreement with measured variability over grasslands, while CLM/Med performs somewhat better at forest sites.



3.4.3 Alternative model configurations

475 To evaluate the overall performance of the different model configurations, we considered the cross-site averaged statistics of each simulation (Table 5). Since the covered period differs across sites, this method ensures all sites contribute equally to the result.

Figure 12 shows the cross-site averaged metrics on a Taylor diagram. The clumping and clear separation of simulations using different stomatal conductance schemes suggests that this component of the model has a significantly greater influence than the soil water uptake function on the behaviour of the model, with the exception of the linear (Noah-type) parametrization, which is much more restrictive than the other three in terms of water uptake. In this case, both the BB and Med simulations seem to perform similarly regarding monthly latent heat fluxes, with the variability of the modeled fluxes somewhere in between the BB and Med clumps.

Simulated sensible heat fluxes display similar correlation with observations in all runs. The correlation coefficient is very high ($r \sim 0.9$) for hourly fluxes, and moderately high ($r \sim 0.75$) for monthly averages.

Sensible heat is overestimated in all model configurations; the average bias is always positive, but the Med simulations perform better in this respect. In the case of hourly averages, BB runs show an average bias of $\sim 46 \text{ Wm}^{-2}$, while the average value for Med runs is $\sim 35 \text{ Wm}^{-2}$. Average errors are also smaller in Med simulations. For hourly fluxes, the average RMSE is $\sim 90 \text{ Wm}^{-2}$ for BB runs, and $\sim 70 \text{ Wm}^{-2}$ for Med runs. For monthly fluxes, RMSE averages are $\sim 31 \text{ Wm}^{-2}$ and $\sim 27 \text{ Wm}^{-2}$ respectively.

The model also generally overestimates the variability of sensible heat. For hourly fluxes, the standard deviation of the sample is, on average, ~ 1.6 times greater than the measurements for the BB runs, and ~ 1.5 for the Med runs. In the case of monthly variability, BB runs perform better; the average standard deviations of modeled fluxes are ~ 1.4 and ~ 1.6 for BB and Med runs respectively.

495 Correlations between modeled and measured latent heat fluxes are lower than for sensible heat; $r \sim 0.8$ for hourly fluxes and ~ 0.7 for monthly fluxes. All runs show similar RMSE; $\sim 75 \text{ Wm}^{-2}$ and $\sim 24 \text{ Wm}^{-2}$ for hourly and monthly fluxes respectively. Latent heat is underestimated on average in all configurations. However, the Med runs perform significantly better than the BB runs on this metric. The average bias is $\sim -11 \text{ Wm}^{-2}$ (BB: $\sim -21 \text{ Wm}^{-2}$) for hourly fluxes, and $\sim -6 \text{ Wm}^{-2}$ (BB: $\sim -11 \text{ Wm}^{-2}$) for monthly fluxes. The variability of hourly latent heat fluxes is underestimated in the BB runs by about the same amount that it is overestimated in the Med runs, but in the case of monthly fluxes, BB simulations seem to reproduce the measured variability better ($\sigma_m \sim \sigma_o$, while $\sigma_m \sim 1.3\sigma_o$ for Med runs).

505 Monthly averages of latent heat simulated by the non-LSM version of LPJ-GUESS show a slightly worse correlation with measurements than the LSM version of the model. The average bias is $\sim -5 \text{ Wm}^{-2}$, in line with Med simulations and lower than BB simulations, and the RMSE is slightly higher, but close to the LSM runs. However, the predicted variability is significantly exaggerated; the standard deviation of the sample of modeled fluxes is, on average, ~ 1.6 times larger than observed.



Table 6. Foliar projective cover, averaged over the whole simulated period, of the plant functional types predicted for each site, given as a percentage. The LSM simulations use the CLM type water uptake factor. The dominant PFT for each site is highlighted in bold font.

Site	TeBE			TrBR			TrIBE			TrBE			C3G			C4G		
	LPJ-G	BB	Med	LPJ-G	BB	Med	LPJ-G	BB	Med	LPJ-G	BB	Med	LPJ-G	BB	Med	LPJ-G	BB	Med
AU-Emr	-	-	-	-	-	-	-	-	-	-	-	-	-	-	-	-	-	-
ES-Amo	-	-	-	-	-	-	-	-	-	-	-	-	61	23	24	-	-	-
AU-DaP	-	-	-	-	-	-	-	-	-	-	-	-	1	-	-	82	94	95
AU-Stp	-	-	-	-	-	-	-	-	-	-	-	-	1	-	-	71	56	57
CG-Tch	-	-	-	-	-	-	-	-	-	-	-	-	1	-	-	88	98	98
PA-SPs	-	-	-	-	-	-	-	-	-	-	-	-	-	-	-	95	98	98
AU-DaS	-	-	-	11	33	21	4	14	4	10	3	5	-	-	-	61	30	54
AU-Dry	-	-	-	7	28	-	2	6	1	2	3	2	1	-	-	64	36	85
SD-Dem	-	-	-	1	9	-	1	2	-	8	6	5	-	-	-	38	21	45
AU-Ade	-	-	-	7	28	22	3	12	3	5	3	6	1	-	-	63	37	52
AU-Gin	43	41	31	-	-	-	-	-	-	-	-	-	9	7	7	-	-	-
AU-How	-	-	-	21	40	31	7	16	12	20	3	5	-	-	-	41	23	40
AU-RDF	-	-	-	10	37	21	4	15	9	4	4	8	1	-	-	68	20	45
AU-Rob	-	-	-	57	54	45	29	23	22	2	1	3	-	-	-	4	9	10
BR-Sa1	-	-	-	66	65	63	28	12	23	2	3	6	-	-	-	8	6	6
BR-Sa3	-	-	-	51	50	44	23	21	21	4	5	3	-	-	-	7	14	11
GF-Guy	-	-	-	57	54	50	35	22	23	3	2	3	-	-	-	7	12	12
GH-Ank	-	-	-	61	63	59	24	26	20	2	6	7	1	-	-	8	3	8
MY-PSO	-	-	-	53	64	56	26	15	24	4	4	14	-	-	-	7	6	5
PA-SPn	-	-	-	60	57	51	27	20	20	2	1	4	-	-	-	6	8	12
ZM-Mon	2	-	-	3	23	4	3	4	3	3	4	5	2	1	1	54	44	75



Table 7. List of Plant Functional Types in the standard configuration of LPJ-GUESS (only PFTs predicted by the simulations in this study are listed)

Plant functional type	Abbreviation
Temperate Broadleaf Evergreen	TeBE
Tropical Broadleaf Raingreen	TrBR
Tropical shade-Intolerant Broadleaf Evergreen	TrIBE
Tropical Broadleaf Evergreen	TrBE
C ₃ Grass	C3G
C ₄ Grass	C4G

3.4.4 Ecosystem structure and function

We compared the predictions of the CLM/BB and the CLM/Med simulations to standard LPJ-GUESS for species composition and a number of ecosystem structure and function variables.

Table 6 shows the FPC of the simulated PFTs (Table 7) at each site. All three simulations predict the same type of grass at 510 grassland sites. At AU-Emr, the grass coverage predicted by the LSM runs is substantially lower than in standard LPJ-GUESS. Land surface model simulations predict a larger FPC at most C₄ grassland sites, except at AU-Stp, where FPC is ~ 20% smaller than in the LPJ-GUESS simulation.

All three simulations predict a temperate forest with a C₃ grassy understory at AU-Gin. At the rest of the savanna and woody 515 savanna sites, the three runs predict a mixture of tropical trees and C₄ grasses with a relatively high proportion of the latter. C₄ grass is the dominant PFT in the standard LPJ-GUESS and Med simulations, while in the BB simulations the tree coverage is close to or larger than that of grasses. In the standard LPJ-GUESS run, the simulated landscape is closer to the savanna IGBP classification at most sites (tree coverage lower than 30%). The BB simulation predicts a woody savanna (tree coverage higher than 30%) at all sites except for SD-Dem, while the Med simulation predicts the expected landscape at all sites (Table 1) except for AU-DaS, where it produces a woody savanna.

At the forest sites, all three simulations predict a mixture of tropical trees and C₄ grass, where the coverage of the latter is 520 relatively small. The dominant PFT is TrBR, taking between 50 and 65% of the coverage area. A similar prediction is made for the PA-SPn site, which is classified as a deciduous broadleaf forest. However, for the ZM-Mon site, also a deciduous forest, all three models yield a PFT composition that is closer to that of savanna sites.

Model predictions for the rest of the selected variables are shown in Table 8. The two C₃ grassland sites show different 525 behaviour with respect to ecosystem productivity and respiration. At AU-Emr, LSM simulations predict substantially lower gross primary production (GPP) and autotrophic respiration (R_a) than standard LPJ-GUESS, which results in lower estimates of net primary production (NPP). This site is a net carbon source (positive net ecosystem exchange, NEE) in all three simulations, which agrees with observations. Modelled LAI is lower in the LSM simulations, and much closer to the observed value. At ES-



Table 8. Comparison of selected variables related to simulated ecosystem structure and function between standard LPJ-GUESS and the LSM version at the selected sites. The LSM values are from the CLM/BB and the CLM/Med simulations. Gross primary production (GPP), autotrophic respiration (Ra), net primary production (NPP), heterotrophic respiration (Rh) and net ecosystem exchange (NEE) are given in $\text{gCm}^{-2}\text{y}^{-1}$. Bold fonts in the LAI and NEE columns indicate the closest match to the observed value. Bold fonts in the rest of the columns indicate the LSM prediction closest to standard LPJ-GUESS.

Site	LAI			GPP			Ra			NPP			Rh			NEE			
	Obs	LPJ-G	BB	Med	LPJ-G	BB	Med	LPJ-G	BB	Med	LPJ-G	BB	Med	LPJ-G	BB	Med	LPJ-G	BB	Med
AU-Emr	0.7	2.0	0.6	0.6	1184	431	414	922	360	330	303	104	93	53	41	33	10		
ES-Amo	-	2.0	2.3	2.1	767	976	850	479	666	540	288	310	310	262	254	233	182	-27	-55
Average	0.7	2.0	1.4	1.3	976	704	632	700	513	435	275	190	197	283	179	163	118	7	-11
AU-Dnp	1.5	4.0	6.9	7.8	976	1544	1888	296	611	693	681	933	1194	544	807	973	-210	-137	-126
AU-Sip	0.5	3.0	1.8	2.0	896	548	692	294	215	246	602	333	446	559	299	397	-52	-43	-34
CG-Tch	2.0	4.5	11.3	11.5	1020	1965	2019	336	757	780	682	1208	1238	596	1089	1116	-148	-86	-118
PA-SFs	5.4	6.5	10.7	10.9	1447	2026	2099	536	794	823	912	1232	1276	836	1133	1169	277	-76	-98
Average	2.4	4.5	7.7	8.1	1084	1521	1674	365	594	636	719	926	1039	634	832	914	-33	-86	-94
AU-DaS	1.5	3.4	3.7	4.2	966	1123	1242	332	541	518	633	582	724	470	425	521	-284	-164	-157
AU-Dry	1.2	2.8	3.3	4.7	826	1015	1286	263	476	436	563	538	850	428	388	689	-307	-137	-150
SD-Dem	0.9	1.3	1.2	1.3	460	421	543	173	195	190	287	225	351	246	189	315	-73	-42	-36
Average	1.2	2.5	2.7	3.4	751	853	1024	256	404	381	495	449	642	381	334	508	-221	-114	-115
AU-Adc	1.1	2.8	3.9	4.2	764	1126	1206	235	530	518	529	595	688	400	448	528	-272	-130	-148
AU-Gin	0.9	1.8	1.9	1.5	1178	1346	1216	914	1109	996	264	236	220	233	234	196	-317	-80	-1
AU-Hew	1.5	3.6	4.0	4.4	1073	1223	1298	427	603	588	647	620	710	476	487	529	-692	-171	-133
AU-RDF	1.6	3.4	3.8	4.2	915	1212	1267	300	633	574	614	579	692	515	492	589	329	-99	-87
Average	1.3	2.9	3.4	3.6	983	1227	1247	469	719	669	514	507	578	406	415	460	-238	-107	-92
AU-Rob	4.3	4.7	4.9	4.7	1650	1663	1668	775	800	809	873	861	859	613	626	642	-744	-260	-236
BR-Sai	6.5	6.4	5.2	5.7	2266	1910	2022	1137	1038	1058	1130	873	963	939	740	853	-4	-190	-134
BR-Ss3	6.5	4.5	4.8	4.5	1599	1505	1567	794	739	798	805	766	770	647	646	601	-105	-159	-120
GF-Guy	5.9	5.5	5.2	5.1	1926	1753	1815	942	882	924	983	871	891	760	683	695	-157	-223	-187
GH-Ank	-	5.4	5.2	5.1	1779	1648	1665	860	844	869	920	803	796	876	701	776	-	-44	-103
MY-PSO	6.5	5.5	4.6	5.2	2039	1619	1805	993	859	913	1046	759	892	841	616	739	-971	-205	-144
Average	5.9	5.3	5.0	5.1	1876	1683	1757	917	860	895	959	822	862	779	669	718	-396	-180	-154
PA-SPh	2.9	5.0	4.7	4.8	1654	1550	1605	816	803	810	839	747	794	764	606	640	-458	-75	-143
ZM-Mon	1.6	2.2	3.5	4.2	621	1002	1101	202	399	370	418	603	731	312	433	581	143	-107	-171
Average	2.3	3.6	4.1	4.5	1137	1276	1353	509	601	590	629	675	762	538	519	611	-157	-91	-157



530 Amo, GPP is enhanced in the LSM versions, while heterotrophic respiration (R_h) is low compared to standard LPJ-GUESS, resulting in a slightly enhanced carbon sink in the LSM simulations.

At three out of four C_4 grassland sites, the LSM simulations generate ~ 50 to 100% higher GPP than LPJ-GUESS. LAI is extremely high (between ~ 7 and ~ 11), and much higher than the observed values. R_a increases too, but not as much, in absolute terms, as GPP. This results in an increased NPP in the LSM simulations ($\sim 30\%$ in the BB run and $\sim 45\%$ in the Med run, Fig. 13, upper panels). R_h is also enhanced with respect to standard LPJ-GUESS, but again not as much as NPP, so the CO_2 sink is strengthened in both LSM runs (Fig. 13, lower panels). Simulations at the AU-Stp site again show a pattern different to the other C_4 grassland sites; GPP and NPP simulated in the LSM runs are both lower than in the non-LSM simulation. However, NPP is substantially higher in the Med simulation than in the BB simulation. This results in NEE being less negative than in LPJ-GUESS for the BB simulation and more negative than LPJ-GUESS for Med. NEE values predicted by the Med simulation are closest to the observed fluxes, except at PA-SPs, where all simulations fail to predict a net CO_2 source.

The BB and Med simulations also behave differently at savanna and woody savanna sites. At most sites, BB predicts LAI values similar to LPJ-GUESS, while Med produces higher LAIs. Both GPP and R_a increase in the LSM runs, but in the BB simulation the comparatively larger increase in R_a results in an NPP decrease $\sim 8\%$ for savanna and $\sim 2\%$ for woody savanna with respect to LPJ-GUESS. In the Med simulation, the absolute GPP increase is larger than that of R_a , which results in an NPP increase of $\sim 30\%$ for savanna and $\sim 12\%$ for woody savanna relative to the LPJ-GUESS simulation (Fig. 13, upper panels). In the BB simulation, R_h is $\sim 12\%$ smaller than the LPJ-GUESS prediction in savanna sites, and close to LPJ-GUESS in woody savanna sites, which yields similar NEE averages for savanna sites, but a $\sim 15\%$ reduced carbon sink for woody savanna (Fig. 13, lower left). In the Med simulation, savanna and woody savanna show similar tendencies; R_h increases relative to the LPJ-GUESS run, but not enough to overtake the increase in NPP. As a result, the average net carbon sink is enhanced by $\sim 17\%$ at savanna sites and by $\sim 9\%$ at woody savanna sites. Observed NEE is generally more negative than the values predicted by the simulations, with the exception of AU-RDF, where observations indicate a large net carbon source.

The three simulations slightly underestimate LAI at most evergreen broadleaf forest sites, but the non-LSM version produces values that are somewhat closer to the observations. Both GPP and R_a are somewhat lower in the LSM simulations, but similar to the LPJ-GUESS run. The net result is somewhat lower NPP estimates at these sites; a $\sim 14\%$ decrease, relative to LPJ-GUESS, in the BB simulation and a $\sim 10\%$ decrease in the Med simulation (Fig. 13, upper panels). R_h is also reduced in LSM simulations, but the balance with NPP still yields an NEE value above LPJ-GUESS's diagnostic (increases of $\sim 15\%$ and $\sim 20\%$ in the BB and the Med simulations, respectively; Fig. 13, lower panels). Observed NEE shows great cross-site variability. Simulations overestimate the strength of the CO_2 sink at the two Brazil sites and the Guiana sites, and greatly underestimate it at Robson Creek and Pasoh Forest.

560 The two deciduous broadleaf forest sites show different patterns. At PA-SPn, GPP is somewhat lower in the LSM simulations than in LPJ-GUESS, while autotrophic respiration is similar for all three simulations, which results in slightly decreased NPP values in the LSM runs. However, standard LPJ-GUESS predicts substantially higher heterotrophic respiration, so NEE is decreased in the LSM runs, but still much higher than the observed value of $\sim -458 \text{ gCm}^{-2}\text{y}^{-1}$. At the ZM-Mon site, GPP,



R_a and NPP increase in the LSM runs. Heterotrophic respiration is also enhanced in the LSM simulations, but the balance with
565 NPP still results in more negative NEE than standard LPJ-GUESS. The simulations predict a carbon sink between -107 and
 $-171 \text{ gCm}^{-2}\text{y}^{-1}$, while observations indicate a carbon source of $\sim 143 \text{ gCm}^{-2}\text{y}^{-1}$.

Figure 14 shows a comparison between land-cover averages of measured and modeled NEE for C_4 grasslands, savanna,
woody savanna and evergreen forests. Average measured NEE is negative for all land cover types, and substantially more
negative than in the simulations for savanna, woody savanna and evergreen broadleaf forests, implying an average underes-
570 timation of the C sink by the models at these sites. At C_4 sites simulations predict NEE values between $-86 \text{ gCm}^{-2}\text{y}^{-1}$
and $-125 \text{ gCm}^{-2}\text{y}^{-1}$, while observations indicate a less negative value of $-33 \text{ gCm}^{-2}\text{y}^{-1}$. For savanna, measured NEE is
 $\sim -221 \text{ gCm}^{-2}\text{y}^{-1}$, while simulations predict an average between $\sim -114 \text{ gCm}^{-2}\text{y}^{-1}$ and $\sim -133 \text{ gCm}^{-2}\text{y}^{-1}$. For woody
savanna, measured NEE averages to $\sim -238 \text{ gCm}^{-2}\text{y}^{-1}$, while simulated fluxes are $\sim -100 \text{ gCm}^{-2}\text{y}^{-1}$. Measured fluxes at
575 evergreen broadleaf forests are, on average, $\sim -396 \text{ gCm}^{-2}\text{y}^{-1}$, while simulations predict average fluxes between -144 and
 $-180 \text{ gCm}^{-2}\text{y}^{-1}$. However, this is the result of very large negative values measured at AU-Rob, and MY-PSO (Table 8). In
general, differences in simulated fluxes between standard LPJ-GUESS and the two LPJ-GUESS/LSM simulations seem to be
small compared to the magnitude of observed fluxes, and the interannual and cross-site variability of the measured fluxes is
much greater than in the simulations.

4 Discussion and summary

580 In this work we described a number of modifications to the LPJ-GUESS DGVM aimed at making the model suitable for direct
coupling with an atmospheric model. The newly incorporated energy balance module resolves the diurnal cycle of energy
and water fluxes between the canopy and the atmosphere, as opposed to LPJ-GUESS's daily calculations. This enables the
shorter time step used by atmospheric models to be matched. The simple, Beer's law-based PAR absorption calculations were
replaced with a more sophisticated two-stream radiative transfer scheme (Sellers, 1985; Dai et al., 2004), which allows for
585 separate treatment of sunlit and shaded leaves in the canopy. The representation of soil physical processes was modified in two
ways. Firstly, the original 1.5 m deep, two-layer soil column was replaced with a 3 m deep, 9-layer column. Secondly, the soil
heat and water transport schemes were replaced with less parametrized formulations. Soil heat transport is now calculated by
solving the heat diffusion equation, while soil water transport is solved by applying Richard's equation. These formulations are
better fit to resolve near-surface heat and water fluxes on the sub-daily time scales introduced in the model.

590 4.1 Evaluation of the simulated heat fluxes

The new model was evaluated by comparing simulated fluxes of sensible and latent heat with flux tower measurements at 21
FLUXNET sites. Stöckli et al. (2008) used a similar analysis (including the filtering of fluxes with $u^* < 0.2 \text{ m s}^{-1}$) to evaluate
the improvement in performance of CLM 3.5 after introducing nitrogen limitation of photosynthesis, a ground water model and
an updated formulation of surface resistance. Owing to the different site selection, a rigorous comparison of that study with the
595 results presented in section 3.4.2 is not possible, but average statistics of model performance can provide an overview of how



Table 9. Average correlation and RMSE between observed and simulated sensible and latent heat fluxes for LPJ-GUESS/LSM, CLM 3.0, and CLM 3.5. RMSE values (between brackets) are given in Wm^{-2} . Hourly and monthly values are labeled (h) and (m) respectively. CLM values correspond to averages over temperate, tropical and grassland sites as reported in Stöckli et al. (2008). LPJ-GUESS/LSM values correspond to the CLM/Med simulation.

	LPJ-GUESS/LSM	CLM 3.0	CLM 3.5
H (h)	0.90 (75)	0.70 (101)	0.77 (72)
H (m)	0.74 (26)	0.66 (47)	0.61 (30)
λE (h)	0.79 (76)	0.54 (83)	0.80 (59)
λE (m)	0.70 (24)	0.53 (40)	0.85 (29)

the models compare. Table 9 shows averaged values of the correlation coefficient and RMSE for CLM 3.0, CLM 3.5 and LPJ-GUESS/LSM. Our model seems to yield stronger correlations between measured and observed sensible heat fluxes, for similar RMSE values, while CLM 3.5 appears to perform better in terms of RMSE for hourly latent heat fluxes, and the correlation between measured and observed monthly latent heat fluxes is stronger. In order to ascertain the significance of these findings a comparison using the same site-measured fluxes and forcing climate would be needed. Nevertheless, the values presented in Table 9 suggest that the performance of our model is closer to CLM 3.5 than to CLM 3.0.

Sensible heat is generally overestimated by the LSM model. Poor performance in sensible heat flux estimation is a common issue of many land surface models (Best et al., 2015). The reason for this is not well understood. It has been suggested that the models, the majority of which use similar methods to calculate the turbulent fluxes, do not extract all the information available in the climate forcing data. However, eddy covariance measurements often fail to close the energy balance, and might systematically underestimate sensible heat much more than latent heat, which would appear as an overestimation of sensible heat in the simulations. A detailed discussion of these issues is provided in Haughton et al. (2016).

One issue in our simulations is the marked underestimation of latent heat flux during extremely dry periods, when the rooting zone is nearly depleted of water available for plant uptake. This, in turn, causes a strong spike in sensible heat (Fig. 7, upper right panel). All eight model configurations show this behaviour. One possible reason for this is the choice of free drainage boundary conditions at the bottom of the soil column. Simulating ground water in the model may promote the retention of some soil moisture during dry periods and thus help alleviate this problem (Stöckli et al., 2008). Deeper root profiles and lateral access to soil water may also be important to support evapotranspiration in dry periods (Schenk and Jackson, 2002).

We implemented two different stomatal conductance schemes: the Ball-Berry model (Ball et al., 1987) and the Medlyn model (Medlyn et al., 2011). One notable difference between these two models concerns the behaviour of the stomatal conductance when the vapour pressure deficit at the leaf surface (VPD) is small. In the Ball-Berry model, stomatal conductance increases linearly with decreasing VPD, while in the Medlyn model stomatal conductance increases much more rapidly as VPD approaches zero (Fig. 3). Larger stomatal conductance leads to generally higher evapotranspiration values (less negative bias values, Table 5), and enhanced GPP (Fig. 13) in simulations using the Medlyn model. A statistical evaluation of the impact of



Table 10. Daily average climate measured at the four C_4 grassland sites in this study. $T_{\text{atm,day}}$: daily average temperature ($^{\circ}\text{C}$); P_{day} : daily average precipitation (mm/day); $I_{0,\text{day}}^{\downarrow}$: daily average incoming solar irradiance (W m^{-2}).

	$T_{\text{atm,day}}$	P_{day}	$I_{0,\text{day}}^{\downarrow}$
AU-DaP	25.5	3.8	249.5
AU-Stp	26.2	2.0	262.0
CG-Tch	24.3	4.7	148.7
Pa-SPs	25.3	6.4	177.1

Table 11. Observed and simulated LAI at the four C_4 grassland sites when all natural PFTs are allowed to grow in the patch. The BB and Med values correspond to LSM simulations using the CLM-type water uptake function.

Site	Observed	Total			Tree			Grass		
		LPJ-G	BB	Med	LPJ-G	BB	Med	LPJ-G	BB	Med
AU-DaP	1.5	3.5	3.6	4.0	1.0	2.1	1.5	2.5	1.6	2.4
AU-Stp	0.5	2.6	1.0	0.9	0.3	0.8	0.6	2.3	0.3	0.3
CG-Tch	2.0	4.4	4.5	4.7	4.2	4.4	4.3	0.2	0.1	0.3
PA-SPs	5.4	5.2	4.4	4.4	4.9	3.8	3.9	0.3	0.6	0.6

620 these differences on the model output was not carried out, but the clumping of symbols representing the two different stomatal conductance models seen in Fig. 12 suggests that the stomatal conductance scheme has a significantly greater impact on the model's behaviour than the choice of soil water uptake function, except when the latter is very restrictive (for example, the Noah-type in our simulations, Eq. 49).

4.2 Why does C_4 productivity increase so much in LSM simulations?

625 The results presented in Section 3.4.4 show that predictions of PFT composition are similar for standard LPJ-GUESS and the LSM simulations. However, ecosystem productivity, respiration and carbon dioxide exchange vary between LSM simulations using different stomatal conductance schemes and with respect to standard LPJ-GUESS. Very notably, both the gross and net productivities of C_4 grasses are substantially enhanced in the LSM simulations. This results in unrealistically high simulated LAI values at three out of four sites where the grasses are allowed to grow without competition.

630 We found that the main reason for this behaviour is the occurrence of higher photosynthetic rates in the LSM simulations due to the mitigation of biochemical N limitation at higher leaf temperatures. Standard LPJ-GUESS uses a daily average of the forcing air temperature as a proxy for leaf temperature in the V_{max} calculation. By contrast, LPJ-GUESS/LSM simulates leaf temperature explicitly, and uses a daytime average (Eq. 44) to estimate V_{max} . This average leaf temperature can be several degrees above the forcing air temperature, which makes it possible to reach the optimal maximum carboxylation rate at lower



635 leaf nitrogen concentrations (see Haxeltine and Prentice, 1996). This makes it easier for the plants to attain the optimal V_{\max}
with the available nitrogen, which enhances productivity. Exceedingly high leaf temperatures can have a negative impact on
 V_{\max} due to the thermal breakdown of the biochemical reactions. However, the simulated leaf temperatures are still within the
optimal temperature range for C_4 grasses (20 to 45°C in LPJ-GUESS). The temperature dependence of V_{\max} , including the
effect on nitrogen limitation, is illustrated in Fig. 15.

640 At AU-Stp, all three simulations predict much lower productivities. In this case, water availability is the limiting factor. This
site receives, on average, considerably less rain water than the other three C_4 grasslands (Table 10), which leads to lower values
of the β factor (Eq. 48), and brings photosynthetic rates down.

As pointed out in Section 3.2, the simulated PFTs were restricted to grassy types at these sites. Table 11 shows a summary
of LAI values predicted by standard LPJ-GUESS and two representative LSM simulations when establishment is not restricted
645 to grassy PFTs. All three experiments predict a mixture of trees and grasses, but total LAI in the LSM runs is much lower
than in the simulations where only grasses were allowed to establish. In these runs, competition with trees limits the resources
available to grasses, and shading from the taller trees helps lowering the average leaf temperature of the grassy understory, all
of which helps counteract the effect described above.

4.3 Conclusion and outlook

650 The developments presented in this paper will enable to study feedbacks between the climate and the biosphere using the state-
of-the-art DGVM LPJ-GUESS coupled to an atmospheric model directly. Work is in progress regarding the development of a
flexible interface to enable such coupling, as well as extending the model's ability to simulate cold-climate ecosystems. More
work is also needed to characterize and fully understand the model's response to the switch from using air temperature as a
proxy for leaf temperature to simulating leaf temperature explicitly, particularly as these concern the productivity of C_4 plants
655 in well watered, no-competition situations (e.g., monoculture crops or managed pastures). These developments will allow to
use LPJ-GUESS/LSM in regional as well as global studies. Given the capacity of LPJ-GUESS to represent land use change
and management (Lindeskog et al., 2013, 2021; Olin et al., 2015), the range of applications includes exploring impacts of
management on regional climate, which can be an important tool to help devise and assess climate change mitigation policies.

Code and data availability. LPJ-GUESS is a worldwide developed and refined DGVM. The model code is managed and maintained by
660 the Department of Physical Geography and Ecosystem Science, Lund University, Sweden. The source code can be made available with a
collaboration agreement under the acceptance of certain conditions. For this reason, a DOI for the model code cannot be provided. The code
with the augmentations developed for this paper is available to the editor and reviewers via a restricted link, on the condition that the code is
used only for review purposes, and is deleted after the review process. Additional details and information can be found at the LPJ-GUESS
website (<http://web.nateko.lu.se/lpj-guess>, last access: 17 December 2021). The forcing data, evaluation data, model output and analysis
665 scripts used in this study have been uploaded to a public repository with DOI 10.5281/zenodo.5813886.



Appendix A: Derivation of the canopy conductance for water vapor flux

During a given time step Δt , the total amount of water evapotranspired from the sunlit part of the canopy can be expressed as the sum of the contributions from the dry and wet parts:

$$E_{\text{sun}} \Delta t = (1 - f_{\text{wet}}) E_{\text{sun, tr}} \Delta t + f_{\text{wet}} [E_{\text{sun, ev}} \Delta t_{\text{wet, sun}} + E_{\text{sun, tr}} (\Delta t - \Delta t_{\text{wet, sun}})] \quad (\text{A1})$$

where E_{sun} is the actual evapotranspiration rate, $E_{\text{sun, tr}}$ is the potential rate of transpiration, $E_{\text{sun, ev}}$ is the potential rate of evaporation, and $\Delta t_{\text{wet, sun}}$ is the time that the wet part of the sunlit canopy remains wet at the potential evaporation rate. The latter is calculated as:

$$\Delta t_{\text{wet, sun}} = \min \left(\frac{w_c \text{PAI}_{c, \text{sun}} / \text{PAI}_c}{f_{\text{wet}} E_{\text{sun, ev}}}, \Delta t \right), \quad (\text{A2})$$

675 where w_c is the current canopy water content (kg m^{-2}).

The evaporation rates in the above equations can be expressed as follows:

$$E_{\text{sun}} = -\rho g_{w, \text{sun}} [q_{ca} - q^*(T_{\text{sun}})]; \quad (\text{A3})$$

$$E_{\text{tr, sun}} = -\rho \sum_i \text{LAI}_{\text{sun}}^{(i)} \frac{g_{s, \text{sun}}^{(i)} g_b}{g_{s, \text{sun}}^{(i)} + g_b} [q_{ca} - q^*(T_{\text{sun}})]; \quad (\text{A4})$$

$$E_{\text{ev, sun}} = -\rho \text{PAI}_{c, \text{sun}} g_b [q_{ca} - q^*(T_{\text{sun}})]. \quad (\text{A5})$$

680 where the index i runs over cohorts. Inserting these expressions into Eq. (A1), dividing both sides by Δt , simplifying, and rearranging terms yields

$$g_{w, \text{sun}} = f_{\text{wet}} \eta_{\text{sun}} \text{PAI}_{c, \text{sun}} g_b + (1 - f_{\text{wet}} \eta_{\text{sun}}) \sum_i \text{LAI}_{\text{sun}}^{(i)} \frac{g_{s, \text{sun}}^{(i)} g_b}{g_{s, \text{sun}}^{(i)} + g_b}, \quad (\text{A6})$$

where $\eta_{\text{sun}} = \Delta t_{\text{wet, sun}} / \Delta t$. Identical equations apply to the shaded part of the canopy.

685 Appendix B: List of symbols, parameters and variables used in the model description

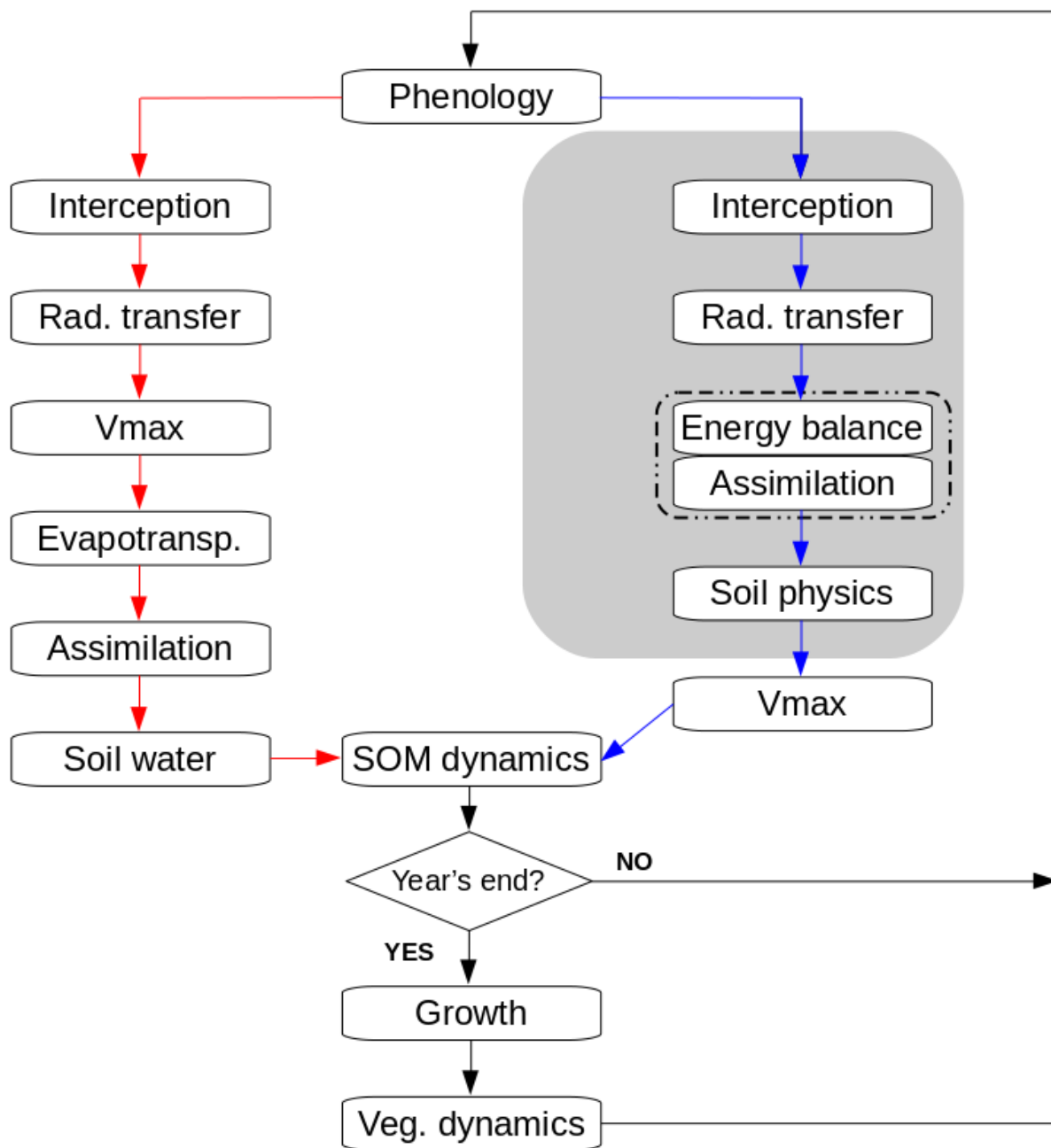


Figure 1. Flowchart of the main daily simulation loop in standard LPJ-GUESS (red branch) and the modified version (LPJ-GUESS/LSM, blue branch). The shaded area indicates the sub-daily loop in the modified version. The dashed line encloses coupled iterative calculations.

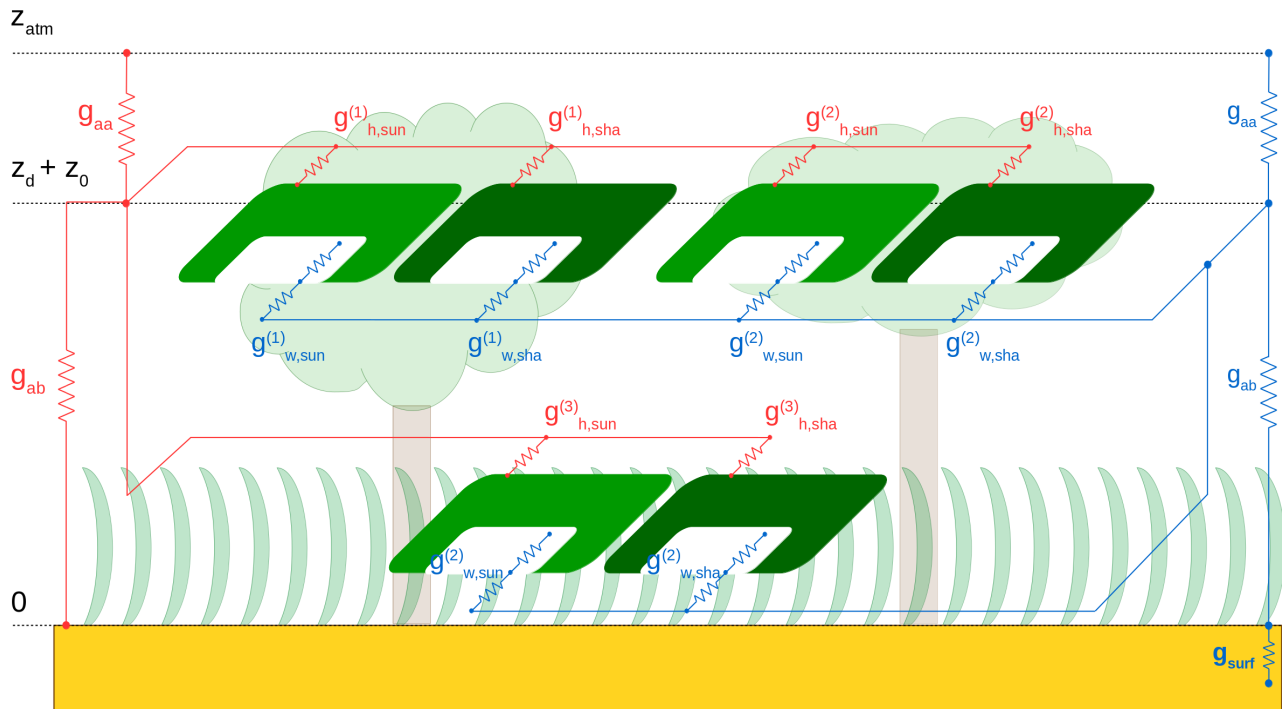


Figure 2. Networks of sensible (red) and latent (blue) heat exchange between the ground surface, the canopy and the atmosphere in the patch. Light green indicates the sunlit fraction of the cohorts, dark green the shaded fraction. g_{aa} is the aerodynamic conductance from the canopy air to the atmospheric reference level (z_{atm}). z_0 and z_d are respectively roughness length and zero plane displacement. g_{ab} is the aerodynamic conductance for heat/moisture flux from the ground surface to the canopy air. g_{surf} is the surface conductance for moisture flux. $g_{h,sun[sha]}^{(i)}$ is the conductance for sensible heat transport from the sunlit [shaded] part of cohort i to the canopy air. $g_{w,sun[sha]}^{(i)}$ is the conductance for moisture transport from the sunlit [shaded] part of cohort i to the canopy air, with the contributions from stomatal conductance and leaf boundary layer conductance represented explicitly. A dry canopy ($f_{wet} = 0$) is represented for clarity.

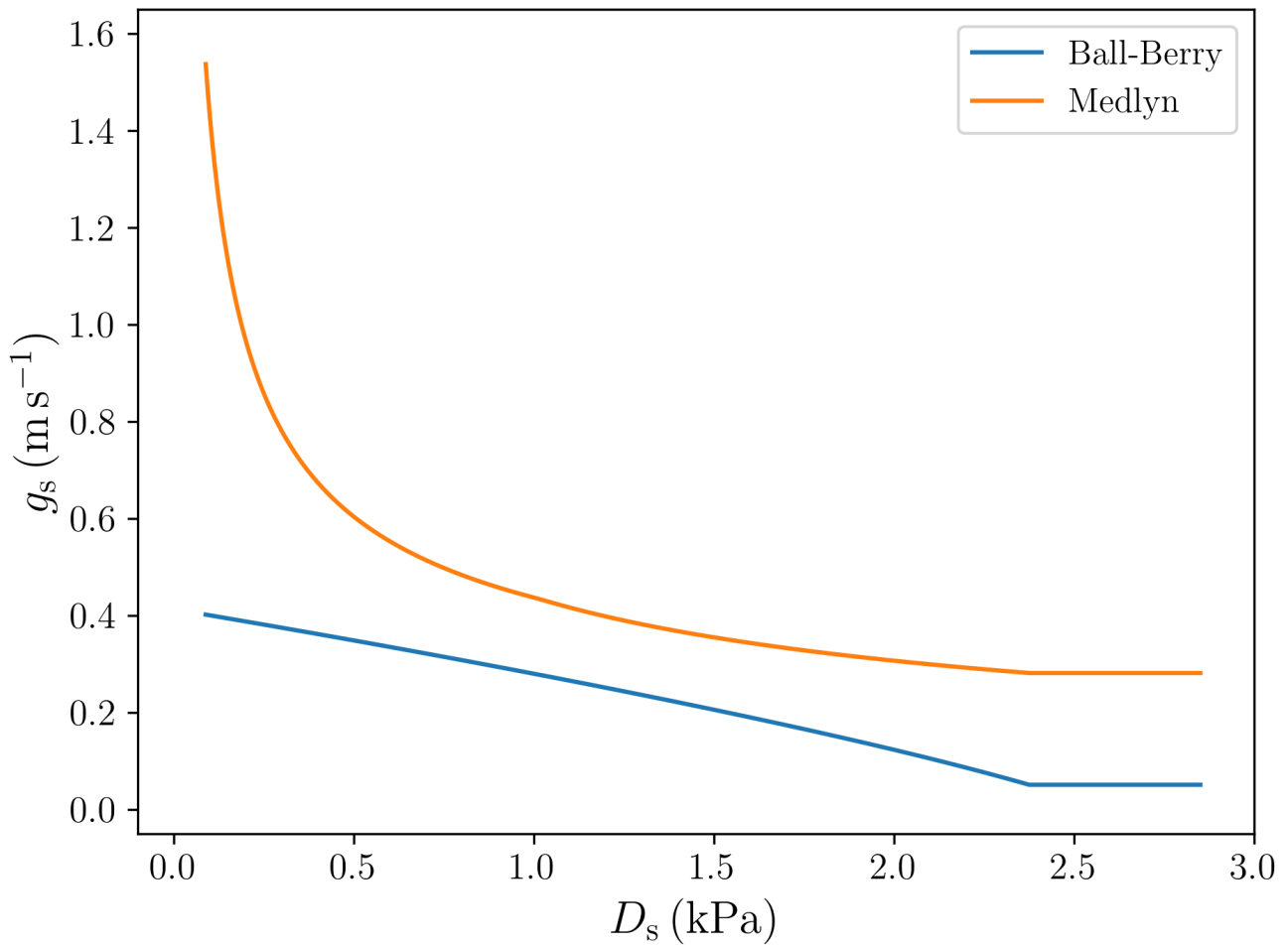


Figure 3. Stomatal conductance as a function of water vapor deficit at the leaf surface.

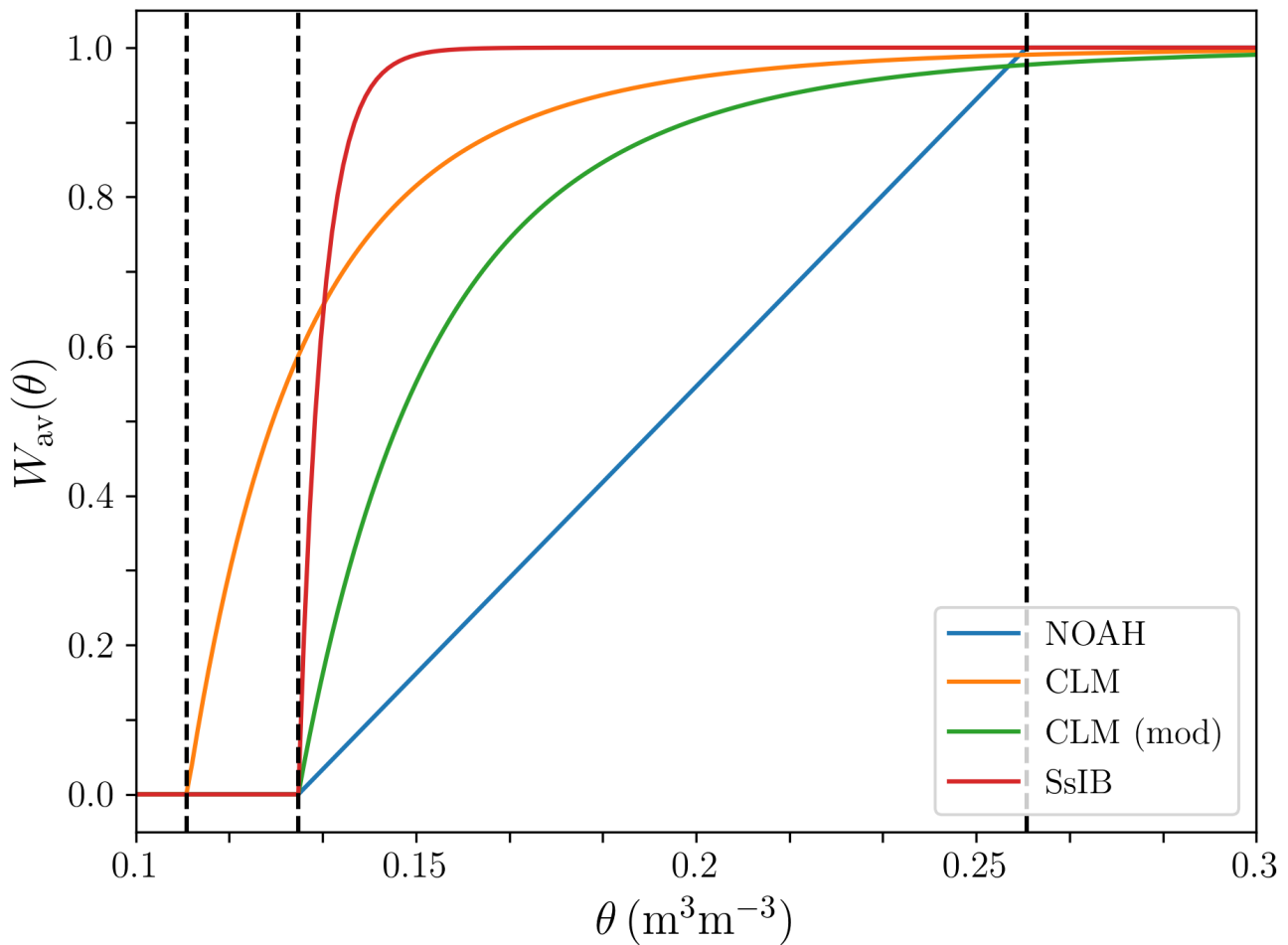


Figure 4. Factor limiting plant water uptake as a function of volumetric soil water content. The dashed, vertical lines represent, from left to right, the volumetric soil water content at a wilting matric potential of -150 m, at a wilting matric potential of -45 m, and at field capacity.

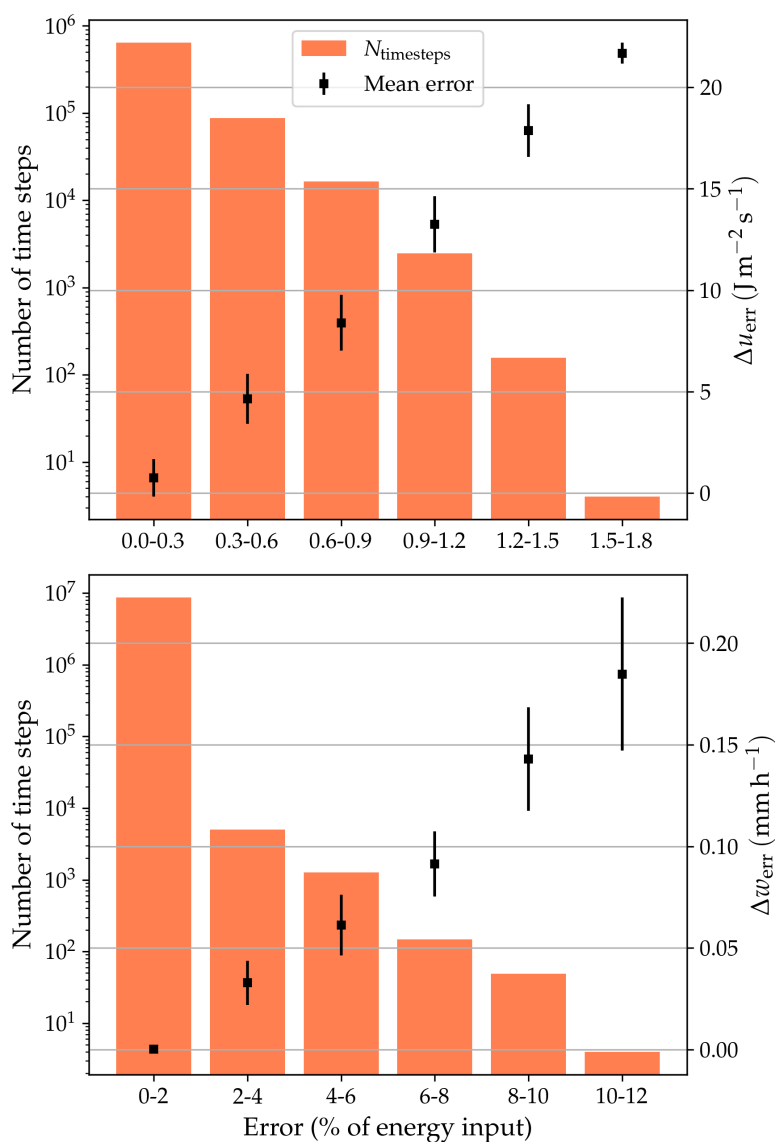


Figure 5. The histograms show the energy conservation error (upper panel) and the water conservation error (lower panel), as a percentage of the energy input, incurred at every time step. The symbols indicate the mean absolute error corresponding to each bin. The error bars indicate $\pm 1\sigma$ around the mean. The plots are derived from data from the historical period of all LSM simulations in this study.

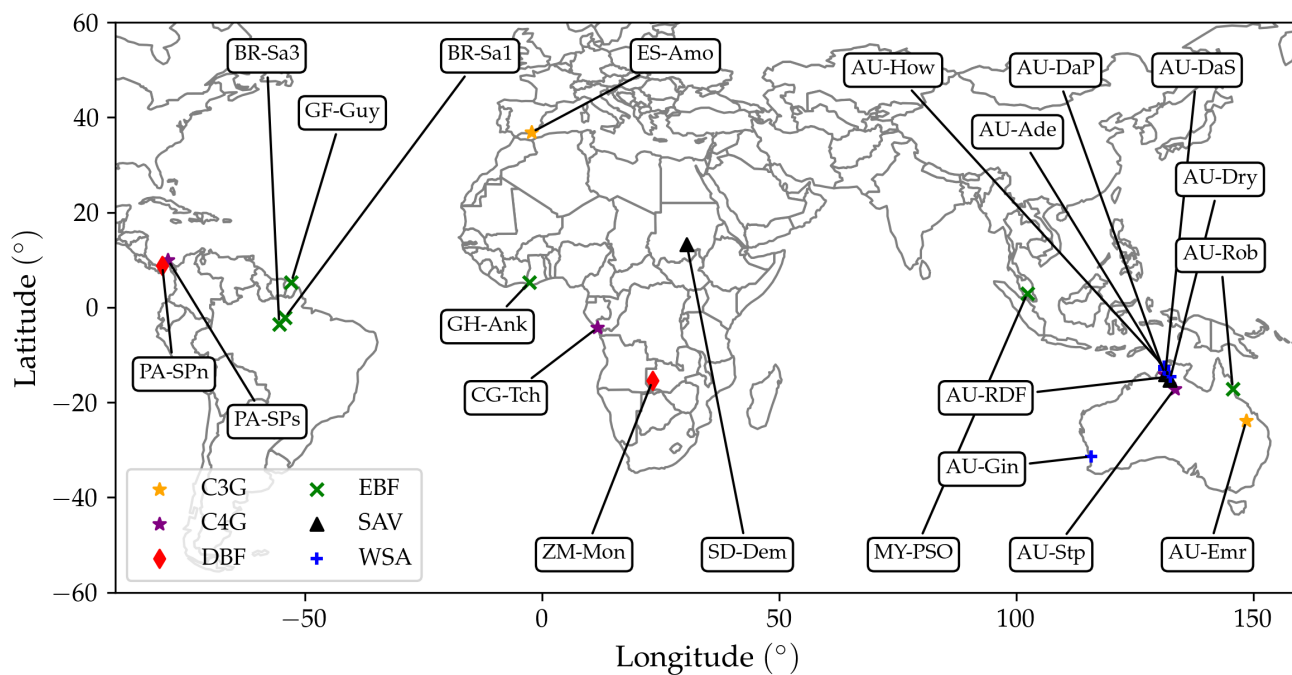


Figure 6. Fluxnet sites selected for model evaluation. Different symbols indicate different land cover types. The sites are labeled according to their site code (Table 1).

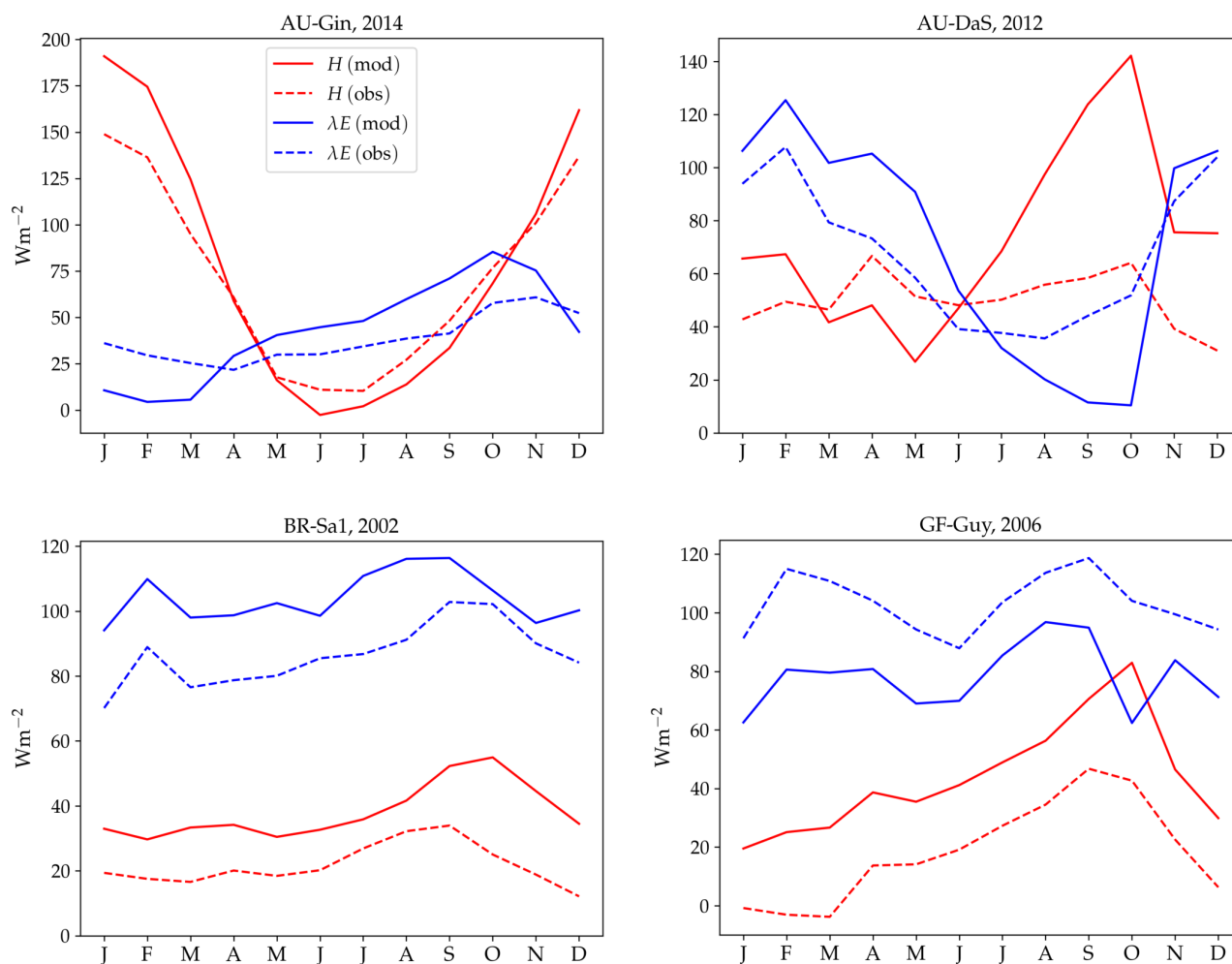


Figure 7. Observed (dashed lines) and simulated (continuous lines) annual cycles of sensible and latent heat flux at four selected sites: Gingin (AU-Gin, upper left), Daly River savanna (AU-DaS, upper right), Santarem Km. 67 (BR-Sa1, lower left), and Guyana (GF-Guy, lower right).

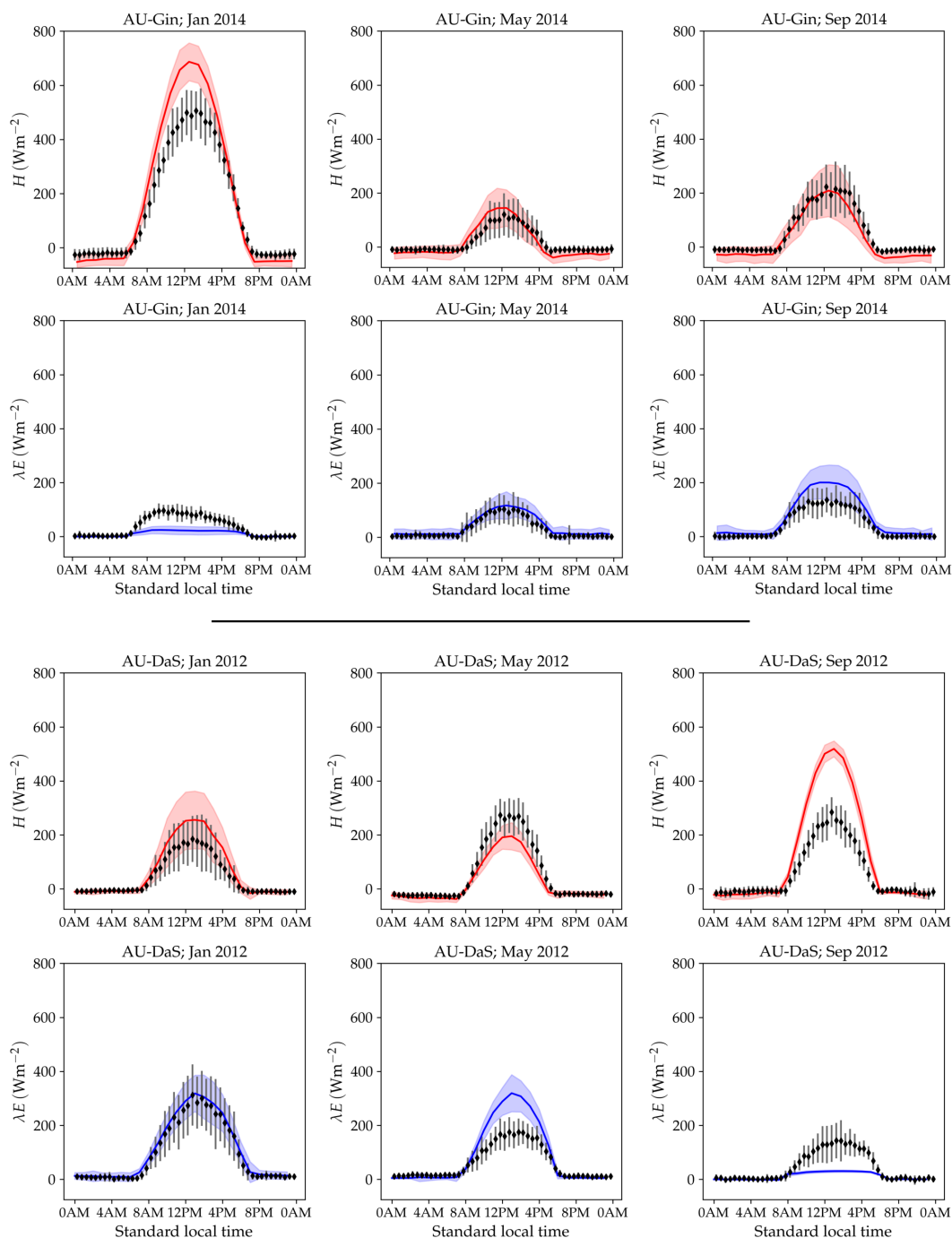


Figure 8. Monthly-averaged diurnal cycle of sensible and latent heat flux at the AU-DaP (upper panels) and AU-DaS sites (lower panels) in selected months. The red and blue lines represent simulated sensible and latent heat fluxes respectively. The shaded areas around each curve delimit one standard deviation above and below it. The symbols represent monthly averaged fluxes. The error bars indicate a $\pm 1\sigma$ deviation from the observed mean.

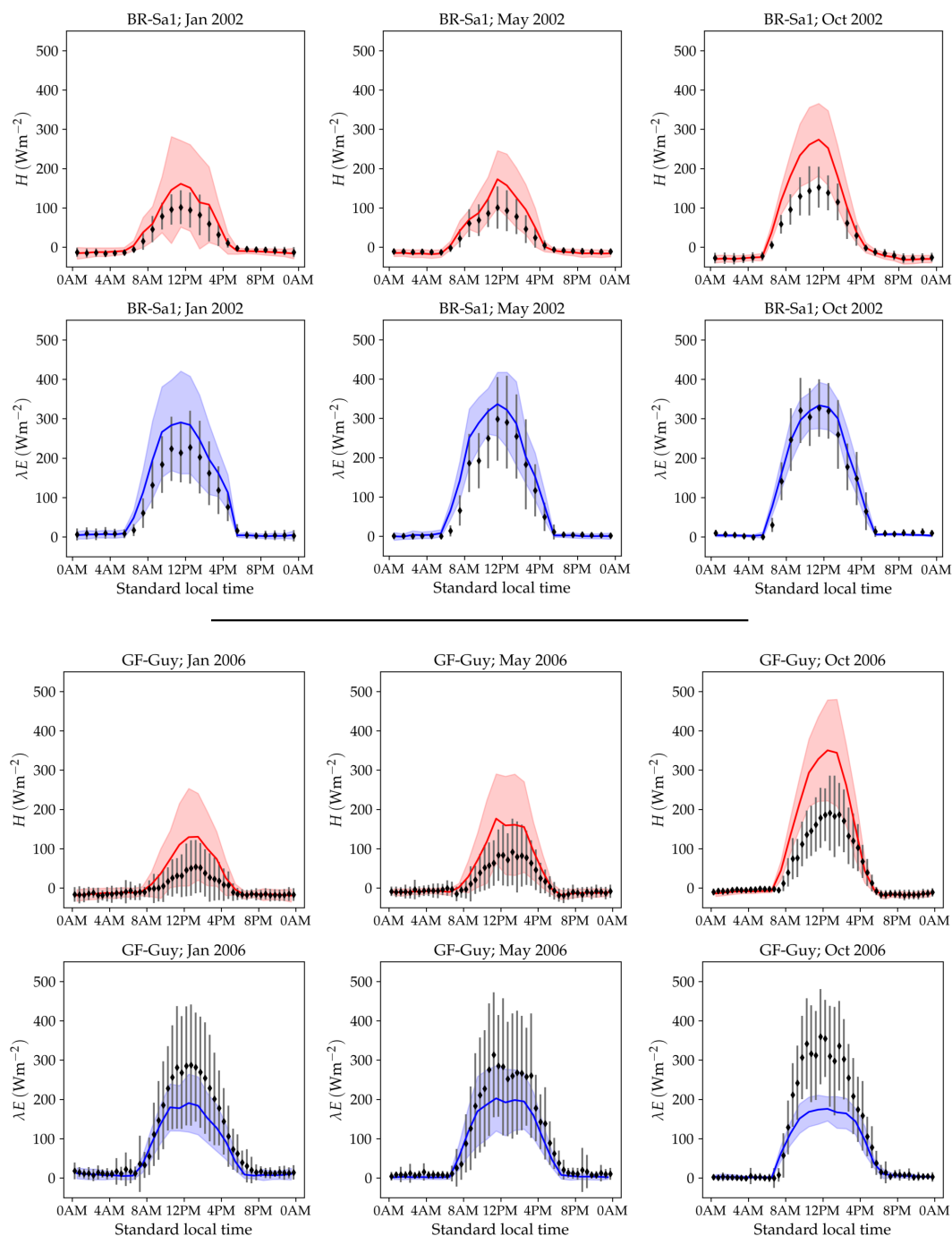


Figure 9. Monthly-averaged diurnal cycle of sensible and latent heat flux at the BR-Sa1 (upper panels) and GF-Guy sites (lower panels) in selected months. The red and blue lines represent simulated sensible and latent heat fluxes respectively. The shaded areas around each curve delimit one standard deviation above and below it. The symbols represent monthly averaged fluxes. The error bars indicate a $\pm 1\sigma$ deviation from the observed mean.

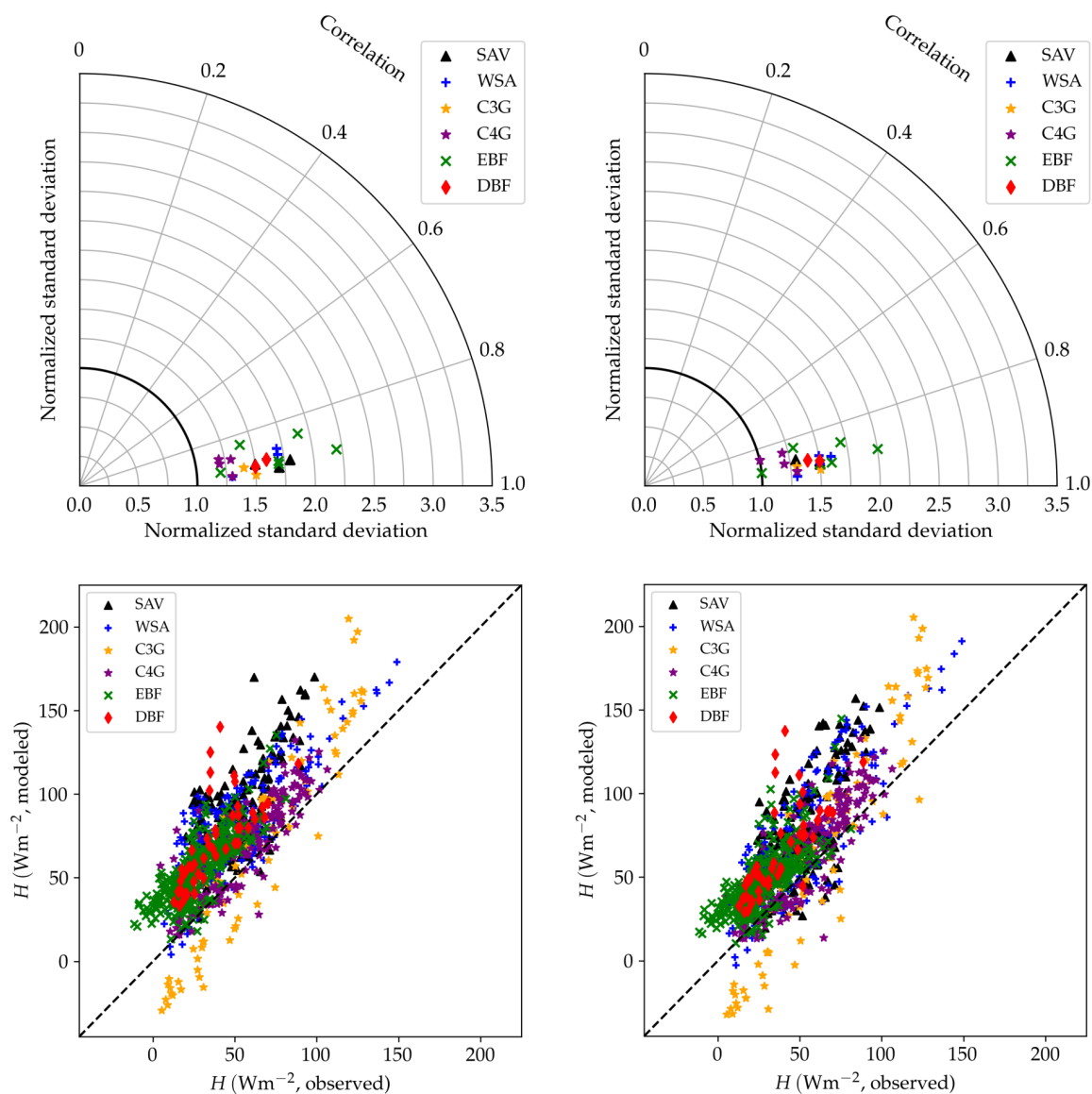


Figure 10. Performance of the CLM/BB (left) and the CLM/Med (right) runs for sensible heat flux. The Taylor diagrams (Taylor, 2001) on the upper panels summarize the degree of agreement between observed and simulated hourly fluxes by relying on the geometrical relationship between the “centered pattern” root mean square difference (defined as $E'^2 = \text{RMSE}^2 - \text{Bias}^2$), the correlation coefficient, and the standard deviation of observed and modeled data: $E'^2 = \sigma_o^2 + \sigma_m^2 - 2\sigma_o\sigma_m r$. Each point in the polar diagram represents a simulation. The radial coordinate indicates the ratio between modeled and observed standard deviations. The correlation between observed and modeled values is encoded by the polar angle; it decreases counterclockwise from $r = 1$ (perfect correlation) for points situated on the x - axis to $r = 0$ for points situated on the y - axis. The distance between a point in the diagram and the reference value 1 on the x - axis equals the centered pattern RMSE normalized by the standard deviation of the observed values, E'/σ_o , and is therefore a measure of the agreement between observed and simulated data. The scatter plots (lower panels) show a direct comparison of observed and modeled monthly averaged fluxes. The different symbols refer to different land cover types: savanna (SAV), woody savanna (WSA), C_3 grasslands (C3G), C_4 grasslands (C4G), evergreen broadleaf forest (EBF), and deciduous broadleaf forest (DBF).

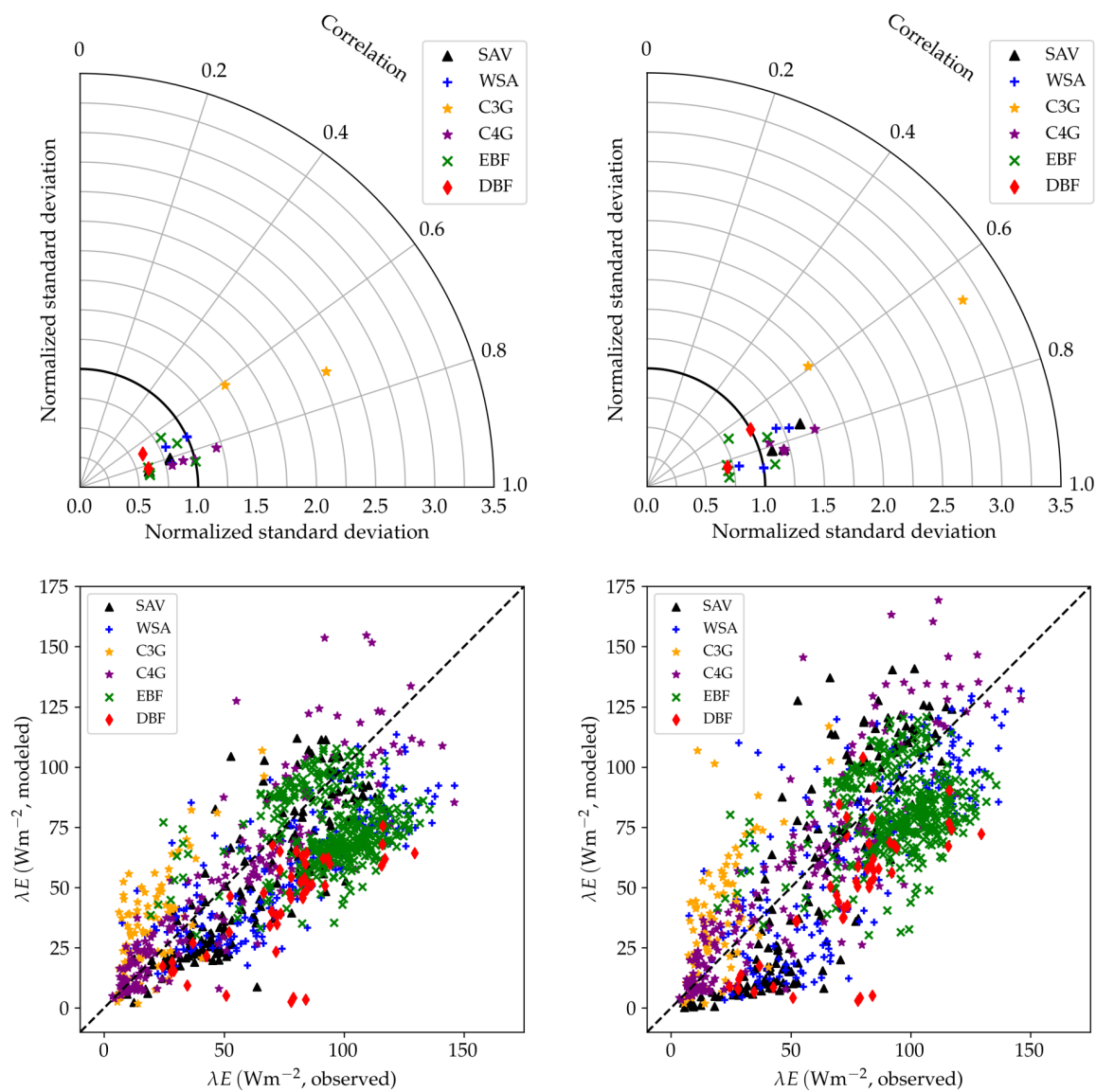


Figure 11. Performance of the CLM/BB (left) and the CLM/Med (right) runs for latent heat flux. The Taylor diagram shows statistical metrics calculated from hourly observed and simulated fluxes. The scatter plots show a direct comparison of observed and modeled monthly averaged fluxes. The different symbols refer to different land cover types: savanna (SAV), woody savanna (WSA), C_3 grasslands (C3G), C_4 grasslands (C4G), evergreen broadleaf forest (EBF), and deciduous broadleaf forest (DBF).

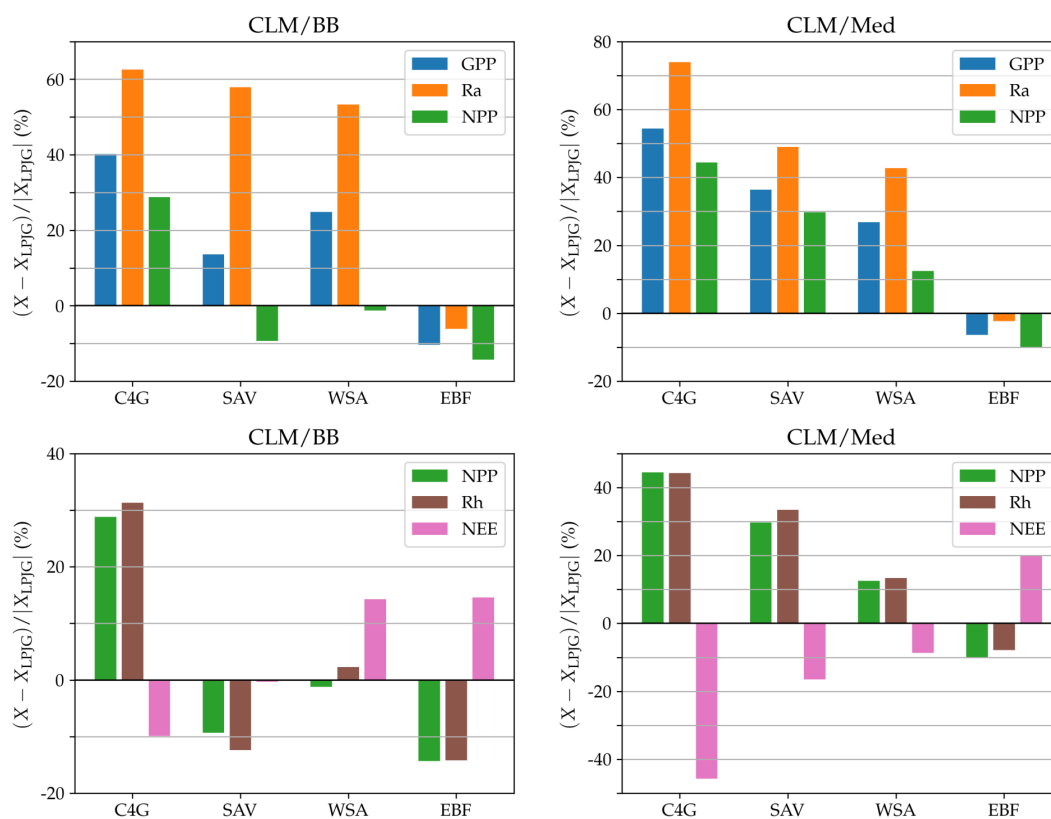


Figure 13. Top panels: percent change in average gross primary production (blue), autotrophic respiration (orange), and net primary production (green), simulated by the LSM version, with respect to standard LPJ-GUESS. Bottom panels: percent change in predicted average net primary production (green), heterotrophic respiration (brown) and net ecosystem exchange (pink).

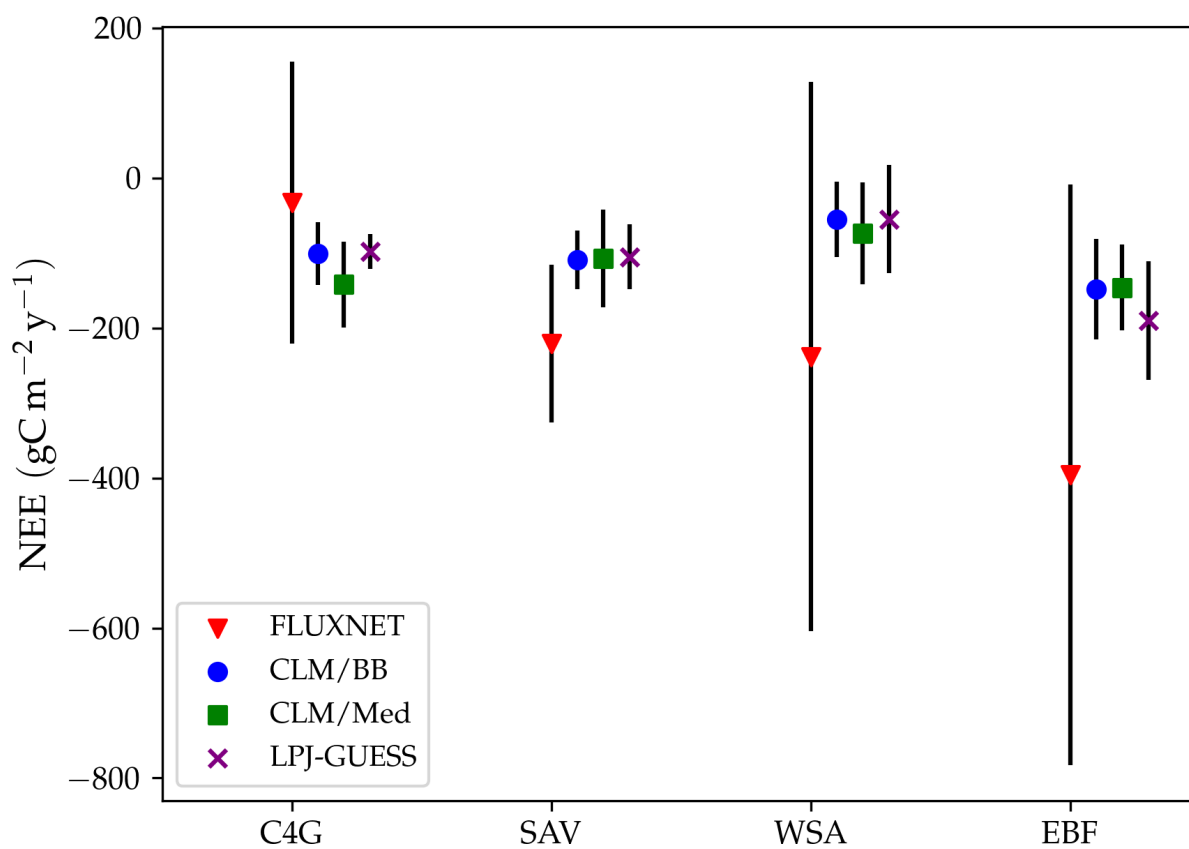


Figure 14. Comparison between observed and modeled annual NEE. The symbols indicate averages over sites the same land cover type. Red triangles correspond to flux tower CO₂ measurements. Blue dots, green squares and purple crosses correspond, respectively, to the CLM/BB, CLM/Med and standard LPJ-GUESS simulations. The bars represent one standard deviation above and below the average.

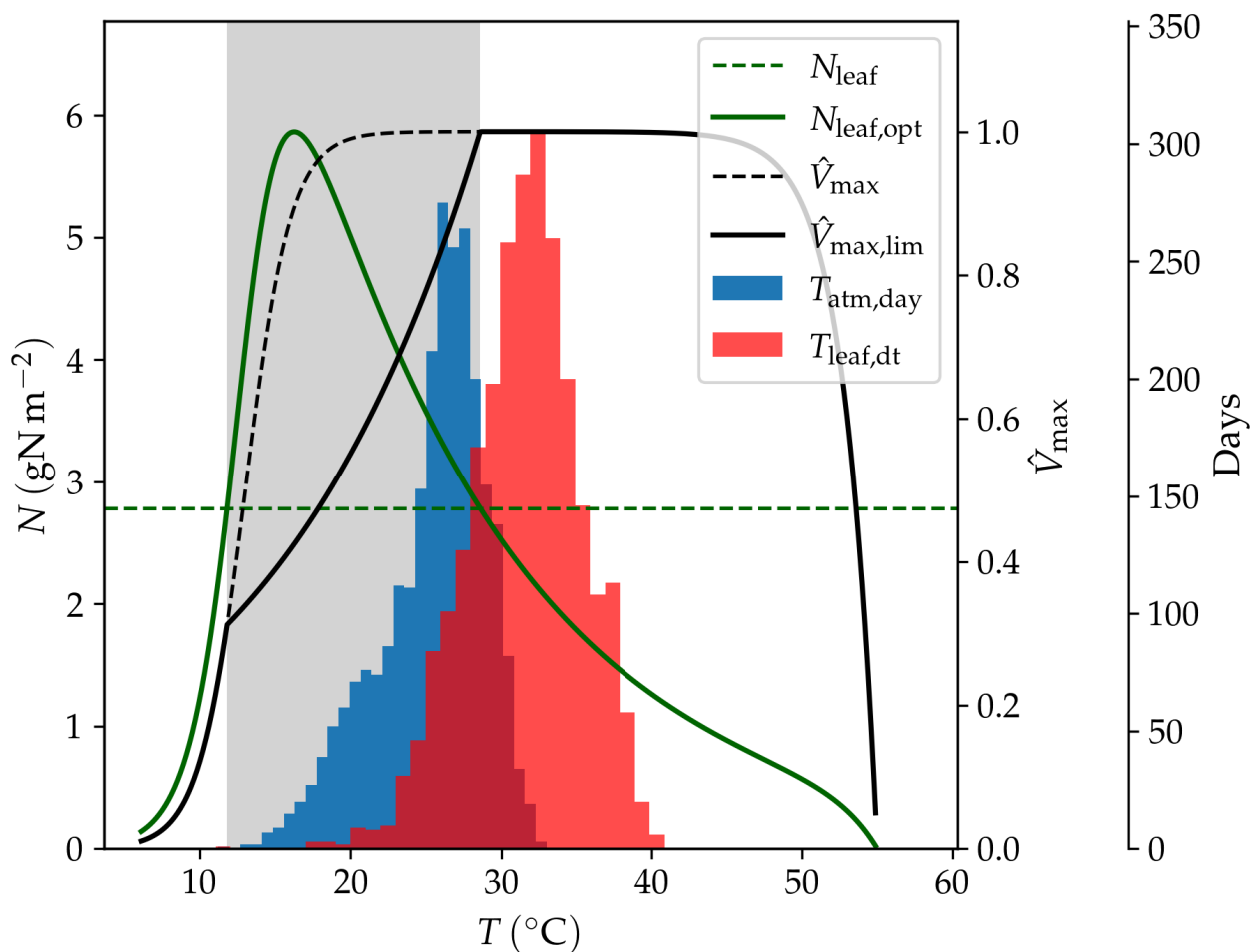


Figure 15. Effect of temperature (T) on modeled V_{\max} ; $N_{\text{leaf,opt}}$: leaf nitrogen content necessary to attain the maximum carboxylation rate; N_{leaf} : representative leaf nitrogen concentration; \hat{V}_{\max} : normalized maximum carboxylation rate without nitrogen limitation; $\hat{V}_{\max,\text{lim}}$: normalized maximum carboxylation rate with nitrogen limitation. The histograms show the frequency of temperatures in the AU-DaP simulation; $T_{\text{atm,day}}$: daily average of air temperature; $T_{\text{leaf,dt}}$: daytime average of leaf temperature. The shaded area indicates the temperature range where V_{\max} is nitrogen-limited.



Table A1. Ecosystem structure

Parameter	Description	Units
LAI_c	Patch canopy leaf area index	m^2/m^2
PAI_c	Patch canopy plant matter area index	m^2/m^2
$PAI^{(l)}$	Plant matter area index of patch canopy layer l	m^2/m^2
$LAI^{(i)}$	Leaf area index of cohort i in the patch	m^2/m^2
$SAI^{(i)}$	Stem area index of cohort i in the patch	m^2/m^2
$LAI^{(i,l)}$	Leaf area index of cohort i in patch canopy layer l	m^2/m^2
$SAI^{(i,l)}$	Stem area index of cohort i in patch canopy layer l	m^2/m^2
h_c	Patch canopy height	m



Table A2. Energy balance

Parameter	Description	Units
$S_{[\text{sun,sha}]}$	Shortwave radiation absorbed by the [sunlit, shaded] part of the canopy	Wm^{-2}
$L_{[\text{sun,sha}]}$	Net longwave radiation emitted by the [sunlit, shaded] part of the canopy	Wm^{-2}
$H_{[\text{sun,sha}]}$	Sensible heat flux from the [sunlit, shaded] canopy to the canopy air space	Wm^{-2}
$\lambda E_{[\text{sun,sha}]}$	Sensible heat flux from the [sunlit, shaded] canopy to the canopy air space	Wm^{-2}
S_g	Shortwave radiation absorbed by the ground surface	Wm^{-2}
L_g	Net longwave radiation emitted by the ground surface	Wm^{-2}
H_g	Sensible heat flux from the ground surface to the canopy air space	Wm^{-2}
λE_g	Latent heat flux from the ground surface to the canopy air space	Wm^{-2}
G	Heat flux conducted into the soil	Wm^{-2}
H^\uparrow	Sensible heat flux from the canopy air space to the atmosphere	Wm^{-2}
λE^\uparrow	Sensible heat flux from the canopy air space to the atmosphere	Wm^{-2}
$T_{[\text{sun,sha}]}$	Temperature of the [sunlit,shaded] part of the canopy	$^\circ\text{C}, \text{K}$
T_g	Temperature of the ground surface	$^\circ\text{C}, \text{K}$
T_{ca}	Temperature of the canopy air	$^\circ\text{C}$
T_{atm}	Temperature of the atmosphere at the reference level	$^\circ\text{C}$
$q_{[\text{sun,sha}]}$	Specific humidity of the stomatal cavity air for [sunlit,shaded] leaves	kg/kg
$q^*(T_g)$	Saturated specific humidity at the ground surface temperature	kg/kg
α	Ground surface specific humidity as a fraction of $q^*(T_g)$	-
q_{ca}	Specific humidity of the canopy air	kg/kg
q_{atm}	Specific humidity of the atmosphere at the reference level	kg/kg
g_b	Leaf boundary layer conductance	ms^{-1}
$g_{w,[\text{sun,sha}]}$	Conductance to water vapor between the [sunlit,shaded] canopy and the canopy air	ms^{-1}
g_{surf}	Conductance to water vapor from near-surface soil pores to the ground surface	ms^{-1}
g_{ab}	Aerodynamic conductance from the ground surface to the canopy air	ms^{-1}
g_{aa}	Aerodynamic conductance from the canopy air to the atmosphere reference level	ms^{-1}
f_{wet}	Wet fraction of the canopy	-
$\eta_{[\text{sun,sha}]}$	Factor limiting evaporation from the [sunlit,shaded] canopy	-
z_0	Canopy roughness length	m
z_d	Zero plane displacement height	m
$\Delta z^{(1)}$	Top soil layer thickness	m
$T_s^{(1)}$	Temperature of top soil layer	$^\circ\text{C}$
$\kappa_s^{(1)}$	Thermal conductivity of the top soil layer	$\text{Wm}^{-1}\text{K}^{-1}$



Table A3. Radiative transfer

Parameter	Description	Units
$PAI_{c,[sun,sha]}$	Plant matter area index of the [sunlit, shaded] part of the canopy	m^2/m^2
$PAI_{[sun,sha]}^{(i)}$	Plant matter area index of the [sunlit, shaded] part of cohort i	m^2/m^2
$LAI_{[sun,sha]}^{(i)}$	Leaf area index of the [sunlit, shaded] part of cohort i	m^2/m^2
$I_{[D,d]0}^\downarrow$	Incoming [direct beam, diffuse] radiation	Wm^{-2}
I_D^\downarrow	Direct beam profile in the canopy	Wm^{-2}
$\hat{f}_b^{[\downarrow,\uparrow]}$	Normalized profile of [downwards, upwards] scattered direct beam in the canopy	-
$\hat{f}_a^{[\downarrow,\uparrow]}$	Normalized profile of [downwards, upwards] scattered diffuse atmospheric radiation in the canopy	-
I^\uparrow	Outgoing shortwave radiation	Wm^{-2}
k	Direct beam extinction coefficient	-
ω	Direct beam scattering coefficient	-
$S_{[D,d]}^{(l)}$	[Direct, diffuse] shortwave radiation absorbed by canopy layer l	Wm^{-2}
$S_{[sun,sha]}^{(l)}$	Shortwave radiation absorbed by the [sunlit, shaded] part of canopy layer l	Wm^{-2}
$f_{[sun,sha]}^{(l)}$	Fraction of canopy layer l that is [sunlit, shaded]	Wm^{-2}
$S_{[sun,sha],vis}^{(l)}$	Visible radiation absorbed by the [sunlit,shaded] part of canopy layer l	Wm^{-2}
$PAR_{[sun,sha]}^{(i)}$	Photosynthetically active radiation absorbed by the [sunlit, shaded] part of cohort i	Wm^{-2}
$\alpha_{[sun,sha],[vis,nir]}$	Reflectivity of [sunlit, shaded] leaves in the [visible, infrared] waveband	-
$\tau_{[sun,sha],[vis,nir]}$	Transmissivity of [sunlit, shaded] leaves in the [visible, infrared] waveband	-
L^\downarrow	Incoming (atmospheric) longwave radiation	Wm^2
L^\uparrow	Outgoing longwave radiation	Wm^2
$\gamma_{[sun,sha]}$	Effective thermal emissivity of the [sunlit, shaded] part of the canopy	-



Table A4. Assimilation and stomatal conductance

Parameter	Description	Units
$g_{s,[sun,sha]}^{(i)}$	Stomatal conductance of the [sunlit,shaded] leaves of cohort i	ms^{-1}
g_{min}	Minimum stomatal conductance	ms^{-1}
$g_{1,\text{BB}}$	Stomatal conductance parameter for the Ball-Berry model	-
$g_{1,\text{Med}}$	Stomatal conductance parameter for the Medlyn model	$\text{kPa}^{0.5}$
$A_{n,[sun,sha]}^{(i)}$	Net photosynthetic assimilation rate of [sunlit,shaded] leaves of cohort i	$\mu\text{molCm}^{-2}\text{s}^{-1}$
$h_{s,[sun,sha]}$	Fractional humidity at the surface of [sunlit, shaded] leaves	kPa kPa^{-1}
$D_{s,[sun,sha]}$	Water vapor deficit at the surface of [sunlit, shaded] leaves	kPa
$c_{s,[sun,sha]}$	Carbon dioxide concentration at the surface of [sunlit, shaded] leaves	$\mu\text{mol mol}^{-1}$
$\text{PAR}_{\text{day}}^{(i)}$	Daily photosynthetically active radiation absorbed by cohort i	$\text{Jday}^{-1}\text{m}^{-2}$
$\text{PAR}_{[\text{sun,sha}],\text{day}}^{(i)}$	Daily photosynthetically active radiation absorbed by the [sunlit, shaded] parts of cohort i	$\text{Jday}^{-1}\text{m}^{-2}$
$V_{\text{max,day}}^{(i)}$	Maximum carboxylation rate of cohort i	$\mu\text{molCm}^{-2}\text{day}^{-1}$
f_v	Slope of the relationship between $\text{PAR}^{(i)}$ and $V_{\text{max}}^{(i)}$	μmolCJ^{-1}
$T_{\text{leaf,dt}}^{(i)}$	Daytime average temperature of cohort i	$^{\circ}\text{C}$
n_{dt}	Number of subdaily periods at the end of the simulation day	-
$V_{\text{max,[sun,sha],day}}^{(i)}$	Maximum carboxylation rate of the [sunlit, shaded] part of cohort i , per unit patch area	$\mu\text{molCm}^{-2}\text{day}^{-1}$
$V_{\text{max,[sun,sha],leaf}}^{(i)}$	Maximum carboxylation rate of the [sunlit, shaded] part of cohort i , per unit leaf area	$\mu\text{molCm}^{-2}\text{s}^{-1}$
$\text{LAI}_{[\text{sun,sha}],\text{dt}}^{(i)}$	Daytime average of the [sunlit,shaded] LAI for cohort i .	m^2m^{-2}
β	Water stress factor limiting the assimilation rate	-
$r^{(j)}$	Fraction of roots in soil layer j	-
$W_{\text{av}}^{(j)}$	Soil water uptake function (layer j)	-



Table A5. Soil physics

Parameter	Description	Units
T_s	Soil temperature	$^{\circ}\text{C}$
c_h	Volumetric heat capacity	$\text{Jm}^{-3}\text{C}^{-1}$
κ_s	Thermal conductivity	$\text{Wm}^{-1}\text{C}^{-1}$
$\theta^{(l)}$	Volumetric water content of soil layer l	m^3m^{-3}
θ_{wilt}	Volumetric soil water content at wilting point	m^3m^{-3}
θ_{fc}	Volumetric soil water content at field capacity	m^3m^{-3}
$\psi^{(l)}$	Matric potential of soil layer l	m
ψ_{wilt}	Matric potential of soil water at wilting point	m
ψ_{fc}	Matric potential of soil water at saturation point	m
γ_w	Hydraulic conductivity	ms^{-1}
λ_w	Hydraulic diffusivity	m^2s^{-1}
S_{θ}	Volumetric soil water uptake sink term	m^3m^{-3}



Author contributions. AA had the original idea and motivated the development. DMB designed the model augmentations described in this work with input from all the coauthors. DMB implemented the code, ran the experiments and performed the model evaluation analysis. All coauthors provided input regarding the analysis of the results and the discussion, and helped shape the final form of the manuscript.

Competing interests. The author declare no competing interests.



690 References

- Ahlström, A., Smith, B., Lindström, J., Rummukainen, M., and Uvo, C. B.: GCM characteristics explain the majority of uncertainty in projected 21st century terrestrial ecosystem carbon balance, *Biogeosciences*, 10, 1517–1528, <https://doi.org/10.5194/bg-10-1517-2013>, publisher: Copernicus GmbH, 2013.
- Ahlström, A., Schurgers, G., and Smith, B.: The large influence of climate model bias on terrestrial carbon cycle simulations, *Environmental Research Letters*, 12, 014004, <https://doi.org/10.1088/1748-9326/12/1/014004>, publisher: IOP Publishing, 2017.
- Alessandri, A., Catalano, F., De Felice, M., Van Den Hurk, B., Doblas Reyes, F., Boussetta, S., Balsamo, G., and Miller, P. A.: Multi-scale enhancement of climate prediction over land by increasing the model sensitivity to vegetation variability in EC-Earth, *Climate Dynamics*, 49, 1215–1237, <https://doi.org/10.1007/s00382-016-3372-4>, 2017.
- Ardö, J., Mölder, M., El-Tahir, B. A., and Elkhidir, H. A. M.: Seasonal variation of carbon fluxes in a sparse savanna in semi arid Sudan, *Carbon Balance and Management*, 3, 7, <https://doi.org/10.1186/1750-0680-3-7>, 2008.
- Arnth, A., Harrison, S. P., Zaehle, S., Tsigaridis, K., Menon, S., Bartlein, P. J., Feichter, J., Korhola, A., Kulmala, M., O'Donnell, D., Schurgers, G., Sorvari, S., and Vesala, T.: Terrestrial biogeochemical feedbacks in the climate system, *Nature Geoscience*, 3, 525–532, <https://doi.org/10.1038/ngeo905>, bandiera_abtest: a Cg_type: Nature Research Journals Number: 8 Primary_atype: Reviews Publisher: Nature Publishing Group Subject_term: Biogeochemistry;Climate sciences Subject_term_id: biogeochemistry;climate-sciences, 2010.
- 705 Arnth, A., Sitch, S., Pongratz, J., Stocker, B. D., Ciais, P., Poulter, B., Bayer, A. D., Bondeau, A., Calle, L., Chini, L. P., Gasser, T., Fader, M., Friedlingstein, P., Kato, E., Li, W., Lindeskog, M., Nabel, J. E. M. S., Pugh, T. a. M., Robertson, E., Viovy, N., Yue, C., and Zaehle, S.: Historical carbon dioxide emissions caused by land-use changes are possibly larger than assumed, *Nature Geoscience*, 10, 79–84, <https://doi.org/10.1038/ngeo2882>, number: 2 Publisher: Nature Publishing Group, 2017.
- Ball, J. T., Woodrow, I. E., and Berry, J. A.: A Model Predicting Stomatal Conductance and its Contribution to the Control of Photosynthesis under Different Environmental Conditions, in: *Progress in Photosynthesis Research: Volume 4 Proceedings of the VIIth International Congress on Photosynthesis Providence, Rhode Island, USA, August 10–15, 1986*, edited by Biggins, J., pp. 221–224, Springer Netherlands, Dordrecht, https://doi.org/10.1007/978-94-017-0519-6_48, 1987.
- Berlinger, J., Hacker, J., Hutley, L. B., Leuning, R., Arndt, S. K., Amiri, R., Bannehr, L., Cernusak, L. A., Grover, S., Hensley, C., Hocking, D., Isaac, P., Jamali, H., Kanniah, K., Livesley, S., Neining, B., U, K. T. P., Sea, W., Straten, D., Tapper, N., Weinmann, R., Wood, S., and Zegelin, S.: SPECIAL—Savanna Patterns of Energy and Carbon Integrated across the Landscape, *Bulletin of the American Meteorological Society*, 92, 1467–1485, <https://doi.org/10.1175/2011BAMS2948.1>, publisher: American Meteorological Society Section: Bulletin of the American Meteorological Society, 2011.
- 715 Berlinger, J., Hutley, L. B., McHugh, I., Arndt, S. K., Campbell, D., Cleugh, H. A., Cleverly, J., Resco de Dios, V., Eamus, D., Evans, B., Ewenz, C., Grace, P., Griebel, A., Haverd, V., Hinko-Najera, N., Huete, A., Isaac, P., Kanniah, K., Leuning, R., Liddell, M. J., Macfarlane, C., Meyer, W., Moore, C., Pendall, E., Phillips, A., Phillips, R. L., Prober, S. M., Restrepo-Coupe, N., Rutledge, S., Schroder, I., Silberstein, R., Southall, P., Yee, M. S., Tapper, N. J., van Gorsel, E., Vote, C., Walker, J., and Wardlaw, T.: An introduction to the Australian and New Zealand flux tower network – OzFlux, *Biogeosciences*, 13, 5895–5916, <https://doi.org/10.5194/bg-13-5895-2016>, publisher: Copernicus GmbH, 2016.
- 720 Best, M. J., Abramowitz, G., Johnson, H. R., Pitman, A. J., Balsamo, G., Boone, A., Cuntz, M., Decharme, B., Dirmeyer, P. A., Dong, J., Ek, M., Guo, Z., Haverd, V., Hurk, B. J. J. v. d., Nearing, G. S., Pak, B., Peters-Lidard, C., Santanello, J. A., Stevens, L., and



- Vuichard, N.: The Plumbing of Land Surface Models: Benchmarking Model Performance, *Journal of Hydrometeorology*, 16, 1425–1442, <https://doi.org/10.1175/JHM-D-14-0158.1>, publisher: American Meteorological Society Section: Journal of Hydrometeorology, 2015.
- Bonal, D., Bosc, A., Ponton, S., Goret, J.-Y., Burban, B., Gross, P., Bonnefond, J.-M., Elbers, J., Longdoz, B., Epron, D., Guehl, J.-M., and Granier, A.: Impact of severe dry season on net ecosystem exchange in the Neotropical rainforest of French Guiana, *Global Change Biology*, 14, 1917–1933, <https://doi.org/https://doi.org/10.1111/j.1365-2486.2008.01610.x>, [_eprint: https://onlinelibrary.wiley.com/doi/pdf/10.1111/j.1365-2486.2008.01610.x](https://onlinelibrary.wiley.com/doi/pdf/10.1111/j.1365-2486.2008.01610.x), 2008.
- Bonan, G. B.: *Ecological Climatology: Concepts and Applications*, <https://doi.org/10.1017/CBO9780511805530>, 2008.
- Bonan, G. B., Levis, S., Sitch, S., Vertenstein, M., and Oleson, K. W.: A dynamic global vegetation model for use with climate models: concepts and description of simulated vegetation dynamics, *Global Change Biology*, 9, 1543–1566, <https://doi.org/10.1046/j.1365-2486.2003.00681.x>, 2003.
- Booth, B. B. B., Jones, C. D., Collins, M., Totterdell, I. J., Cox, P. M., Sitch, S., Huntingford, C., Betts, R. A., Harris, G. R., and Lloyd, J.: High sensitivity of future global warming to land carbon cycle processes, *Environmental Research Letters*, 7, 024002, <https://doi.org/10.1088/1748-9326/7/2/024002>, publisher: IOP Publishing, 2012.
- Bristow, M., Hutley, L. B., Beringer, J., Livesley, S. J., Edwards, A. C., and Arndt, S. K.: Quantifying the relative importance of greenhouse gas emissions from current and future savanna land use change across northern Australia, *Biogeosciences*, 13, 6285–6303, <https://doi.org/10.5194/bg-13-6285-2016>, publisher: Copernicus GmbH, 2016.
- Brovkin, V., Sitch, S., Bloh, W. V., Claussen, M., Bauer, E., and Cramer, W.: Role of land cover changes for atmospheric CO₂ increase and climate change during the last 150 years, *Global Change Biology*, 10, 1253–1266, <https://doi.org/10.1111/j.1365-2486.2004.00812.x>, [_eprint: https://onlinelibrary.wiley.com/doi/pdf/10.1111/j.1365-2486.2004.00812.x](https://onlinelibrary.wiley.com/doi/pdf/10.1111/j.1365-2486.2004.00812.x), 2004.
- Christidis, N., Stott, P. A., Hegerl, G. C., and Betts, R. A.: The role of land use change in the recent warming of daily extreme temperatures, *Geophysical Research Letters*, 40, 589–594, <https://doi.org/10.1002/grl.50159>, [_eprint: https://agupubs.onlinelibrary.wiley.com/doi/pdf/10.1002/grl.50159](https://agupubs.onlinelibrary.wiley.com/doi/pdf/10.1002/grl.50159), 2013.
- Ciais, P., Sabine, C., Bala, G., Bopp, L., Brovkin, V., Al, E., and House, J. I.: Carbon and Other Biogeochemical Cycles, *Climate Change 2013: The Physical Science Basis. Contribution of Working Group I to the Fifth Assessment Report of the Intergovernmental Panel on Climate Change*, pp. 465–570, <https://research-information.bris.ac.uk/en/publications/carbon-and-other-biogeochemical-cycles>, publisher: Cambridge University Press, 2014.
- Clapp, R. B. and Hornberger, G. M.: Empirical equations for some soil hydraulic properties, *Water Resources Research*, 14, 601–604, <https://doi.org/https://doi.org/10.1029/WR014i004p00601>, [_eprint: https://agupubs.onlinelibrary.wiley.com/doi/pdf/10.1029/WR014i004p00601](https://agupubs.onlinelibrary.wiley.com/doi/pdf/10.1029/WR014i004p00601), 1978.
- Cosby, B. J., Hornberger, G. M., Clapp, R. B., and Ginn, T. R.: A Statistical Exploration of the Relationships of Soil Moisture Characteristics to the Physical Properties of Soils, *Water Resources Research*, 20, 682–690, <https://doi.org/https://doi.org/10.1029/WR020i006p00682>, [_eprint: https://agupubs.onlinelibrary.wiley.com/doi/pdf/10.1029/WR020i006p00682](https://agupubs.onlinelibrary.wiley.com/doi/pdf/10.1029/WR020i006p00682), 1984.
- Cramer, W., Bondeau, A., Woodward, F. I., Prentice, I. C., Betts, R. A., Brovkin, V., Cox, P. M., Fisher, V., Foley, J. A., Friend, A. D., Kucharik, C., Lomas, M. R., Ramankutty, N., Sitch, S., Smith, B., White, A., and Young-Molling, C.: Global response of terrestrial ecosystem structure and function to CO₂ and climate change: results from six dynamic global vegetation models, *Global Change Biology*, 7, 357–373, <https://doi.org/https://doi.org/10.1046/j.1365-2486.2001.00383.x>, [_eprint: https://onlinelibrary.wiley.com/doi/pdf/10.1046/j.1365-2486.2001.00383.x](https://onlinelibrary.wiley.com/doi/pdf/10.1046/j.1365-2486.2001.00383.x), 2001.



- Dai, Y., Dickinson, R. E., and Wang, Y.-P.: A Two-Big-Leaf Model for Canopy Temperature, Photosynthesis, and Stomatal Conductance, *Journal of Climate*, 17, 2281–2299, [https://doi.org/10.1175/1520-0442\(2004\)017<2281:ATMFCT>2.0.CO;2](https://doi.org/10.1175/1520-0442(2004)017<2281:ATMFCT>2.0.CO;2), 2004.
- 765 De Kauwe, M. G., Kala, J., Lin, Y.-S., Pitman, A. J., Medlyn, B. E., Duursma, R. A., Abramowitz, G., Wang, Y.-P., and Miralles, D. G.: A test of an optimal stomatal conductance scheme within the CABLE land surface model, *Geoscientific Model Development*, 8, 431–452, <https://doi.org/10.5194/gmd-8-431-2015>, publisher: Copernicus GmbH, 2015.
- de Vries, D.: Thermal properties of soils, *Physics of Plant Environment*, <https://ci.nii.ac.jp/naid/10016146353/>, publisher: North-Holland Publishing Co., 1963.
- 770 Dickinson, R. E.: Land Surface Processes and Climate—Surface Albedos and Energy Balance, in: *Advances in Geophysics*, edited by Saltzman, B., vol. 25 of *Theory of Climate*, pp. 305–353, Elsevier, [https://doi.org/10.1016/S0065-2687\(08\)60176-4](https://doi.org/10.1016/S0065-2687(08)60176-4), 1983.
- Döscher, R., Acosta, M., Alessandri, A., Anthoni, P., Arneth, A., Arsouze, T., Bergmann, T., Bernadello, R., Bousetta, S., Caron, L.-P., Carver, G., Castrillo, M., Catalano, F., Cvijanovic, I., Davini, P., Dekker, E., Doblus-Reyes, F. J., Docquier, D., Echevarria, P., Fladrich, U., Fuentes-Franco, R., Gröger, M., v. Hardenberg, J., Hieronymus, J., Karami, M. P., Keskinen, J.-P., Koenigk, T., Makkonen, R., Massonnet, 775 F., Ménégos, M., Miller, P. A., Moreno-Chamarro, E., Nieradzic, L., van Noije, T., Nolan, P., O'Donnell, D., Ollinaho, P., van den Oord, G., Ortega, P., Prims, O. T., Ramos, A., Reerink, T., Rousset, C., Ruprich-Robert, Y., Le Sager, P., Schmith, T., Schrödner, R., Serva, F., Sicardi, V., Sloth Madsen, M., Smith, B., Tian, T., Tourigny, E., Uotila, P., Vancoppenolle, M., Wang, S., Wårlind, D., Willén, U., Wyser, K., Yang, S., Yepes-Arbós, X., and Zhang, Q.: The EC-Earth3 Earth System Model for the Climate Model Intercomparison Project 6, *Geoscientific Model Development Discussions*, pp. 1–90, <https://doi.org/10.5194/gmd-2020-446>, publisher: Copernicus GmbH, 2021.
- 780 Fisher, R. A., Koven, C. D., Anderegg, W. R. L., Christoffersen, B. O., Dietze, M. C., Farrior, C. E., Holm, J. A., Hurtt, G. C., Knox, R. G., Lawrence, P. J., Lichstein, J. W., Longo, M., Matheny, A. M., Medvigy, D., Muller-Landau, H. C., Powell, T. L., Serbin, S. P., Sato, H., Shuman, J. K., Smith, B., Trugman, A. T., Viskari, T., Verbeeck, H., Weng, E., Xu, C., Xu, X., Zhang, T., and Moorcroft, P. R.: Vegetation demographics in Earth System Models: A review of progress and priorities, *Global Change Biology*, 24, 35–54, <https://doi.org/10.1111/gcb.13910>, eprint: <https://onlinelibrary.wiley.com/doi/pdf/10.1111/gcb.13910>, 2018.
- 785 Forrest, M., Tost, H., Lelieveld, J., and Hickler, T.: Including vegetation dynamics in an atmospheric chemistry-enabled general circulation model: linking LPJ-GUESS (v4.0) with the EMAC modelling system (v2.53), *Geoscientific Model Development*, 13, 1285–1309, <https://doi.org/https://doi.org/10.5194/gmd-13-1285-2020>, publisher: Copernicus GmbH, 2020.
- Friedlingstein, P., Cox, P., Betts, R., Bopp, L., von Bloh, W., Brovkin, V., Cadule, P., Doney, S., Eby, M., Fung, I., Bala, G., John, J., Jones, C., Joos, F., Kato, T., Kawamiya, M., Knorr, W., Lindsay, K., Matthews, H. D., Raddatz, T., Rayner, P., Reick, C., Roeckner, E., Schnitzler, 790 K.-G., Schnur, R., Strassmann, K., Weaver, A. J., Yoshikawa, C., and Zeng, N.: Climate–Carbon Cycle Feedback Analysis: Results from the C4MIP Model Intercomparison, *Journal of Climate*, 19, 3337–3353, <https://doi.org/10.1175/JCLI3800.1>, 2006.
- Friedlingstein, P., Meinshausen, M., Arora, V. K., Jones, C. D., Anav, A., Liddicoat, S. K., and Knutti, R.: Uncertainties in CMIP5 Climate Projections due to Carbon Cycle Feedbacks, *Journal of Climate*, 27, 511–526, <https://doi.org/10.1175/JCLI-D-12-00579.1>, publisher: American Meteorological Society Section: *Journal of Climate*, 2014.
- 795 Friend, A. D., Lucht, W., Rademacher, T. T., Keribin, R., Betts, R., Cadule, P., Ciais, P., Clark, D. B., Dankers, R., Falloon, P. D., Ito, A., Kahana, R., Kleidon, A., Lomas, M. R., Nishina, K., Ostberg, S., Pavlick, R., Peylin, P., Schaphoff, S., Vuichard, N., Warszawski, L., Wiltshire, A., and Woodward, F. I.: Carbon residence time dominates uncertainty in terrestrial vegetation responses to future climate and atmospheric CO₂, *Proceedings of the National Academy of Sciences*, 111, 3280–3285, <https://doi.org/10.1073/pnas.1222477110>, publisher: National Academy of Sciences Section: *Biological Sciences*, 2014.



- 800 Gerten, D., Schaphoff, S., Haberlandt, U., Lucht, W., and Sitch, S.: Terrestrial vegetation and water balance—hydrological evaluation of a dynamic global vegetation model, *Journal of Hydrology*, 286, 249–270, <https://doi.org/10.1016/j.jhydrol.2003.09.029>, 2004.
- Green, J. K., Konings, A. G., Alemohammad, S. H., Berry, J., Entekhabi, D., Kolassa, J., Lee, J.-E., and Gentine, P.: Regionally strong feedbacks between the atmosphere and terrestrial biosphere, *Nature Geoscience*, 10, 410–414, <https://doi.org/10.1038/ngeo2957>, number: 6 Publisher: Nature Publishing Group, 2017.
- 805 Green, W. H. and Ampt, G. A.: *Studies on Soil Physics.*, The Journal of Agricultural Science, 4, 1–24, <https://doi.org/10.1017/S0021859600001441>, publisher: Cambridge University Press, 1911.
- Guo, Z., Dirmeyer, P. A., Koster, R. D., Sud, Y. C., Bonan, G., Oleson, K. W., Chan, E., Versegny, D., Cox, P., Gordon, C. T., McGregor, J. L., Kanae, S., Kowalczyk, E., Lawrence, D., Liu, P., Mocko, D., Lu, C.-H., Mitchell, K., Malyshev, S., McAvaney, B., Oki, T., Yamada, T., Pitman, A., Taylor, C. M., Vasic, R., and Xue, Y.: GLACE: The Global Land–Atmosphere Coupling Experiment. Part II: Analysis, *Journal of Hydrometeorology*, 7, 611–625, <https://doi.org/10.1175/JHM511.1>, publisher: American Meteorological Society Section: Journal of Hydrometeorology, 2006.
- 810 Houghton, N., Abramowitz, G., Pitman, A. J., Or, D., Best, M. J., Johnson, H. R., Balsamo, G., Boone, A., Cuntz, M., Decharme, B., Dirmeyer, P. A., Dong, J., Ek, M., Guo, Z., Haverd, V., Hurk, B. J. J. v. d., Nearing, G. S., Pak, B., Santanello, J. A., Stevens, L. E., and Vuichard, N.: The Plumbing of Land Surface Models: Is Poor Performance a Result of Methodology or Data Quality?, *Journal of Hydrometeorology*, 17, 1705–1723, <https://doi.org/10.1175/JHM-D-15-0171.1>, publisher: American Meteorological Society Section: Journal of Hydrometeorology, 2016.
- 815 Haxeltine, A. and Prentice, I. C.: A General Model for the Light-Use Efficiency of Primary Production, *Functional Ecology*, 10, 551–561, <https://doi.org/10.2307/2390165>, 1996.
- Huntingford, C., Lowe, J. A., Booth, B. B. B., Jones, C. D., Harris, G. R., Gohar, L. K., and Meir, P.: Contributions of carbon cycle uncertainty to future climate projection spread, *Tellus B: Chemical and Physical Meteorology*, 61, 355–360, <https://doi.org/10.1111/j.1600-0889.2008.00414.x>, publisher: Taylor & Francis _eprint: <https://www.tandfonline.com/doi/pdf/10.1111/j.1600-0889.2008.00414.x>, 2009.
- 820 Hutley, L. B., Beringer, J., Isaac, P. R., Hacker, J. M., and Cernusak, L. A.: A sub-continental scale living laboratory: Spatial patterns of savanna vegetation over a rainfall gradient in northern Australia, *Agricultural and Forest Meteorology*, 151, 1417–1428, <https://doi.org/10.1016/j.agrformet.2011.03.002>, 2011.
- 825 Johansen, O.: *Thermal Conductivity of Soils*, PhD thesis, Trondheim University, Norway, <https://ci.nii.ac.jp/naid/10003620379/>, 1975.
- Johansen, O.: *Thermal Conductivity of Soils*, Tech. rep., COLD REGIONS RESEARCH AND ENGINEERING LAB HANOVER NH, <https://apps.dtic.mil/sti/citations/ADA044002>, section: Technical Reports, 1977.
- Jones, C., Robertson, E., Arora, V., Friedlingstein, P., Shevliakova, E., Bopp, L., Brovkin, V., Hajima, T., Kato, E., Kawamiya, M., Liddicoat, S., Lindsay, K., Reick, C. H., Roelandt, C., Segsneider, J., and Tjiputra, J.: Twenty-First-Century Compatible CO₂ Emissions and Airborne Fraction Simulated by CMIP5 Earth System Models under Four Representative Concentration Pathways, *Journal of Climate*, 26, 4398–4413, <https://doi.org/10.1175/JCLI-D-12-00554.1>, publisher: American Meteorological Society Section: Journal of Climate, 2013.
- 830 Kosugi, Y., Takanashi, S., Ohkubo, S., Matsuo, N., Tani, M., Mitani, T., Tsutsumi, D., and Nik, A. R.: CO₂ exchange of a tropical rainforest at Pasoh in Peninsular Malaysia, *Agricultural and Forest Meteorology*, 148, 439–452, <https://doi.org/10.1016/j.agrformet.2007.10.007>, 2008.
- 835 Krinner, G., Viovy, N., Noblet-Ducoudré, N. d., Ogée, J., Polcher, J., Friedlingstein, P., Ciais, P., Sitch, S., and Prentice, I. C.: A dynamic global vegetation model for studies of the coupled atmosphere-biosphere system, *Global Biogeochemical Cycles*, 19, <https://doi.org/10.1029/2003GB002199>, _eprint: <https://agupubs.onlinelibrary.wiley.com/doi/pdf/10.1029/2003GB002199>, 2005.



- Kucharik, C. J., Norman, J. M., and Gower, S. T.: Measurements of branch area and adjusting leaf area index indirect measurements, *Agricultural and Forest Meteorology*, 91, 69–88, [https://doi.org/10.1016/S0168-1923\(98\)00064-1](https://doi.org/10.1016/S0168-1923(98)00064-1), 1998.
- 840 Kumar, S., Dirmeyer, P. A., Merwade, V., DelSole, T., Adams, J. M., and Niyogi, D.: Land use/cover change impacts in CMIP5 climate simulations: A new methodology and 21st century challenges, *Journal of Geophysical Research: Atmospheres*, 118, 6337–6353, <https://doi.org/10.1002/jgrd.50463>, eprint: <https://agupubs.onlinelibrary.wiley.com/doi/pdf/10.1002/jgrd.50463>, 2013.
- Kurz, W. A., Dymond, C. C., Stinson, G., Rampley, G. J., Neilson, E. T., Carroll, A. L., Ebata, T., and Safranyik, L.: Mountain pine beetle and forest carbon feedback to climate change, *Nature*, 452, 987–990, <https://doi.org/10.1038/nature06777>, bandiera_abtest: a Cg_type: Nature Research Journals Number: 7190 Primary_atype: Research Publisher: Nature Publishing Group, 2008.
- 845 Lamarque, J.-F., Dentener, F., McConnell, J., Ro, C.-U., Shaw, M., Vet, R., Bergmann, D., Cameron-Smith, P., Dalsoren, S., Doherty, R., Faluvegi, G., Ghan, S. J., Josse, B., Lee, Y. H., MacKenzie, I. A., Plummer, D., Shindell, D. T., Skeie, R. B., Stevenson, D. S., Strode, S., Zeng, G., Curran, M., Dahl-Jensen, D., Das, S., Fritzsche, D., and Nolan, M.: Multi-model mean nitrogen and sulfur deposition from the Atmospheric Chemistry and Climate Model Intercomparison Project (ACCMIP): evaluation of historical and projected future changes, *Atmospheric Chemistry and Physics*, 13, 7997–8018, <https://doi.org/10.5194/acp-13-7997-2013>, publisher: Copernicus GmbH, 2013.
- 850 Lawrence, D. and Vandecar, K.: Effects of tropical deforestation on climate and agriculture, *Nature Climate Change*, 5, 27–36, <https://doi.org/10.1038/nclimate2430>, bandiera_abtest: a Cg_type: Nature Research Journals Number: 1 Primary_atype: Reviews Publisher: Nature Publishing Group Subject_term: Agroecology;Climate and Earth system modelling;Climate-change impacts;Hydrology Subject_term_id: agri-ecology;climate-and-earth-system-modelling;climate-change-impacts;hydrology, 2015.
- 855 Lawrence, P. J. and Chase, T. N.: Representing a new MODIS consistent land surface in the Community Land Model (CLM 3.0), *Journal of Geophysical Research: Biogeosciences*, 112, <https://doi.org/10.1029/2006JG000168>, 2007.
- Le Quéré, C., Andrew, R. M., Friedlingstein, P., Sitch, S., Hauck, J., Pongratz, J., Pickers, P. A., Korsbakken, J. I., Peters, G. P., Canadell, J. G., Arneeth, A., Arora, V. K., Barbero, L., Bastos, A., Bopp, L., Chevallier, F., Chini, L. P., Ciais, P., Doney, S. C., Gkritzalis, T., Goll, D. S., Harris, I., Haverd, V., Hoffman, F. M., Hoppema, M., Houghton, R. A., Hurtt, G., Ilyina, T., Jain, A. K., Johannessen, T., Jones, 860 C. D., Kato, E., Keeling, R. F., Goldewijk, K. K., Landschützer, P., Lefèvre, N., Lienert, S., Liu, Z., Lombardozi, D., Metz, N., Munro, D. R., Nabel, J. E. M. S., Nakaoka, S.-i., Neill, C., Olsen, A., Ono, T., Patra, P., Peregon, A., Peters, W., Peylin, P., Pfeil, B., Pierrot, D., Poulter, B., Rehder, G., Resplandy, L., Robertson, E., Rocher, M., Rödenbeck, C., Schuster, U., Schwinger, J., Séférian, R., Skjelvan, I., Steinhoff, T., Sutton, A., Tans, P. P., Tian, H., Tilbrook, B., Tubiello, F. N., van der Laan-Luijkx, I. T., van der Werf, G. R., Viovy, N., Walker, A. P., Wiltshire, A. J., Wright, R., Zaehle, S., and Zheng, B.: Global Carbon Budget 2018, *Earth System Science Data*, 10, 865 2141–2194, <https://doi.org/10.5194/essd-10-2141-2018>, publisher: Copernicus GmbH, 2018.
- Levis, S., Foley, J. A., and Pollard, D.: Large-Scale Vegetation Feedbacks on a Doubled CO₂ Climate, *Journal of Climate*, 13, 1313–1325, [https://doi.org/10.1175/1520-0442\(2000\)013<1313:LSVFOA>2.0.CO;2](https://doi.org/10.1175/1520-0442(2000)013<1313:LSVFOA>2.0.CO;2), publisher: American Meteorological Society Section: Journal of Climate, 2000.
- Lindeskog, M., Arneeth, A., Bondeau, A., Waha, K., Seaquist, J., Olin, S., and Smith, B.: Implications of accounting for land use in simulations of ecosystem carbon cycling in Africa, *Earth System Dynamics*, 4, 385–407, <https://doi.org/10.5194/esd-4-385-2013>, 2013.
- 870 Lindeskog, M., Smith, B., Lagergren, F., Sycheva, E., Ficko, A., Pretzsch, H., and Rammig, A.: Accounting for forest management in the estimation of forest carbon balance using the dynamic vegetation model LPJ-GUESS (v4.0, r9710): implementation and evaluation of simulations for Europe, *Geoscientific Model Development*, 14, 6071–6112, <https://doi.org/10.5194/gmd-14-6071-2021>, publisher: Copernicus GmbH, 2021.



- 875 Lorenz, R., Davin, E. L., Lawrence, D. M., Stöckli, R., and Seneviratne, S. I.: How Important is Vegetation Phenology for European Climate and Heat Waves?, *Journal of Climate*, 26, 10 077–10 100, <https://doi.org/10.1175/JCLI-D-13-00040.1>, publisher: American Meteorological Society Section: *Journal of Climate*, 2013.
- Luo, Y.: Terrestrial Carbon–Cycle Feedback to Climate Warming, *Annual Review of Ecology, Evolution, and Systematics*, 38, 683–712, <https://doi.org/10.1146/annurev.ecolsys.38.091206.095808>, eprint: <https://doi.org/10.1146/annurev.ecolsys.38.091206.095808>, 2007.
- 880 López-Ballesteros, A., Serrano-Ortiz, P., Kowalski, A. S., Sánchez-Cañete, E. P., Scott, R. L., and Domingo, F.: Subterranean ventilation of allochthonous CO₂ governs net CO₂ exchange in a semiarid Mediterranean grassland, *Agricultural and Forest Meteorology*, 234–235, 115–126, <https://doi.org/10.1016/j.agrformet.2016.12.021>, 2017.
- McGuire, A. D., Sitch, S., Clein, J. S., Dargaville, R., Esser, G., Foley, J., Heimann, M., Joos, F., Kaplan, J., Kicklighter, D. W., Meier, R. A., Melillo, J. M., Moore III, B., Prentice, I. C., Ramankutty, N., Reichenau, T., Schloss, A., Tian, H., Williams, L. J., and Wittenberg, U.: Carbon balance of the terrestrial biosphere in the Twentieth Century: Analyses of CO₂, climate and land use effects with four process-based ecosystem models, *Global Biogeochemical Cycles*, 15, 183–206, <https://doi.org/10.1029/2000GB001298>, eprint: <https://onlinelibrary.wiley.com/doi/pdf/10.1029/2000GB001298>, 2001.
- 885 Medlyn, B. E., Duursma, R. A., Eamus, D., Ellsworth, D. S., Prentice, I. C., Barton, C. V. M., Crous, K. Y., Angelis, P. D., Freeman, M., and Wingate, L.: Reconciling the optimal and empirical approaches to modelling stomatal conductance, *Global Change Biology*, 17, 2134–2144, <https://doi.org/10.1111/j.1365-2486.2010.02375.x>, 2011.
- Medvigy, D., Walko, R. L., Otte, M. J., and Avissar, R.: Simulated Changes in Northwest U.S. Climate in Response to Amazon Deforestation, *Journal of Climate*, 26, 9115–9136, <https://doi.org/10.1175/JCLI-D-12-00775.1>, publisher: American Meteorological Society Section: *Journal of Climate*, 2013.
- 895 Merbold, L., Ardö, J., Arneth, A., Scholes, R. J., Nouvellon, Y., de Grandcourt, A., Archibald, S., Bonnefond, J. M., Boulain, N., Brueggemann, N., Bruemmer, C., Cappelaere, B., Ceschia, E., El-Khidir, H. a. M., El-Tahir, B. A., Falk, U., Lloyd, J., Kergoat, L., Le Dantec, V., Mougín, E., Muchinda, M., Mukelabai, M. M., Ramier, D., Rouspard, O., Timouk, F., Veenendaal, E. M., and Kutsch, W. L.: Precipitation as driver of carbon fluxes in 11 African ecosystems, *Biogeosciences*, 6, 1027–1041, <https://doi.org/10.5194/bg-6-1027-2009>, publisher: Copernicus GmbH, 2009.
- Metsaranta, J. M., Kurz, W. A., Neilson, E. T., and Stinson, G.: Implications of future disturbance regimes on the carbon balance of Canada’s managed forest (2010–2100), *Tellus B: Chemical and Physical Meteorology*, 62, 719–728, <https://doi.org/10.1111/j.1600-0889.2010.00487.x>, publisher: Taylor & Francis eprint: <https://doi.org/10.1111/j.1600-0889.2010.00487.x>, 2010.
- 900 Monsi, M. and Saeki, T.: On the Factor Light in Plant Communities and its Importance for Matter Production, *Japanese Journal of Botany*, 14, 22–52, 1953.
- Monsi, M. and Saeki, T.: On the Factor Light in Plant Communities and its Importance for Matter Production, *Annals of Botany*, 95, 549–567, <https://doi.org/10.1093/aob/mci052>, 2005.
- 905 Narisma, G. T. and Pitman, A. J.: The Impact of 200 Years of Land Cover Change on the Australian Near-Surface Climate, *Journal of Hydrometeorology*, 4, 424–436, [https://doi.org/10.1175/1525-7541\(2003\)4<424:TIOYOL>2.0.CO;2](https://doi.org/10.1175/1525-7541(2003)4<424:TIOYOL>2.0.CO;2), publisher: American Meteorological Society Section: *Journal of Hydrometeorology*, 2003.
- Niu, G.-Y., Yang, Z.-L., Mitchell, K. E., Chen, F., Ek, M. B., Barlage, M., Kumar, A., Manning, K., Niyogi, D., Rosero, E., Tewari, M., and Xia, Y.: The community Noah land surface model with multiparameterization options (Noah-MP): 1. Model description and evaluation with local-scale measurements, *Journal of Geophysical Research*, 116, <https://doi.org/10.1029/2010JD015139>, 2011.



- 915 Noblet-Ducoudré, N. d., Boisier, J.-P., Pitman, A., Bonan, G. B., Brovkin, V., Cruz, F., Delire, C., Gayler, V., Hurk, B. J. J. M. v. d., Lawrence, P. J., Molen, M. K. v. d., Müller, C., Reick, C. H., Strengers, B. J., and Voldoire, A.: Determining Robust Impacts of Land-Use-Induced Land Cover Changes on Surface Climate over North America and Eurasia: Results from the First Set of LUCID Experiments, *Journal of Climate*, 25, 3261–3281, <https://doi.org/10.1175/JCLI-D-11-00338.1>, publisher: American Meteorological Society Section: Journal of Climate, 2012.
- Oleson, K., Dai, Y., Bonan, B., Bosilovich, M., Dickinson, R., Dirmeyer, P., Hoffman, F., Houser, P., Levis, S., Niu, G.-Y., Thornton, P., Vertenstein, M., Yang, Z.-L., and Zeng, X.: Technical Description of the Community Land Model (CLM), <https://doi.org/10.5065/D6N877R0>, 2004.
- 920 Olin, S., Lindeskog, M., Pugh, T. A. M., Schurgers, G., Wärlind, D., Mishurov, M., Zaehle, S., Stocker, B. D., Smith, B., and Arneth, A.: Soil carbon management in large-scale Earth system modelling: implications for crop yields and nitrogen leaching, *Earth System Dynamics*, 6, 745–768, <https://doi.org/10.5194/esd-6-745-2015>, 2015.
- O’ishi, R. and Abe-Ouchi, A.: Influence of dynamic vegetation on climate change arising from increasing CO₂, *Climate Dynamics*, 33, 645–663, <https://doi.org/10.1007/s00382-009-0611-y>, 2009.
- 925 Pastorello, G., Trotta, C., Canfora, E., Chu, H., Christianson, D., Cheah, Y.-W., Poindexter, C., Chen, J., Elbashandy, A., Humphrey, M., Isaac, P., Polidori, D., Reichstein, M., Ribeca, A., van Ingen, C., Vuichard, N., Zhang, L., Amiro, B., Ammann, C., Arain, M. A., Ardö, J., Arkebauer, T., Arndt, S. K., Arriga, N., Aubinet, M., Aurela, M., Baldocchi, D., Barr, A., Beamesderfer, E., Marchesini, L. B., Bergeron, O., Beringer, J., Bernhofer, C., Berveiller, D., Billesbach, D., Black, T. A., Blanken, P. D., Bohrer, G., Boike, J., Bolstad, P. V., Bonal, D., Bonnefond, J.-M., Bowling, D. R., Bracho, R., Brodeur, J., Brümmer, C., Buchmann, N., Burban, B., Burns, S. P., Buysse, P., Cale, P., 930 Cavagna, M., Cellier, P., Chen, S., Chini, I., Christensen, T. R., Cleverly, J., Collalti, A., Consalvo, C., Cook, B. D., Cook, D., Coursolle, C., Cremonese, E., Curtis, P. S., D’Andrea, E., da Rocha, H., Dai, X., Davis, K. J., Cinti, B. D., Grandcourt, A. d., Ligne, A. D., De Oliveira, R. C., Delpierre, N., Desai, A. R., Di Bella, C. M., Tommasi, P. d., Dolman, H., Domingo, F., Dong, G., Dore, S., Duce, P., Dufrêne, E., Dunn, A., Dušek, J., Eamus, D., Eichelmann, U., ElKhidir, H. A. M., Eugster, W., Ewenz, C. M., Ewers, B., Famulari, D., Fares, S., Feigenwinter, I., Feitz, A., Fensholt, R., Filippa, G., Fischer, M., Frank, J., Galvagno, M., Gharun, M., Gianelle, D., Gielen, B., Gioli, B., 935 Gitelson, A., Goded, I., Goeckede, M., Goldstein, A. H., Gough, C. M., Goulden, M. L., Graf, A., Griebel, A., Gruening, C., Grünwald, T., Hammerle, A., Han, S., Han, X., Hansen, B. U., Hanson, C., Hatakka, J., He, Y., Hehn, M., Heinesch, B., Hinko-Najera, N., Hörtnagl, L., Hutley, L., Ibrom, A., Ikawa, H., Jackowicz-Korczynski, M., Janouš, D., Jans, W., Jassal, R., Jiang, S., Kato, T., Khomik, M., Klatt, J., Knohl, A., Knox, S., Kobayashi, H., Koerber, G., Kolle, O., Kosugi, Y., Kotani, A., Kowalski, A., Kruijt, B., Kurbatova, J., Kutsch, W. L., Kwon, H., Launiainen, S., Laurila, T., Law, B., Leuning, R., Li, Y., Liddell, M., Limousin, J.-M., Lion, M., Liska, A. J., Lohila, 940 A., López-Ballesteros, A., López-Blanco, E., Loubet, B., Loustau, D., Lucas-Moffat, A., Lüers, J., Ma, S., Macfarlane, C., Magliulo, V., Maier, R., Mammarella, I., Manca, G., Marcolla, B., Margolis, H. A., Marras, S., Massman, W., Mastepanov, M., Matamala, R., Matthes, J. H., Mazzenga, F., McCaughey, H., McHugh, I., McMillan, A. M. S., Merbold, L., Meyer, W., Meyers, T., Miller, S. D., Minerbi, S., Moderow, U., Monson, R. K., Montagnani, L., Moore, C. E., Moors, E., Moreaux, V., Moureaux, C., Munger, J. W., Nakai, T., Neiryneck, J., Nestic, Z., Nicolini, G., Noormets, A., Northwood, M., Noretto, M., Nouvellon, Y., Novick, K., Oechel, W., Olesen, J. E., Ourcival, 945 J.-M., Papuga, S. A., Parmentier, F.-J., Paul-Limoges, E., Pavelka, M., Peichl, M., Pendall, E., Phillips, R. P., Pilegaard, K., Pirk, N., Posse, G., Powell, T., Prasse, H., Prober, S. M., Rambal, S., Rannik, U., Raz-Yaseef, N., Rebmann, C., Reed, D., Dios, V. R. d., Restrepo-Coupe, N., Reverter, B. R., Roland, M., Sabbatini, S., Sachs, T., Saleska, S. R., Sánchez-Cañete, E. P., Sanchez-Mejia, Z. M., Schmid, H. P., Schmidt, M., Schneider, K., Schrader, F., Schroder, I., Scott, R. L., Sedláč, P., Serrano-Ortíz, P., Shao, C., Shi, P., Shironya, I., Siebicke, L., Šigut, L., Silberstein, R., Sirca, C., Spano, D., Steinbrecher, R., Stevens, R. M., Sturtevant, C., Suyker, A., Tagesson, T., Takanashi,



- 950 S., Tang, Y., Tapper, N., Thom, J., Tomassucci, M., Tuovinen, J.-P., Urbanski, S., Valentini, R., van der Molen, M., van Gorsel, E., van Huissteden, K., Varlagin, A., Verfaillie, J., Vesala, T., Vincke, C., Vitale, D., Vygodskaya, N., Walker, J. P., Walter-Shea, E., Wang, H., Weber, R., Westermann, S., Wille, C., Wofsy, S., Wohlfahrt, G., Wolf, S., Woodgate, W., Li, Y., Zampedri, R., Zhang, J., Zhou, G., Zona, D., Agarwal, D., Biraud, S., Torn, M., and Papale, D.: The FLUXNET2015 dataset and the ONEFlux processing pipeline for eddy covariance data, *Scientific Data*, 7, 225, <https://doi.org/10.1038/s41597-020-0534-3>, bandiera_abtest: a Cc_license_type: cc_publicdomain Cg_type: Nature Research Journals Number: 1 Primary_atype: Research Publisher: Nature Publishing Group Subject_term: Carbon cycle;Climate sciences;Environmental sciences Subject_term_id: carbon-cycle;climate-sciences;environmental-sciences, 2020.
- 955 Peñuelas, J., Rutishauser, T., and Filella, I.: Phenology Feedbacks on Climate Change, *Science*, 324, 887–888, <https://doi.org/10.1126/science.1173004>, publisher: American Association for the Advancement of Science, 2009.
- Philip, J. R.: Evaporation, and moisture and heat fields in the soil, *Journal of Meteorology*, 14, 354–366, [https://doi.org/10.1175/1520-0469\(1957\)014<0354:EAMAHF>2.0.CO;2](https://doi.org/10.1175/1520-0469(1957)014<0354:EAMAHF>2.0.CO;2), publisher: American Meteorological Society, 1957.
- 960 Piao, S., Sitch, S., Ciais, P., Friedlingstein, P., Peylin, P., Wang, X., Ahlström, A., Anav, A., Canadell, J. G., Cong, N., Huntingford, C., Jung, M., Levis, S., Levy, P. E., Li, J., Lin, X., Lomas, M. R., Lu, M., Luo, Y., Ma, Y., Myneni, R. B., Poulter, B., Sun, Z., Wang, T., Viovy, N., Zaehle, S., and Zeng, N.: Evaluation of terrestrial carbon cycle models for their response to climate variability and to CO₂ trends, *Global Change Biology*, 19, 2117–2132, <https://doi.org/https://doi.org/10.1111/gcb.12187>, _eprint: <https://onlinelibrary.wiley.com/doi/pdf/10.1111/gcb.12187>, 2013.
- 965 Pitman, A. J.: The evolution of, and revolution in, land surface schemes designed for climate models, *International Journal of Climatology*, 23, 479–510, <https://doi.org/10.1002/joc.893>, 2003.
- Pongratz, J., Reick, C. H., Raddatz, T., and Claussen, M.: Biogeophysical versus biogeochemical climate response to historical anthropogenic land cover change, *Geophysical Research Letters*, 37, <https://doi.org/10.1029/2010GL043010>, _eprint: <https://agupubs.onlinelibrary.wiley.com/doi/pdf/10.1029/2010GL043010>, 2010.
- 970 Prentice, I. C., Cramer, W., Harrison, S. P., Leemans, R., Monserud, R. A., and Solomon, A. M.: Special Paper: A Global Biome Model Based on Plant Physiology and Dominance, Soil Properties and Climate, *Journal of Biogeography*, 19, 117–134, <https://doi.org/10.2307/2845499>, publisher: Wiley, 1992.
- Press, W. H., ed.: Numerical recipes in Fortran 77: the art of scientific computing, no. the art of scientific computing / William H. Press ... ; Vol. [1,1] in Numerical recipes in FORTRAN, Cambridge Univ. Press, Cambridge, 2. ed., reprinted with corr edn., oCLC: 249641445, 2003.
- Quillet, A., Peng, C., and Garneau, M.: Toward dynamic global vegetation models for simulating vegetation–climate interactions and feedbacks: recent developments, limitations, and future challenges, *Environmental Reviews*, 18, 333–353, <https://doi.org/10.1139/A10-016>, publisher: NRC Research Press, 2010.
- 980 Raupach, M. R.: Simplified expressions for vegetation roughness length and zero-plane displacement as functions of canopy height and area index, *Boundary-Layer Meteorology*, 71, 211–216, <https://doi.org/10.1007/BF00709229>, 1994.
- Raupach, M. R.: Corrigenda, *Boundary-Layer Meteorology*, 76, 303–304, <https://doi.org/10.1007/BF00709356>, 1995.
- Richards, L. A.: Capillary conduction of liquids through porous mediums, *Physics*, 1, 318–333, <https://doi.org/10.1063/1.1745010>, publisher: American Institute of Physics, 1931.
- 985 Sakaguchi, K. and Zeng, X.: Effects of soil wetness, plant litter, and under-canopy atmospheric stability on ground evaporation in the Community Land Model (CLM3.5), *Journal of Geophysical Research: Atmospheres*, 114, <https://doi.org/10.1029/2008JD010834>, 2009.



- Saleska, S. R., Miller, S. D., Matross, D. M., Goulden, M. L., Wofsy, S. C., Rocha, H. R. d., Camargo, P. B. d., Crill, P., Daube, B. C., Freitas, H. C. d., Hutyra, L., Keller, M., Kirchhoff, V., Menton, M., Munger, J. W., Pyle, E. H., Rice, A. H., and Silva, H.: Carbon in Amazon Forests: Unexpected Seasonal Fluxes and Disturbance-Induced Losses, *Science*, 302, 1554–1557, 990 <https://doi.org/10.1126/science.1091165>, publisher: American Association for the Advancement of Science Section: Report, 2003.
- Schenk, H. J. and Jackson, R. B.: Rooting depths, lateral root spreads and below-ground/above-ground allometries of plants in water-limited ecosystems, *Journal of Ecology*, 90, 480–494, <https://doi.org/10.1046/j.1365-2745.2002.00682.x>, [_eprint: https://onlinelibrary.wiley.com/doi/pdf/10.1046/j.1365-2745.2002.00682.x](https://onlinelibrary.wiley.com/doi/pdf/10.1046/j.1365-2745.2002.00682.x), 2002.
- Schroder, I., Kuske, T., and Zegelin, S.: Eddy Covariance Dataset for Arcturus (2011–2013), Geoscience Australia, Tech. rep., Canberra, 995 Tech. rep., <https://doi.org/10.21203/rs.3.rs-14249>, 2014.
- Schurgers, G., Ahlström, A., Arneth, A., Pugh, T. A. M., and Smith, B.: Climate Sensitivity Controls Uncertainty in Future Terrestrial Carbon Sink, *Geophysical Research Letters*, 45, 4329–4336, <https://doi.org/10.1029/2018GL077528>, [_eprint: https://onlinelibrary.wiley.com/doi/pdf/10.1029/2018GL077528](https://onlinelibrary.wiley.com/doi/pdf/10.1029/2018GL077528), 2018.
- Sellers, P., Randall, D., Collatz, G., Berry, J., Field, C., Dazlich, D., Zhang, C., Collelo, G., and Bounoua, L.: A Revised Land Surface Parameterization (SiB2) for Atmospheric GCMs. Part I: Model Formulation, *Journal of Climate*, 9, 676–705, [https://doi.org/10.1175/1520-0442\(1996\)009<0676:ARLSPF>2.0.CO;2](https://doi.org/10.1175/1520-0442(1996)009<0676:ARLSPF>2.0.CO;2), 1996.
- Sellers, P. J.: Canopy reflectance, photosynthesis and transpiration, *International Journal of Remote Sensing*, 6, 1335–1372, <https://doi.org/10.1080/01431168508948283>, 1985.
- Sitch, S., Smith, B., Prentice, I. C., Arneth, A., Bondeau, A., Cramer, W., Kaplan, J. O., Levis, S., Lucht, W., Sykes, M. T., Thonicke, K., 1005 and Venevsky, S.: Evaluation of ecosystem dynamics, plant geography and terrestrial carbon cycling in the LPJ dynamic global vegetation model, *Global Change Biology*, 9, 161–185, <https://doi.org/10.1046/j.1365-2486.2003.00569.x>, 2003.
- Smith, B., Prentice, I. C., and Sykes, M. T.: Representation of vegetation dynamics in the modelling of terrestrial ecosystems: comparing two contrasting approaches within European climate space, *Global Ecology*, p. 25, 2001.
- Smith, B., Samuelsson, P., Wramneby, A., and Rummukainen, M.: A model of the coupled dynamics of climate, vegetation and 1010 terrestrial ecosystem biogeochemistry for regional applications, *Tellus A: Dynamic Meteorology and Oceanography*, 63, 87–106, <https://doi.org/10.1111/j.1600-0870.2010.00477.x>, 2011.
- Smith, B., Wårlind, D., Arneth, A., Hickler, T., Leadley, P., Siltberg, J., and Zaehle, S.: Implications of incorporating N cycling and N limitations on primary production in an individual-based dynamic vegetation model, *Biogeosciences*, 11, 2027–2054, <https://doi.org/https://doi.org/10.5194/bg-11-2027-2014>, 2014.
- 1015 Stefani, P., Belelli Marchesini, L., Consalvo, C., Forgione, A., Bombelli, A., Grieco, E., Mazzenga, F., Vittorini, E., Papale, D., and Valentini, R.: Eddy Flux Tower in Ankasa Park : a new facility for the study of the carbon cycle of primary tropical forests in Africa, 11, 9538, <http://adsabs.harvard.edu/abs/2009EGUGA..11.9538S>, conference Name: EGU General Assembly Conference Abstracts, 2009.
- Stöckli, R., Lawrence, D. M., Niu, G.-Y., Oleson, K. W., Thornton, P. E., Yang, Z.-L., Bonan, G. B., Denning, A. S., and Running, S. W.: Use of FLUXNET in the Community Land Model development, *Journal of Geophysical Research: Biogeosciences*, 113, 1020 <https://doi.org/https://doi.org/10.1029/2007JG000562>, [_eprint: https://agupubs.onlinelibrary.wiley.com/doi/pdf/10.1029/2007JG000562](https://agupubs.onlinelibrary.wiley.com/doi/pdf/10.1029/2007JG000562), 2008.
- Swann, A. L. S., Fung, I. Y., and Chiang, J. C. H.: Mid-latitude afforestation shifts general circulation and tropical precipitation, *Proceedings of the National Academy of Sciences*, 109, 712–716, <https://doi.org/10.1073/pnas.1116706108>, publisher: National Academy of Sciences Section: Physical Sciences, 2012.



- 1025 Taylor, K. E.: Summarizing multiple aspects of model performance in a single diagram, *Journal of Geophysical Research: Atmospheres*, 106, 7183–7192, <https://doi.org/https://doi.org/10.1029/2000JD900719>, _eprint: <https://agupubs.onlinelibrary.wiley.com/doi/pdf/10.1029/2000JD900719>, 2001.
- Thonicke, K., Venevsky, S., Sitch, S., and Cramer, W.: The role of fire disturbance for global vegetation dynamics: coupling fire into a Dynamic Global Vegetation Model, *Global Ecology and Biogeography*, 10, 661–677, <https://doi.org/10.1046/j.1466-822X.2001.00175.x>,
1030 _eprint: <https://onlinelibrary.wiley.com/doi/pdf/10.1046/j.1466-822X.2001.00175.x>, 2001.
- Wang, Y. P. and Leuning, R.: A two-leaf model for canopy conductance, photosynthesis and partitioning of available energy I: Model description and comparison with a multi-layered model, *Agricultural and Forest Meteorology*, 91, 89–111, [https://doi.org/10.1016/S0168-1923\(98\)00061-6](https://doi.org/10.1016/S0168-1923(98)00061-6), 1998.
- Wania, R., Ross, I., and Prentice, I. C.: Integrating peatlands and permafrost into a dynamic global vegetation model: 1. Evaluation and
1035 sensitivity of physical land surface processes: PEATLANDS AND PERMAFROST IN LPJ, 1, *Global Biogeochemical Cycles*, 23, n/a–n/a, <https://doi.org/10.1029/2008GB003412>, 2009.
- Weiss, M., Miller, P. A., Hurk, B. J. J. M. v. d., Noije, T. v., Ștefănescu, S., Haarsma, R., Ulft, L. H. v., Hazeleger, W., Sager, P. L., Smith, B., and Schurgers, G.: Contribution of Dynamic Vegetation Phenology to Decadal Climate Predictability, *Journal of Climate*, 27, 8563–8577, <https://doi.org/10.1175/JCLI-D-13-00684.1>, publisher: American Meteorological Society Section: Journal of Climate, 2014.
- 1040 Werth, D. and Avissar, R.: The local and global effects of Amazon deforestation, *Journal of Geophysical Research: Atmospheres*, 107, LBA 55–1–LBA 55–8, <https://doi.org/10.1029/2001JD000717>, _eprint: <https://agupubs.onlinelibrary.wiley.com/doi/pdf/10.1029/2001JD000717>, 2002.
- Wolf, A., Ciais, P., Bellassen, V., Delbart, N., Field, C. B., and Berry, J. A.: Forest biomass allometry in global land surface models, *Global Biogeochemical Cycles*, 25, <https://doi.org/10.1029/2010GB003917>, _eprint: <https://onlinelibrary.wiley.com/doi/pdf/10.1029/2010GB003917>, 2011a.
- 1045 Wolf, S., Eugster, W., Potvin, C., Turner, B. L., and Buchmann, N.: Carbon sequestration potential of tropical pasture compared with afforestation in Panama, *Global Change Biology*, 17, 2763–2780, <https://doi.org/https://doi.org/10.1111/j.1365-2486.2011.02460.x>, _eprint: <https://onlinelibrary.wiley.com/doi/pdf/10.1111/j.1365-2486.2011.02460.x>, 2011b.
- Wramneby, A., Smith, B., and Samuelsson, P.: Hot spots of vegetation-climate feedbacks under future greenhouse forcing in Europe, *Journal of Geophysical Research: Atmospheres*, 115, <https://doi.org/10.1029/2010JD014307>, _eprint: <https://agupubs.onlinelibrary.wiley.com/doi/pdf/10.1029/2010JD014307>, 2010.
- 1050 Wu, M., Schurgers, G., Rummukainen, M., Smith, B., Samuelsson, P., Jansson, C., Siltberg, J., and May, W.: Vegetation–climate feedbacks modulate rainfall patterns in Africa under future climate change, *Earth System Dynamics*, 7, 627–647, <https://doi.org/10.5194/esd-7-627-2016>, publisher: Copernicus GmbH, 2016.
- 1055 Wu, M., Schurgers, G., Ahlström, A., Rummukainen, M., Miller, P. A., Smith, B., and May, W.: Impacts of land use on climate and ecosystem productivity over the Amazon and the South American continent, *Environmental Research Letters*, 12, 054016, <https://doi.org/10.1088/1748-9326/aa6fd6>, publisher: IOP Publishing, 2017.
- Wu, M., Smith, B., Schurgers, G., Ahlström, A., and Rummukainen, M.: Vegetation–Climate Feedbacks Enhance Spatial Heterogeneity of Pan-Amazonian Ecosystem States Under Climate Change, *Geophysical Research Letters*, 48, e2020GL092001, <https://doi.org/10.1029/2020GL092001>, _eprint: <https://onlinelibrary.wiley.com/doi/pdf/10.1029/2020GL092001>, 2021.
- 1060



- Xue, Y., Sellers, P. J., Kinter, J. L., and Shukla, J.: A Simplified Biosphere Model for Global Climate Studies, *Journal of Climate*, 4, 345–364, [https://doi.org/10.1175/1520-0442\(1991\)004<0345:ASBMFG>2.0.CO;2](https://doi.org/10.1175/1520-0442(1991)004<0345:ASBMFG>2.0.CO;2), publisher: American Meteorological Society Section: Journal of Climate, 1991.
- 1065 Zeng, N., Neelin, J. D., Lau, K.-M., and Tucker, C. J.: Enhancement of Interdecadal Climate Variability in the Sahel by Vegetation Interaction, *Science*, 286, 1537–1540, <https://doi.org/10.1126/science.286.5444.1537>, publisher: American Association for the Advancement of Science Section: Report, 1999.
- Zhang, W., Jansson, C., Miller, P. A., Smith, B., and Samuelsson, P.: Biogeophysical feedbacks enhance the Arctic terrestrial carbon sink in regional Earth system dynamics, *Biogeosciences*, 11, 5503–5519, <https://doi.org/10.5194/bg-11-5503-2014>, publisher: Copernicus GmbH, 2014.
- 1070 Zhang, W., Miller, P. A., Jansson, C., Samuelsson, P., Mao, J., and Smith, B.: Self-Amplifying Feedbacks Accelerate Greening and Warming of the Arctic, *Geophysical Research Letters*, 45, 7102–7111, <https://doi.org/10.1029/2018GL077830>, [_eprint: https://onlinelibrary.wiley.com/doi/pdf/10.1029/2018GL077830](https://onlinelibrary.wiley.com/doi/pdf/10.1029/2018GL077830), 2018.
- 1075 Zscheischler, J., Mahecha, M. D., Buttlar, J. v., Harmeling, S., Jung, M., Rammig, A., Randerson, J. T., Schölkopf, B., Seneviratne, S. I., Tomelleri, E., Zaehle, S., and Reichstein, M.: A few extreme events dominate global interannual variability in gross primary production, *Environmental Research Letters*, 9, 035 001, <https://doi.org/10.1088/1748-9326/9/3/035001>, publisher: IOP Publishing, 2014.